# Geo-modeling and fluid flow simulation in paleokarst reservoirs

Master Thesis

Jon Petter Furnée



Department of Physics and Technology/Department of Earth Science

Uni Research, Centre for Integrated Petroleum Research

June 2015

Contact info:

jpfurnee@gmail.com

+47 470 89 298

# Abstract

This master thesis focuses on modeling and simulation of fluid flow in collapsed paleocave systems, also known as paleokarst. Petroleum reservoirs all around the world exhibit karst structures. The latest ones on the Norwegian Shelf are the discoveries *Gohta* (7120/1-3) and *Alta* (7220/11-1), the wells were drilled by Lundin Norway AS and completed respectively October 2013 and 2014. Reservoirs of this kind have substantial heterogeneity because of the karst features, which has big impact on fluid flow behavior.

This thesis presents a procedure for modeling paleokarst reservoirs in RMS. Furthermore, the effect of the radius of the cave after collapse is tested by comparing production curves derived from simulation of fluid flow in the paleokarst reservoir with Eclipse. Upscaling of the paleokarst reservoir model is also tested to save simulation time, while minimizing the loss of vital information about the reservoir petrophysical properties. Finally, this thesis presents several simulation results that can be used as reference curves for future simulation of either synthetic- or real paleokarst reservoirs.

The study in this thesis may provide a better understanding of worldwide petroleum reservoirs that fall in the same category.

# Acknowledgement

This Master Thesis is part of my Master Degree in Petroleum Technology – Reservoir Geology at the Department of Technology and Physics and the Department of Earth Science at the University of Bergen. The thesis was mainly supervised by Jan Tveranger and Øystein Pettersen at Uni CIPR, but also by the two co-supervisors Gunnar Sælen and Stein Erik Lauritzen at the Department of Earth Science.

First of all I want to thank Jan for all of his assistance, evaluation and guidance through this thesis. All the hours spent in his office discussing different aspects, guidance with RMS, and evaluation of my writing was essential for this thesis. Øystein participated in quite a few discussions as well, where we found out what we wanted to achieve with this research. He also showed excellent guidance with Eclipse.

Gunnar helped with creating the foundation of the thesis and provided good guidance with the carbonate introduction section. Stein Erik contributed a cornerstone of this thesis, the point-data-set of Setergrotta cave system, which is the basis of the three dimensional paleokarst reservoir model presented in this thesis.

Further, I want to thank Uni CIPR for stimulating my interest in carbonates by sending me on an inspiring trip to the Winter Education Conference hosted by AAPG in Houston (USA) February 2014.

I also want to thank Det norske and my colleagues there for my summer internships and part-time job while studying; it provided me with good insight into the workings of the oil industry. I would particularly like to thank Camilla Oftebro for practical guidance in the use of the RMS software.

Last but not least, I want to thank my partner Kjersti and our daughter Ragnhild for great support and motivation for finishing this Master Thesis.

Jon Petter Furnée

Bergen, May 2015

# Contents

# 1 Introduction

Carbonate reservoirs matter. More than 60% of the world's oil and 40% of the world's gas reserves are held in carbonate reservoirs (Schlumberger, 2008). The carbonate reservoirs of the Middle East region contain about 70% of all known oil and 90% of all known gas reserves (Schlumberger, 2007, Schlumberger, 2008, Schlumberger, 2014a). Fifty-eight percent of all giant-sized (>500 million barrels oil equivalents) oil-field reserves and 25% of all giant-sized gas reserves are located in carbonate reservoirs (Halbouty et al., 1970). These numbers underline that understanding the processes that form and alter carbonate rocks, as well as their petrophysical properties is important to ensure high recovery rates from these reservoirs.

Carbonate reservoirs which have been influence by karstification and associated process, such as secondary clastic sediment infills and collapse features, are found worldwide; a famous example is the Ghawar field in Saudi Arabia, the largest oil field in the World (Afifi, 2005). Other examples are the Casablanca field (Offshore Spain) (Lomando, 1993), Yates field (Texas) (Craig, 1988), the Jingbian gas field and Tahe oilfield (China) (Bing et al., 2011, Kang et al., 2013, Li et al., 2008), and the Garland Field in Wyoming (USA) (Demiralin, 1993).

New prospects and recent discoveries made in in karstified carbonate rocks the Barents Sea (Norway) by Lundin Norway AS highlight that paleokarst plays also can be encountered on the Norwegian continental shelf. The discoveries include the Gohta prospect (Well 7120/1-3) which was completed in October 2013, and the Alta prospect (Well 7220/11-1) which was completed in October 2014.

Karstified carbonate reservoirs are complex and very heterogeneous and therefore is not well understood. The heterogeneity of paleokarst reservoirs originating from a pre-existing system of cave passages is, among other factors, closely linked to the original location of cavities, connectivity between the conduits and to the complex carbonate petrophysical properties. (Lucia, 2007, Pardo-Iguzquiza et al., 2011). The challenge of providing reliable forecasts of reservoir configuration and behavior, thus facilitating optimized production, lies in providing realistic geological models which capture these heterogeneities. This requires an understanding of the processes that form them and methods for rendering them in a realistic manner using reservoir modeling software.

## 1.1 Aim and scope

### 1.1.1 Aim and scope

The challenges faced when producing from carbonate reservoirs in general are well summarized in Burchette (2012), these include predicting reservoir quality, recognizing problematic high permeability features, and making reservoir models with representative physical parameters. Further concerns are linked to the non-linear relationships between porosity and permeability in carbonates and the fact that permeability can range over three to four orders of magnitude for a given porosity. These factors are controlled by the distinctive stratigraphic architectures of carbonate rocks. Burchette (2012) also presents an "*…output from an Industry Technology Facilitation brainstorming meeting in London in 2009…*" listing principle areas of concern with respect to carbonate reservoirs:

- Upscaling of carbonate reservoir models
- Better understanding of processes leading to permeability reduction or improvement, and to determine the best values to assign to flow units in reservoir simulators.
- The effect diagenetic processes has on permeability distribution within carbonate stratigraphic architectures
- How carbonate reservoir geometry in three dimensions relates to stratigraphy
- Understanding dynamic fracture behavior in carbonates over time
- Recovery factors and production characteristics from fractured reservoirs

Additional challenges can be added to this list when also considering the impact of karstification and subsequent collapse, infill and burial. Direct observations from subsurface reservoir are often lacking in detail (seismics) or, if detailed, have limited lateral coverage (wells). The resolution of seismic images is commonly too low to capture paleokarst features, and cave collapse systems are commonly only distinguished indirectly as depressions (discontinuity and sagging of seismic reflectors) with associated faulting (Dou et al., 2011). A detailed understanding of architecture and properties of paleokarst reservoirs must therefore largely be based on a combination of outcrop data and an understanding of how paleokarst features form. Wells drilled through paleokarst reservoirs provides some calibration points. This information can be compiled in high-resolution conceptual or generic models forming the base for understanding and forecasting production behavior.

The topic for this master thesis is; *How will fluid flow be affected by heterogeneity in hydrocarbon reservoirs of karstified carbonate?* It focuses on two specific challenges; 1) geo-modeling of a collapsed karst cave system, and 2) interplay between model parameters and dynamic behavior of such reservoirs.

Geo-modeling of paleokarst reservoirs is anything but straightforward. This is partly due to technical limitations of the software. To my knowledge, no previous attempts have been made to employ standard industrial modeling tools, such as RMS (geo-modeling tool) and Eclipse (simulation software) to carry out modeling and simulation of fluid flow in a real case geometry of a paleokarst system. Although paleokarst-related features such as cave geometries are routinely modelled using specialized speleological software, there is no existing workflow or procedure that allows this to be done using standard reservoir geo-modeling tools employed in the petroleum industry. Part of this thesis therefore focuses on establishing methods and workflows for rendering geometries associated with paleokarst in a realistic manner using RMS.

A second obstacle is posed by defining suitable input data for the models. The geometry and structure of paleokarst reservoirs can be derived from four sources; well data, outcrops, modern cave-/karst systems, and seismic data. As shown by the red arrows on the mind map in Figure 1.1.1-1, this thesis focuses on the use of outcrop data and modern analogues; seismic interpretation and the use of well data from paleokarst reservoirs is outside the scope of this study.

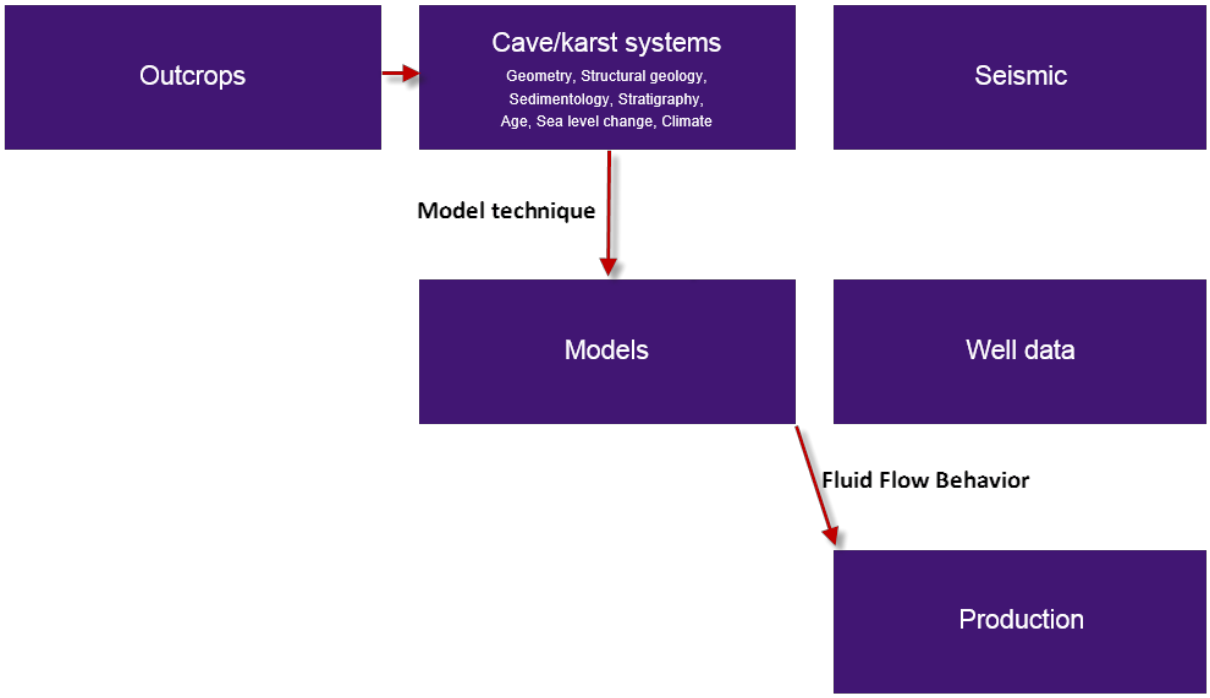


*Figure 1.1.1-1 Mind map thesis. Red arrow shows the structure of this thesis.*

Figure 1.1.1-2 summarizes the workflow used in this thesis. Modeling and simulation of fluid flow in a conceived paleokarst reservoir, constructed using geometries taken from an actual cave system and understanding of collapse process and products has never been tried before with industry-standard programs such as RMS and Eclipse. Particular emphasis is therefore placed on describing the workflow and methods used for constructing and handling the models using these applications. Latching on the challenges related to carbonate reservoirs listed by Burchette (2012), this thesis will address upscaling, assigning the best possible flow units and petrophysical properties in reservoir simulators, the effect of diageneses/collapse of cave passages and their three-dimensional geometry, fractures, and production characteristics as well as recovery factors from paleokarst reservoirs.

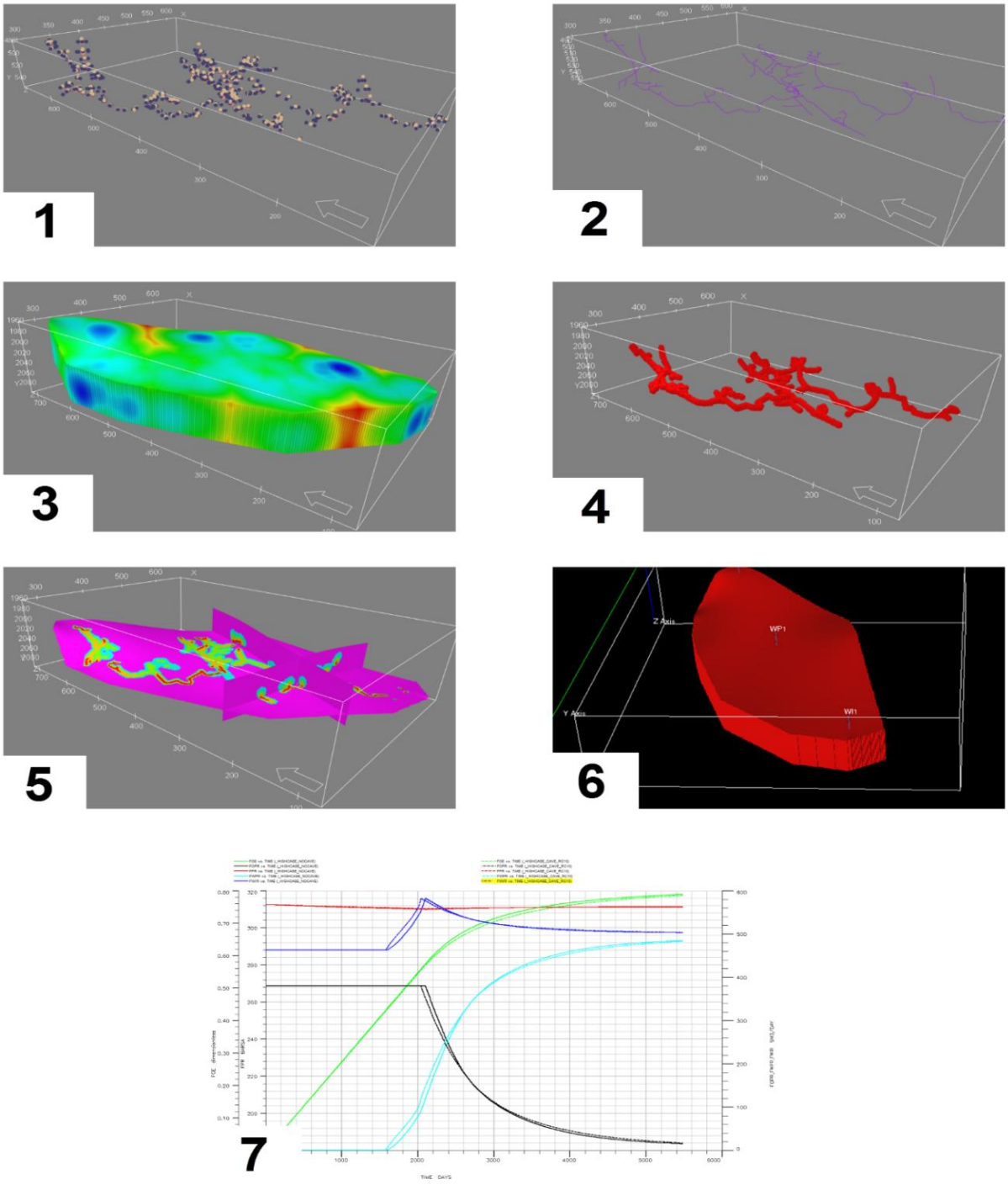


*Figure 1.1.1-2 1) XYZ-coordinates of center-, ceiling-, floor- and wall points in the measured parts of Setergrotta (Mo i Rana, Norway). 2) Skeleton lines drawn between center points, used as input in geometric modeling. 3) Geometric modeling. Uses distance from Skeleton line. 4) Cave with radius 5 meters, derived from geometric modeling. 5) Reservoir model with petrophysical parameters in place (here porosity distribution). 6) Fluid simulation model in Eclipse with wells. 7) Production curves (output from Eclipse simulation).*

## 1.2 Carbonates

### 1.2.1 Formation and composition

Understanding paleokarst reservoirs requires an understanding of carbonate rocks and karst. The following chapters give a brief introduction to the topic as background for the study. While siliciclastic sediments are derived from physical and chemical processes, such as erosion and weathering, carbonate sediments originate from biological and chemical processes in specific areas called “Carbonate factories”. Carbonate sediments are the product of both organic and inorganic processes, with the former being dominant, and are most common in shallow and warm oceans. The production process is characterized either as direct precipitation out of sea water, or by biological extraction of calcium carbonate from seawater to form skeletal material (Coe, 2003). Carbonate sediments consist of carbonate grains, clasts, particles, ooids, peloids, fossil fragments and more. These are loose grains that can be transported by the same physical processes as siliciclastic grains. After deposition however, carbonate sediments are subjected to a variety of diagenetic processes that change porosity, mineralogy and chemistry. These processes transform the carbonate sediment into carbonate rock. (Boggs, 2012)

Carbonates can be divided into limestone and dolomite on the basis of their mineralogy. The elementary chemistry of carbonate rocks is dominated by magnesium $Mg^{2+}$, calcium $Ca^{2+}$ and carbonate $CO_3^2$. Limestone is a sedimentary rock containing 50 percent or more calcium carbonate (calcite or aragonite; both forms of $CaCO_3$), whereas dolomite (or dolostone) contains 50 percent or more of calcium-magnesium carbonate (the mineral dolomite $CaMg(CO_3)_2$) (Boggs, 2012).

### 1.2.2 Limestone

Limestone contains various textures, structures and fossils that yield important information about ancient marine environments and evolution of lifeforms through time. (Boggs, 2012). It comprises mainly three minerals with the same basic chemical formula ($CaCO_3$) but exhibiting different magnesium content and different crystal systems. We distinguish between high-Mg calcite (containing more than 4% MgCO3), low-Mg calcite (containing less than 4% $MgCO_3$) and aragonite. Limestone precipitated in modern oceans is generally aragonite and to a lesser extent high-Mg calcite, but carbonates of early Paleozoic and middle Cenozoic age mainly consist of low-Mg calcite; most likely due to lower Mg/Ca ratios in seawater at that time. (Boggs, 2012)

Calcite has a rhombohedral crystal system while aragonite has an orthorombic crystal system. This has an effect on solubility: aragonite has a less stable crystal structure than calcite and alters readily to low-Mg calcite. (Boggs, 2012)

According to Lucia (2007), carbonate sediments have a wide range of sizes, shapes and mineralogies. They form a multitude of textures, chemical compositions and, most importantly, associated pore-size distributions. Carbonates typically consist of a mixture of carbonate and siliciclastics which petrographically form a compositional spectrum ranging from pure carbonate to nearly pure siliciclastic with only a minor carbonate component. Most carbonate rocks will have a composition in between these extremes. Influx of siliciclastic material can effectively dilute carbonate sedimentation, even in areas of high production. Absence of siliciclastic deposition can, on the other hand promote preservation of carbonate sediments even if sedimentation rates are very low. (Lucia, 2007)

Carbonate grains are typically not transported far from where they were produced, thus the composition and nature of the grains reflect the local depositional environmental setting at the time they were deposited. On the other hand, carbonate rocks are inherently unstable and under the right conditions susceptible to rapid dissolution and diagenesis. Therefore, the original composition of carbonate rocks is rarely conserved, and carbonates typically exhibit extensive diagenetic alteration. (Saller, 2014).

When carbon dioxide comes in contact with rainwater, the following reaction takes place; $H_2O + CO_2 \leftrightarrow H_2CO_3$. Carbonic acid, $H_2CO_3$, can easily dissolve limestone by the following reaction; $CaCO_3 + H_2CO_3 \leftrightarrow Ca^{2+} + 2HCO_3^-$. The carbonate/siliciclastic ratio of a carbonate rock

considerably influences later dissolution processes; pure carbonate can in theory be entirely dissolved, whereas siliciclastics largely remain unaffected. This will influence the mechanical strength and porosity of the rock as it is exposed to corrosive fluids over time. The dissolution process of carbonates can create large cavities in the rock, which is discussed later.

### 1.2.3 Dolomite

Dolomite (or dolostone) contains 50 percent or more of calcium-magnesium carbonate (the mineral dolomite $CaMg(CO_3)_2$). Dolomite commonly forms when calcium carbonate is subjected to magnesium-rich pore fluids. The process of dolomitization follows the equation $2CaCO_3 + Mg^{2+} \leftrightarrow CaMg(CO_3)_2 + Ca^{2+}$ . Seawater is generally the richest source of Mg, and Scholle and Scholle (2014) and Boggs (2011) consider this is the only realistic source for dolomitization.

Dolomite replace carbonate where the latter already has substantially, often localized, permeability enabling transport of water for the dolomitization process. It follows that that dolomites may have high porosity. The chemical conversion of limestone to dolostone involves a reduction in volume because the molar volume of dolomite is smaller than that of calcite. This volume reduction, results in a porosity increase of 12 % (Al-Awadi et al., 2009). Dolomites are less soluble than calcite in most settings and can maintain the rock framework while calcite dissolves to form secondary porosity. Dolomitized rocks are structurally less prone to compaction and depth-related porosity loss (Schmoker and Halley, 1982). This because their hexagonal mineral structure that can take greater compressive strength. Figure 1.2.3-1 shows the relation between burial depth and porosity for limestone versus dolomites. The figure clearly illustrates that even though carbonates commonly exhibit higher porosity at shallow depths, they experience faster loss of porosity than dolomite during burial.

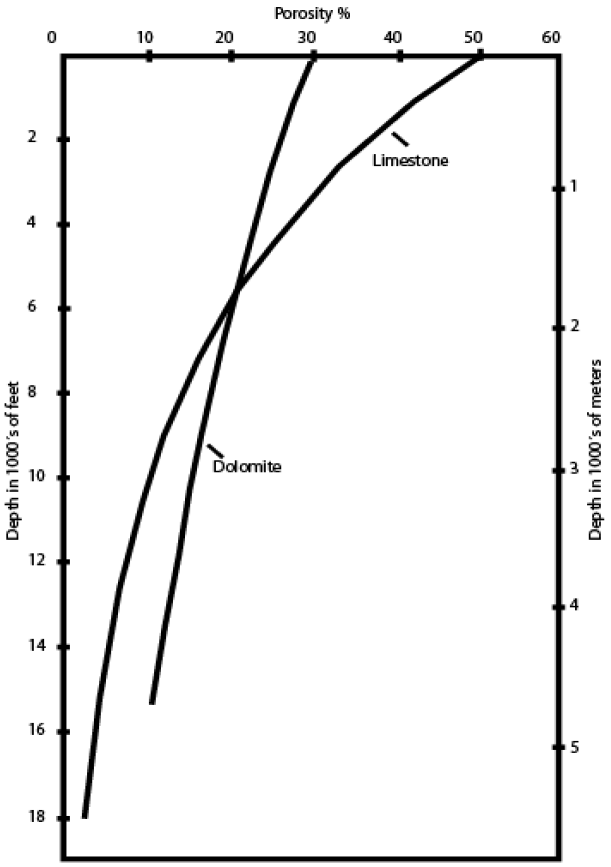


*Figure 1.2.3-1 Porosity/depth plot for carbonates and dolomites based on (Schmoker and Halley, 1982)*

### 1.2.4 Textures in carbonates

Carbonates textures can be described compositionally using a ternary diagram with three end-member components; allochems (grains), carbonate mud matrix (micrite) and sparry calcite cement (Folk, 1962). In Figure 1.2.4-1, the highlighted area shows typical carbonates.

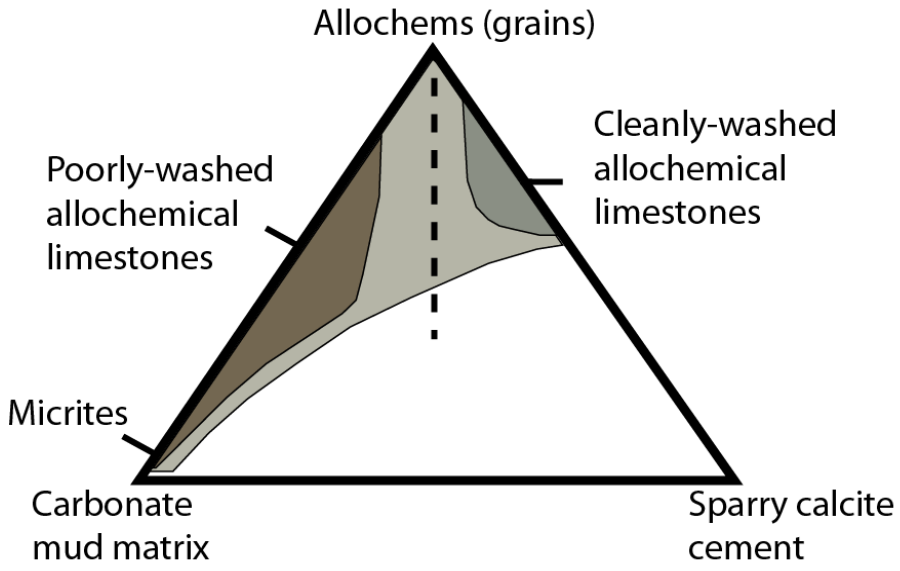


*Figure 1.2.4-1 Three components in carbonate rocks modified from (Folk, 1962) and (Scholle and Scholle, 2014)*

There are four main carbonate grain types (allochems) in sedimentary carbonate rocks; bioclasts, coated grains, pellets and peloids, and intraclasts (see Figure 1.2.4-2). Bioclasts are skeletal fragments, of biogenic origin. Like bioclasts, pellets and peloids are also biogenic. Coated grains include ooids, pisoids, and oncoids, all of which have a chemical and/or biological origin. In contrast to these, intraclasts, consisting of broken skeletal fragments are of erosional origin (Scholle and Scholle, 2014, Scholle and Ulmer-Scholle, 2003).

Texturally, sedimentary carbonate can be divided into forms bound together by organic processes and loose grains (aggregates). Both reefs and stromatolites are examples of the former. Retaining morphologies created during organic growth, can exhibit large constructional cavities and highly porous and permeable textures. Carbonate sediments composed of loose grains are, however, more common. The grain size of loose carbonate sediment is typically bimodal, with a mud fraction and

a fraction of mainly sand-sized grains or bigger. Most mud-sized sediments consist of aragonite crystals produced by authigenic precipitation from sea water, or calcareous planktonic algae such as coccolithophores and foraminifera. The sand-sized sediments typically relate to the size of the calcareous skeletons or exoskeletons/shells of various organisms. Grain size in shell sand can be linked to the degree to which the original assemblage of shells has been broken up and abraded by wave action and currents. (Lucia, 2007).

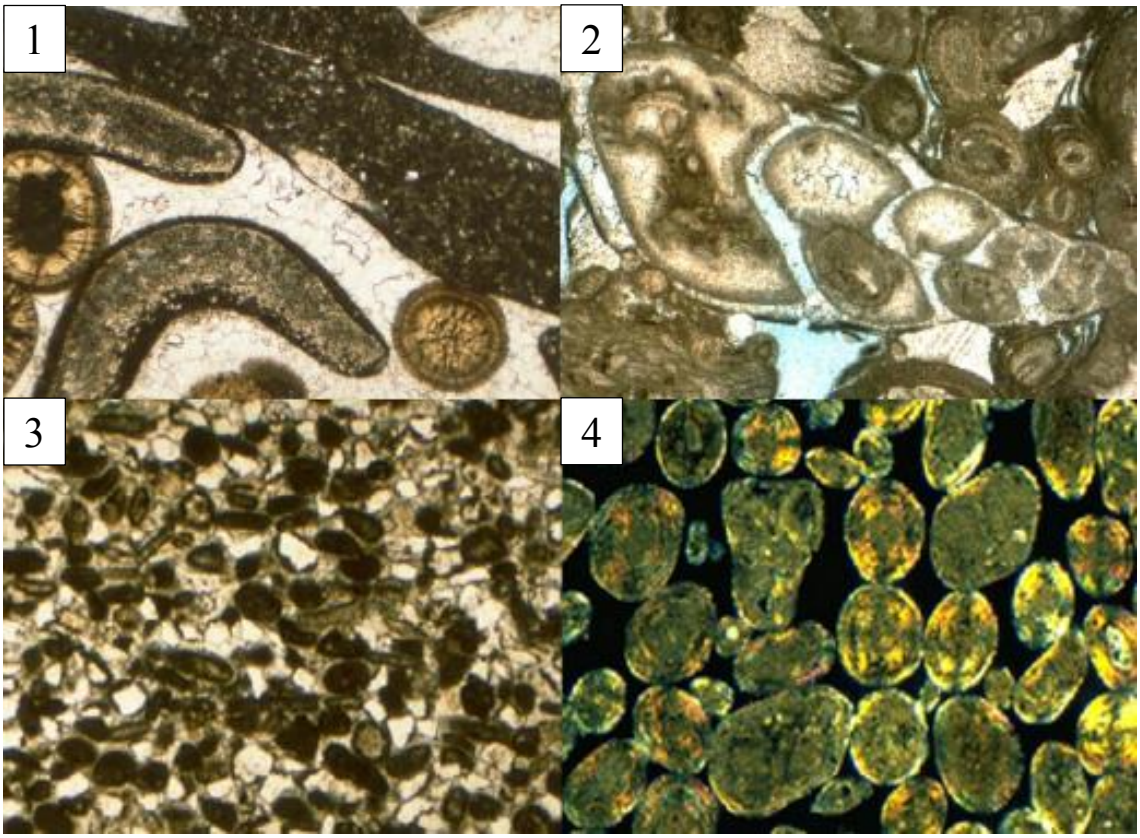


*Figure 1.2.4-2 Figure showing allochems. 1) Intraclasts, 2) bioclasts, 3) pelletal limestone, and 3) coated grains (ooids). Modified from (Scholle and Scholle, 2014, Scholle and Ulmer-Scholle, 2003)*

### 1.2.5 Classification of limestones

Carbonates are classified using Folk´s and Dunham´s classification methods Figure 1.2.5-1 (Figure 1.2.4-1). Folk´s classification from 1962 is based on the relative abundance of three major types of constituents: sparry calcite cement (sparite), microcrystalline carbonate mud (micrite), and carbonate grains or allochems (Figure 1.2.4-1 ). For example, if >25% of the grains are intraclasts, the rock is classified as an intraclastic limestone, and if <25% are intraclasts and >25% are ooids, the rock is labelled ooilitic limestone. Terms can be combined if desired. Dunham (1962) on the other hand, classifies carbonate rocks according to their depositional textures. Scholle and Scholle (2014) point out that the most difficult aspect of the Dunham classification, is deciding whether a rock that has undergone a substantial alteration due to compaction and other diagenetic factors, was originally mud- or grain-supported. Both Folk and Dunham exclude mineralogy from the classification, because it only plays a minor role in classification of carbonate rocks as most carbonates are monomineralic. The mineralogy is primarily used to differentiate between carbonates and non-carbonate rocks, and between limestones and dolomites. (Scholle and Scholle, 2014).

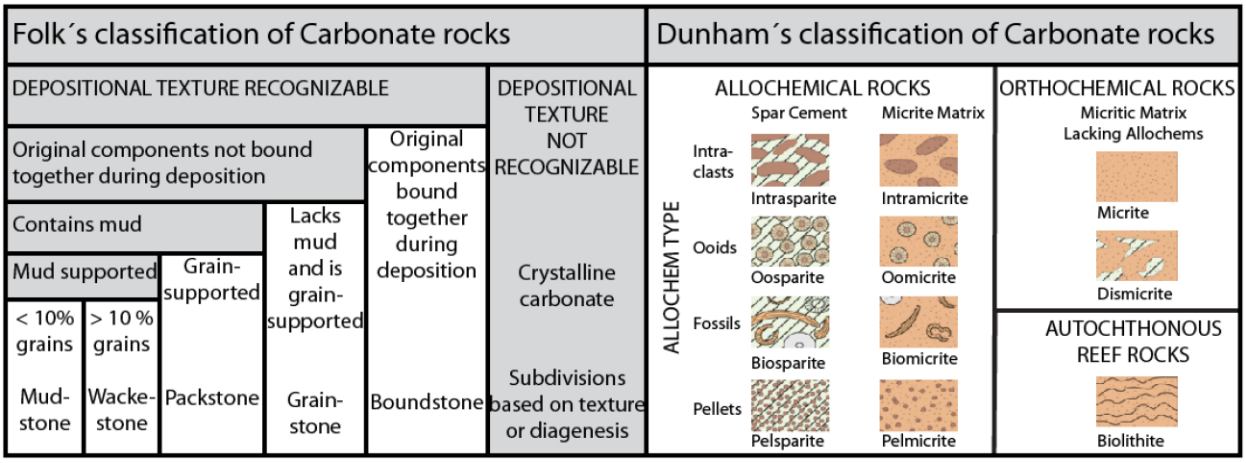


*Figure 1.2.5-1 (left) Folk´s classification of Carbonate rocks modified from (Scholle and Scholle, 2014) and (Folk, 1962), (right) Dunham´s classification of Carbonate rocks modified from (Scholle and Scholle, 2014) and (Dunham, 1962)*

### 1.2.6 Depositional architectures for carbonates

Coe (2003) defines three types of "carbonate factories", settings where carbonates are produced; warm-water, cool-water, and pelagic carbonate factory.

The warm-water carbonate factory is associated with shallow-marine, tropical waters that support rapidly calcifying communities of photosynthesizing organisms. Today, these organisms build shallow-water coral reefs. Furthermore, tropical waters are mostly supersaturated with respect to calcium carbonate, which can be precipitated at the sea floor (e.g. ooid grains).

The cool-water carbonate factory is related to shallow- to moderate-depth shelf environments in temperate and arctic areas. Some tropical areas supporting calcifying communities below the photic zone, can also qualify as cool-water carbonate factories. Cool water carbonate-forming organisms typically include mollusks, bryozoan, and benthic foraminifera. In contrast to warm-water carbonates, cool-water carbonates may have lower rates of carbonate production.

The pelagic carbonate factory encompasses regions where oceanic conditions are suitable for planktonic organisms such as foraminifers and coccolithophores to thrive. Calcifying plankton inhabits the shallow photic zone. Upon death their skeletal remains will settle like pelagic snow on the sea bottom, forming deep-water carbonates. However, the deep and cold oceans are often under-saturated with respect to calcium carbonate below a certain depth, termed the CCD, or carbonate compensation depth (Boggs, 2012). In the Pacific and Indian Ocean, the CCD is found at depths between 3,500 and 4,500 m. In the North Atlantic and the eastern South Atlantic, the CCD occurs deeper than 5,000 m (Bickert, 2009). Below this depth carbonates are dissolved by sea-water.

Warm-water carbonate platforms exhibit the most rapid accumulation rates (Coe, 2003, Sarg, 2014). Over the past million years, only the fastest sea level rise at the end of glacial periods and fault-related subsidence has had the ability to outpace shallow warm-water carbonate accumulation rates.

Distinct differences can be observed when comparing sequence stratigraphy in carbonates and siliciclastic systems; in particular with respect to sedimentation rates. Whereas the highest local sediment flux rates in siliciclastic systems can be observed during episodes of sea level fall, due to fluvial incision, the carbonate production is shut off as carbonate systems become subaerially

exposed. Carbonate systems have their highest ratios of sediment production during sea level rise as a result of increasing accommodation space as flooding creates large areas of shallow, easily warmed, epicontinental sea. Figure 1.2.6-1 below shows the four different carbonate systems tracts; transgressive, regressive, highstand and lowstand systems tract. The categorization is based on the relative sea level and the moving shore line. (Coe, 2003, Saller, 2014, Sarg, 2014, Scholle and Scholle, 2014)

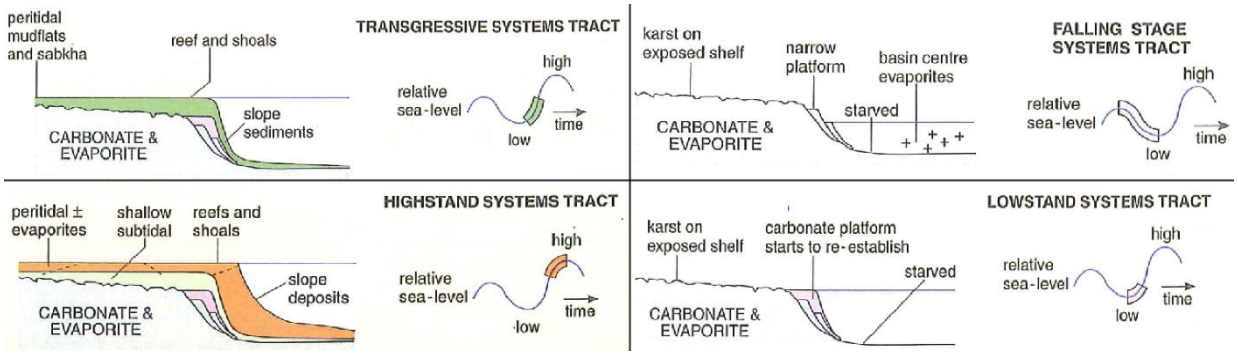


*Figure 1.2.6-1 Sequence stratigraphy for carbonate settings. Modified after (Coe, 2003)*

When the shoreline retrogrades and the sea level is rising, the systems tract is categorized as transgressive. The transgressive systems tract leads to flooding of the shelf and carbonate deposition may keep up with the rising sea level. The carbonate factories now achieve their maximum production. Slope sediments accumulate, either as reef debris, or sediment from the shelf, after storm events. Evaporites may also form in the sabkha environments. The highstand system represents the climax of the transgression as ratio of sea level rise slows down to zero before falling again. Highstand systems tract accommodation space is gradually filled with shallow-water carbonates. If the productivity on the shelf is high, sand shoals or reefs prograding over former resedimented slope deposits may form. (Coe, 2003)

When the sea level falls, regressive systems tracts are formed. For carbonates this may involve subaerial exposure and a shut-down of production. Solution processes erode exposed limestones deposited during the preceding highstand and produce karst topography. Evaporites may form in basins cut off from the ocean and gradually drying out. As the rate of sea level fall slows down to zero and sea level reaches its lowest point, shelf areas remain exposed to karstification processes

driven by meteoric conditions. Low-stand sea-level stabilization is accompanied by re-establishment of carbonate systems and their gradual build-up to sea level. (Coe, 2003)

The ability of carbonate depositional systems to keep up with the creation of accommodation space can lead to very thick successions. The term *carbonate platform* is used to describe ancient thick accumulations of shallow-water carbonates. Carbonate platforms form a range of morphologies, and Figure 1.2.6-2 illustrates these.

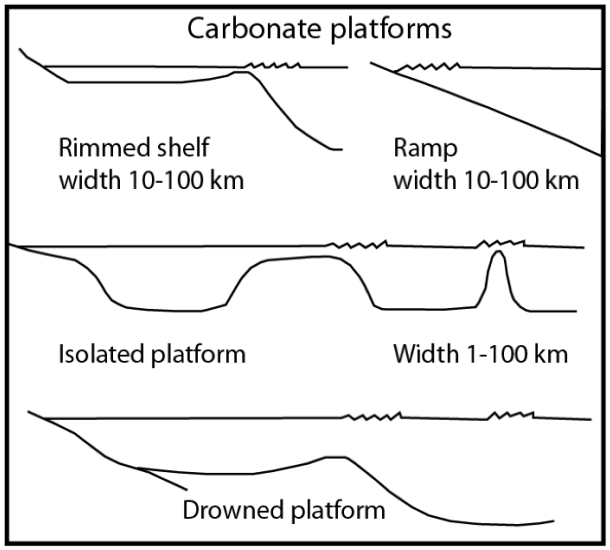


*Figure 1.2.6-2 Carbonate platform morphology modified from (Gischler, 2011) and (Tucker et al., 1990)*

A *rimmed carbonate platform* has a shelf-margin rim or barrier such as a sand shoal or reef that partly isolates an inner platform or lagoon. The rim absorbs wave energy and restricts circulation in the inner platform or lagoon. Rimmed platforms develop at windward margins, because these are most affected by wave energy.

Unrimmed platforms or *ramps* are gently inclined platforms towards the ocean. These often occur at the leeward margins that are less affected by storms and wave energy. They do not develop rims because of their lack of break in the slope, which can be colonized by shallow-water reef-building organisms.

An *isolated platform* is a carbonate platform isolated from the continent. The Bahamas are a great example of an isolated carbonate platform. In Figure 1.2.6-2, the smaller isolated platform is called an *atoll*. An atoll is usually formed over a subsiding volcano.

A *drowned platform* situation occurs when the carbonate deposition cannot keep up with the rate of subsidence. This happens when subsidence rates increase or carbonate production is suppressed by inhospitable conditions such as changes in temperature, nutrient supply or an increase in siliciclastic input. (Coe, 2003, Tucker et al., 1990)

Chalk differs from reefs and carbonate platforms. In modern oceans, chalk is formed by seasonal blooms of shell-forming plankton such as *coccolithophoridae* (see Figure 1.2.6-3 below). For these small skeletons to settle at the sea floor, ocean currents must be relatively weak. Chalks are coccolith-rich limestones, and are very fine-grained. Because of the small grain size, chalks have an inherently low permeability. During burial, the average porosity in chalks decreases even faster than other carbonates in Figure 1.2.3-1, but some chalks retain exceptional porosity because they become filled with oil at an early stage. In contrast to other carbonates, chalks have high chemical stability because they primarily are composed of low-Mg calcite (Scholle, 1977).

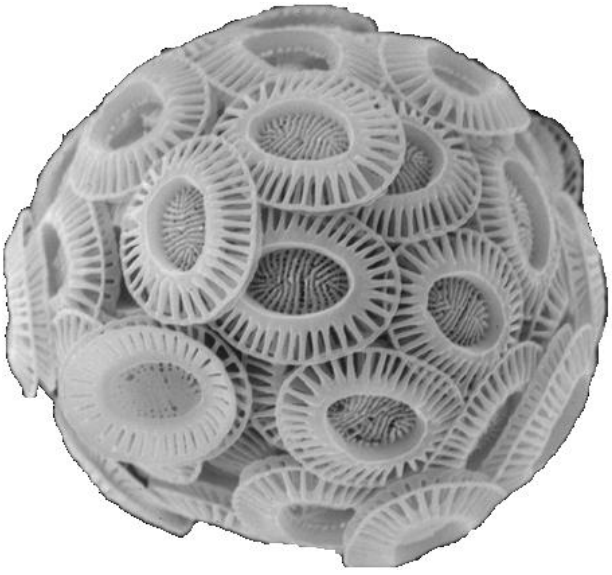

*Figure 1.2.6-3 Coccolithophorid modified from (Scholle and Scholle, 2014). It is approximately 8µm across.*

### 1.2.7 Carbonates through geological time

Carbonate-forming organisms have evolved and changed through geologic time, both due to evolution of organism, but also global environmental changes. Carbonate sediments are products of organic (dominantly) and inorganic processes (Saller, 2014). In these processes, four types of carbonate minerals are formed; low mg-calcite, high mg-calcite, aragonite, and dolomite. In addition to the carbonate forming organisms, the mineralogical composition of carbonates has changed through geological time (see Figure 1.2.7-1 by Scholle and Scholle (2014)). Since composition affects grain stability, the age of the rocks needs to be considered when assessing the effect of dissolution. Modern carbonates are composed of aragonite, calcite or high-Mg calcite, whereas ancient carbonate rocks normally consist of calcite and/or dolomite.

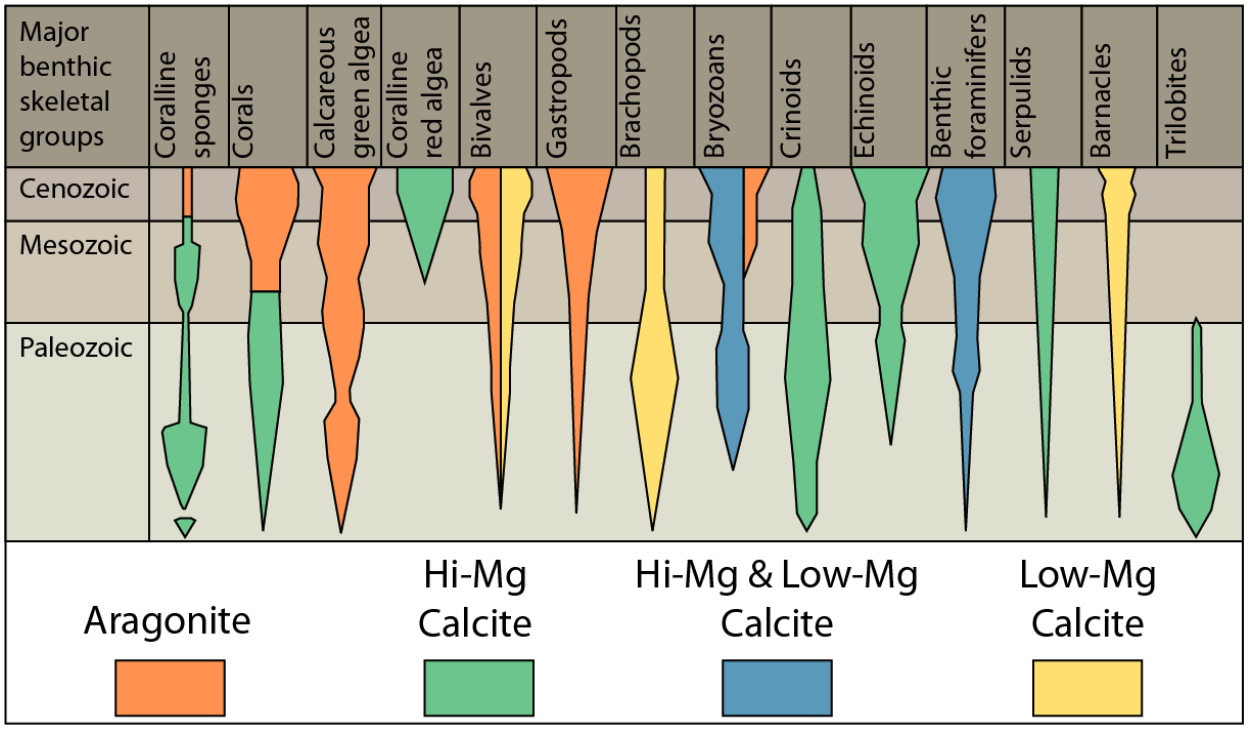


*Figure 1.2.7-1– Skeletal Mineralogy in carbonates over time. Modified from (Scholle and Scholle, 2014)*

The changes in mineralogical composition are commonly attributed to long-term global climate states known as “icehouse” and “greenhouse” (Sandberg, 1983) lasting for millions of years. Fluctuations between these two states are driven by a combination of $CO_2$ concentration in the atmosphere, orbital changes and changes in global land-sea configurations due to plate tectonics

rather than rather than changes in oceanic Mg/Ca-ratio (Sandberg, 1983, Scholle and Scholle, 2014). During icehouse conditions, global cooling is accompanied by eustatic sea level drops as water is bound up in continental ice sheets. This causes carbonate production to stop, and the exposed platforms undergo extensive meteoric diagenesis and karstification. During greenhouse conditions global temperatures rise. Continental ice-sheets melt and cause eustatic sea-level rise, which in turn causes platform drowning and formation of shallow epicontinental seas acting as loci for large carbonate factories. Because of the warm climate, evaporites are also common during greenhouse conditions.

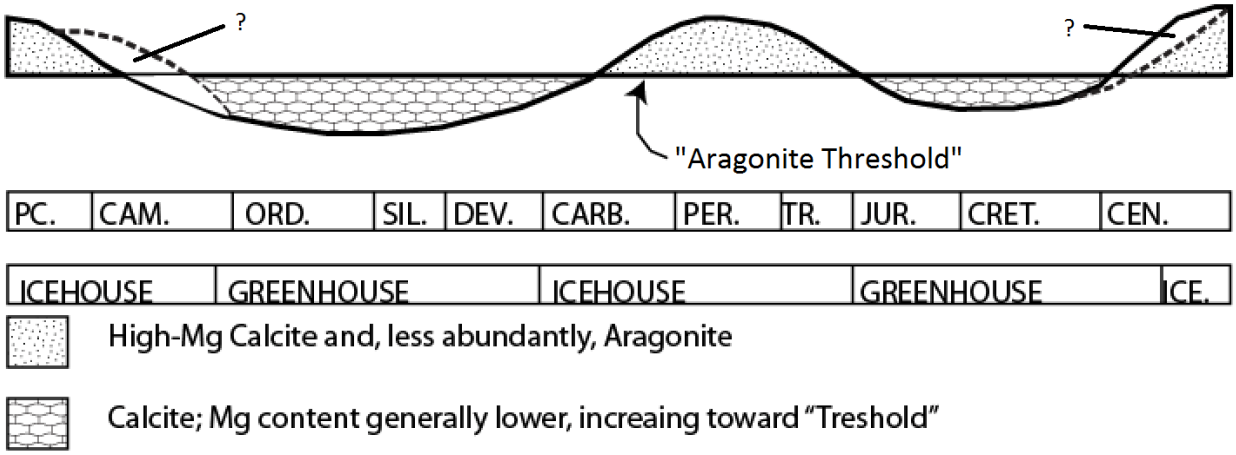


*Figure 1.2.7-2 Icehouse and greenhouse effects on carbonate mineralogy. Modified after (Sandberg, 1983). PC.: Pre-Cambrian, CAM.: Cambrian, ORD.: Ordovician etc.*

Figure 1.2.7-2 shows that carbonates generated during icehouse conditions primarily consist of unstable $CaCO_3$, aragonite and high-Mg calcite. In contrast, stable $CaCO_3$, low-Mg calcite is primarily associated with greenhouse conditions (Coe, 2003, Sandberg, 1983).

Thus, carbonate characteristics reflect the environmental conditions and type of organisms producing them at their time of formation. For carbonates, James Hutton´s (1788) uniformitarian paradigm "The present is the key to the past" may be said to relate to process rather than product.

### 1.2.8 Porosity and permeability in carbonate rocks

Porosity and permeability are important parameters when considering flow properties in rocks. Porosity in carbonate rocks is far more complex than in siliciclastics; this is partly due to the organic origin of most carbonate rocks, but also because their susceptibility to alteration. Porosity in carbonates can be divided into "fabric selective" and "non-fabric selective" (Figure 1.2.8-1). Fabric selectivity implies that the porosity is controlled by the grain and crystals morphology or other structures in the rock; pores do not cut or intersect these structures. The non- fabric selective porosity, on the other hand, exhibits pores that that can cross-cut primary grains and depositional fabrics. In contrast to the fabric selective pores, non-fabric selective pores can exceed the size of any single primary framework element. (Scholle and Scholle, 2014, Lønøy, 2006).

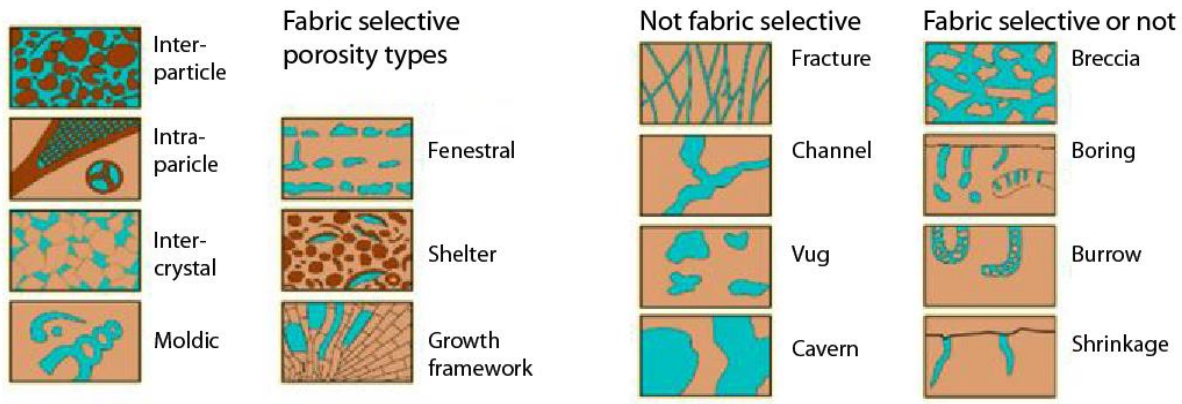


*Figure 1.2.8-1 Porosity Classification in Carbonate rocks modified after (Choquette and Pray, 1970) and (Scholle and Scholle, 2014). We differ between fabric selective-, not fabric selective-, and fabric selective or not porosity types.*

A significant part of the porosity in carbonate rocks may be non-connective, this implies that the rock can be porous as a football, but individual pores are not connected which results in the rock having little or no permeability. As an example, Scholle and Scholle (2014) presented that this can occur by porosity inversion during meteoric diagenesis. Former pores are filled with calcite cement and the original carbonate grains dissolve. The porosity stays more or less the same, but the connectivity between pores may be completely lost.

Lønøy (2006) claims that the high degree of variation of porosity in carbonate rocks, makes the relation between permeability and porosity hard to quantify. It follows that generating predictive models for reservoir quality is difficult, and often forms a significant source of uncertainty when calculating hydrocarbon reserves in carbonate rocks. Lønøy (2006) further presents plots with a relationship between porosity and permeability for different pore systems. This can be used to determine permeability values for input in reservoir models in carbonate reservoirs, when knowing the porosity. One other challenging aspect in addition to the high variation in porosity, is prediction porosity in buried carbonate systems. Reservoir models represent a body of rock, often thousands of meters below the surface. Some attempts of making predictable graphs plotting porosity versus depth are done by Brown (1997), Goldhammer (1997) and Schmoker and Halley (1982). These graphs are presented in Appendix 7.2. It seems that porosity varies between 5 and 20 % on a typical hydrocarbon reservoir depth of 2000 meters below mean sea level.

### 1.2.9 Diagenesis

Alterations affecting sediments after their initial deposition are labelled diagenesis. Diagenesis is divided in near-surface (meteoric) and burial (shallow and deep burial). See Figure 1.2.9-1 and Figure 1.2.9-2 for an overview of diagenetic processes and products.

Early diagenesis begins immediately after deposition and is significantly influenced by depositional factors, including rates of sedimentation, pore water chemistry, frequency of exposure, and other factors (Scholle and Scholle, 2014). Later diagenesis modifies the products of earlier events. Scholle (2014) and Scholle and Scholle (2014) state that one cannot really understand or predict reservoir properties without examining the combined influence of depositional patterns, early diagenetic changes, and late diagenetic modifications. They furthermore claim that burial diagenesis is commonly is overlooked, as it can be hard to distinguish from meteoric diagenesis. Burial diagenesis alters the rock through mechanical/physical compaction, chemical compaction, cementation, burial dolomitization, fracturing and secondary dissolution (Choquette and James, 1987). The Table 1.2.9-1 below shows the different processes in burial diagenesis

*Table 1.2.9-1 Burial processes. Modified from (Choquette and James, 1987, Scholle and Scholle, 2014)*

| Process | Products |
|---|---|
| Physical/mechanical compaction | Dewatering, grain reorientation, plastic or brittle grain deformation. This reduces thickness, porosity and permeability of the rock. |
| Chemical compaction | Pressure solution, solution seaming, and stylolitization creates ions for new carbonate cement. This reduces thickness, porosity and permeability of the rock. |
| Cementation | Typically works with chemical compaction. Mosaic to very coarse calcite and saddle dolomite. |
| Burial dolomitization | Anhedral-crystalline dolomite, generally coarse. |
| Fracturing | Fractures |
| Secondary dissolution | Solution porosity (intermediate to late stage). |

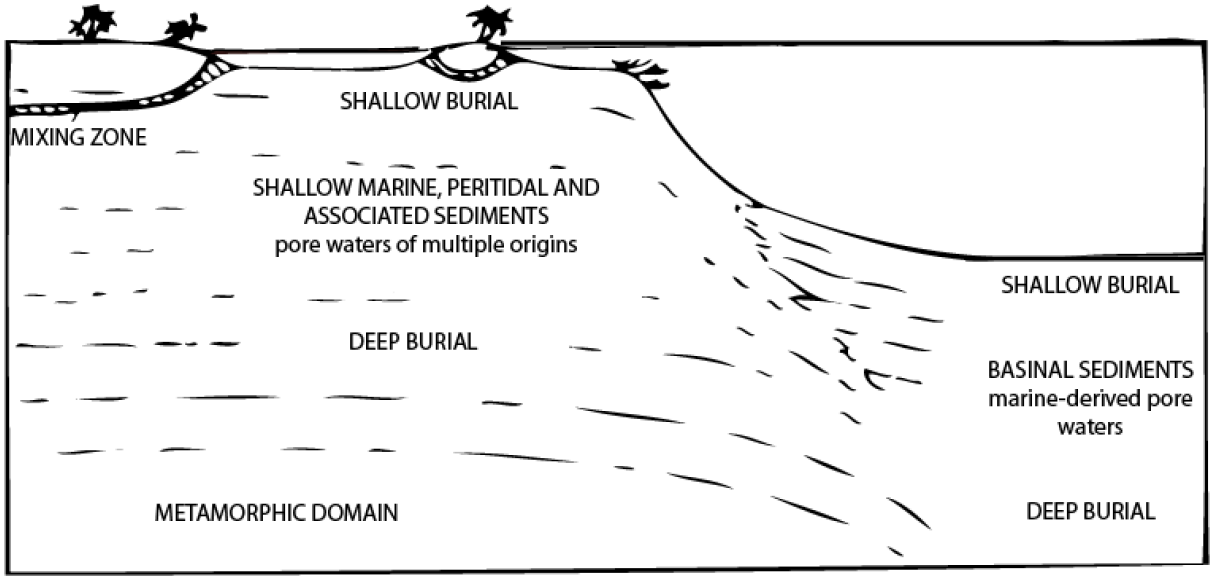


*Figure 1.2.9-1 Burial diagenesis. Figure modified from (Choquette and James, 1987)*

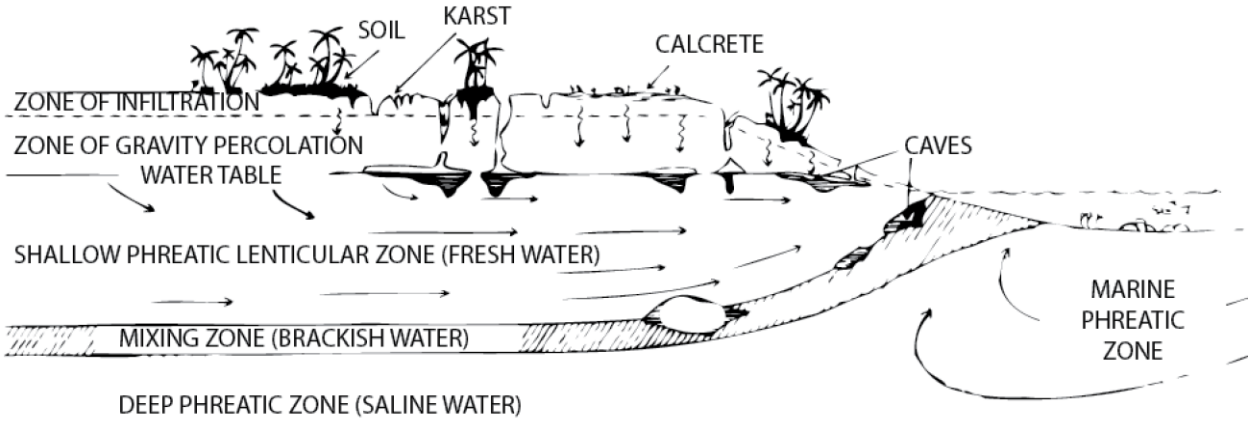


*Figure 1.2.9-2 Meteoric alteration, modified from (James and Choquette, 1984)*

When carbonate platforms become exposed in either an low-stand- or regressive systems tract setting, meteoric alteration of the carbonate rock begins. Scholle and Scholle (2014) define meteoric diagenesis as "*any alteration that occurs at or near the earth´s surface and caused by surface derived fluids"*. Most carbonates undergo meteoric diagenesis at some point during their lifetime. Exposure of carbonate platforms can take place as a result of eustatic sea level fall and/or isostatic and tectonic uplift, and circulation of fresh water may occur far below the surface of the earth. James and Choquette (1984) distinguish two contrasting zones where meteoric alteration

takes place; the vadose zone and the phreatic zone. The vadose zone, also called the unsaturated zone, lies closest to the surface and is divided into the zone of infiltration and the zone of gravity percolation. The phreatic zone, which lies below the vadose zone, is also called the saturated zone. The transition between these zones is the water table. The phreatic zone is further divided into the fresh water and saline water zone. The transition between the two is characterized by brackish water. Figure 1.2.9-2 illustrates that the typical epigenic karst processes occur within these two transition zones (saturated to under-saturated and freshwater to saline water. The mineralogical composition of carbonate sediments is a major factor controlling the intensity and style of diagenetic alteration and the reservoir potential of carbonate rocks through time.

Diagenesis can have a positive or negative influence on porosity and permeability of the rock. On the negative side, Scholle and Scholle (2014) list filling of pore space by cements generated during dissolution of less stable grains, the inversion of porosity (discussed earlier) which decreases the rock´s permeability, and the formation of soil crusts that decrease both porosity and permeability. These features can be outweighed by processes enhancing porosity and permeability. *Spot welding* of grain-to-grain contact (as in beach rock) increases the strength of the rock, making it more resistant to compaction and porosity loss during burial. Dissolution of chemically unstable grains may form secondary porosity if $CaCO_3$ can be transported out of the system, and precipitated as cement in the same body of rock. Solution can enlarge fractures in the rock, and ultimately result in local formation of caves. (Scholle and Scholle, 2014, James and Choquette, 1984). As introduced in Chapter 1.2.2, the dissolution process of carbonate rocks follows the equations below (Boggs, 2012).

$$CO_2 + H_2O \leftrightarrow H_2CO_3$$

$$H_2CO_3 + CaCO_3 \leftrightarrow Ca^{2+} + 2HCO_3^-$$

When carbon dioxide comes in contact with rainwater, carbonic acid can easily dissolve limestone. Factors that influence the process rates are burial depth, mineralogy, pore water chemistry and clay content.

## 1.3 Karst and karst collapse

### 1.3.1 Karst

We here use the term *karst* as defined by Choquette and James (1988) as "*…all diagenetic features-macroscopic and microscopic, surface and subterranean-that are produced during the chemical dissolution and associated modification of a carbonate sequence*." The process is referred to as karstification. Karst features (Figure 1.3.1-2) develop in soluble rock (evaporite, limestone, carbonates etc.) when it is brought into contact with meteoric water through uplift or a major sea-level fall (Tucker, 2011). Loucks (1999) and Scholle and Scholle (2014) add that karst may also be formed by corrosive (hydrothermal) fluids from the subsurface. Typical geomorphic karst features include; karren, dolines, grikes, cave systems and springs (James and Choquette, 1988). The scale of the karst systems is intimately linked to the intensity of karst processes and the composition of the rock. Pervasive karstification may ultimately produce cave systems, which may vary from narrow channels to large caverns (Loucks and Handford, 1996). According to Ford (1988) cave passages can be classified as true cave conduits when reaching a diameter larger than 5-10 mm. This represents the minimum tube diameter at which turbulent flow becomes competent enough to transport sediment. The sediment filled water can contribute to further widening of conduits through mechanical abrasion of the walls.

Karstification and collapse processes in cave systems are to a large extent controlled by host rock properties such as stratigraphy, structural geology (fractures/faults/folds), drainage patterns and pore networks, as well as climate, exposure time and position (including fluctuation) of the water tables. Since dissolution accelerates when temperatures rise, caves develop faster in humid and warm climates. Caves form where dominant antecedent pore network consists of fractures and bedding planes in a rock body with minor matrix porosity. Then acidic water is forced through the same passages, and can widen the passages further.

There are many different features and characteristic forms related to karst. Loucks (1999) illustrates this in Figure 1.3.1-2 below. When regional or local base levels fall, the earlier phreatic passages enter the vadose zone. This can initiate the creation of canyons, keyhole-shaped passages and vertical shafts if the water flow is continuous. At this stage former phreatic passages and caves, may start to collapse and fill in, but they commonly also experience further dissolution and excavation by processes active in the vadose zone.

The width of caves passages can vary considerably. Loucks (1999) states that there is only a 1% chance of cave passages in USA to be more than 12 meters wide. This is based on unpublished measurements on cave passage width and height collected by Art Palmer presented by Loucks (1999). The statistics of cave passage width is presented in Figure 1.3.1-1 below. Passages wider than 12 meters are uncommon except for occasional chambers that can be more than 100 meters across. An extreme example is the Sarawak Chamber in Borneo, which is approximately 600 meters across, however most cave passages collapse before they reach a width more than 30 meters (Loucks, 1999).

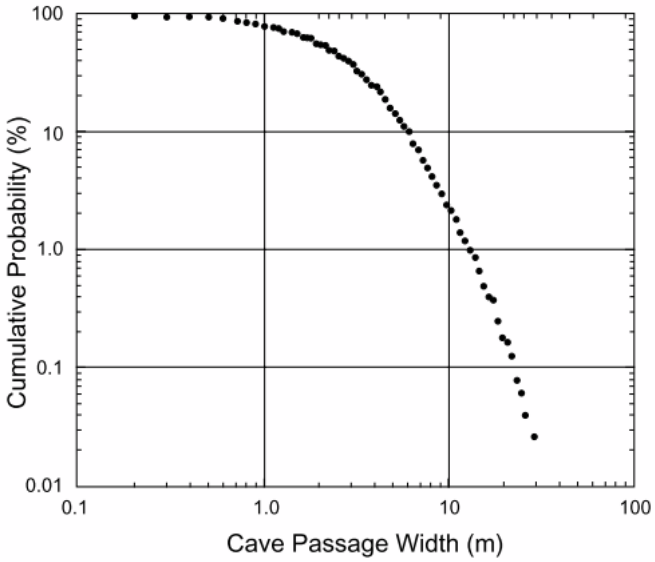


*Figure 1.3.1-1 Statistics on cave passage width. Based on measurements made by Art Palmer. Figure derived from (Loucks, 1999).*

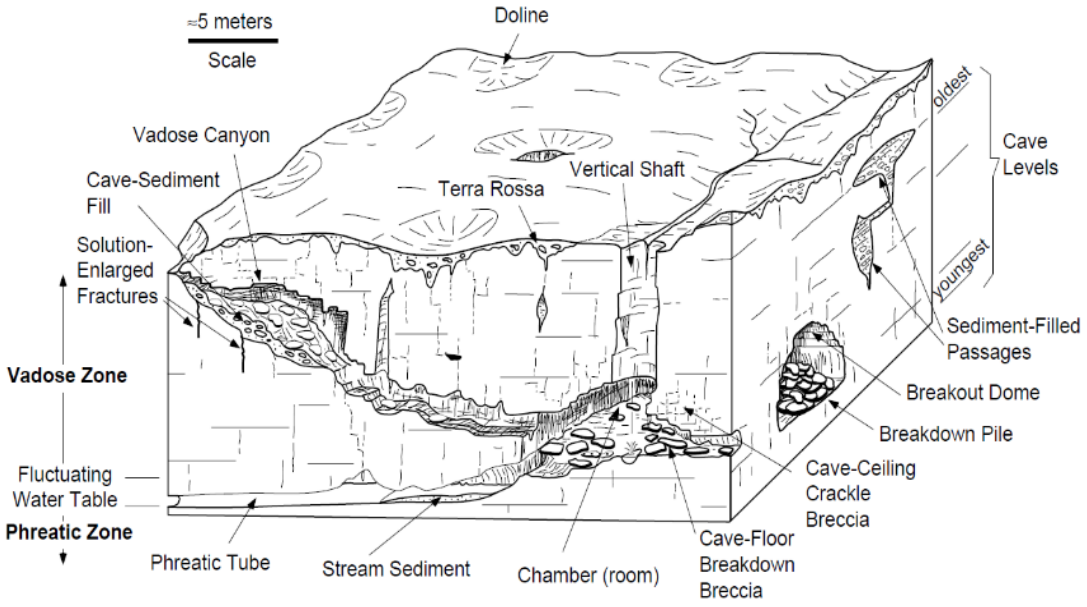


*Figure 1.3.1-2 Schematic figure of vadose and phreatic cave processes. Figure is taken from (Loucks, 1999) which is modified from (Loucks and Handford, 1992).*

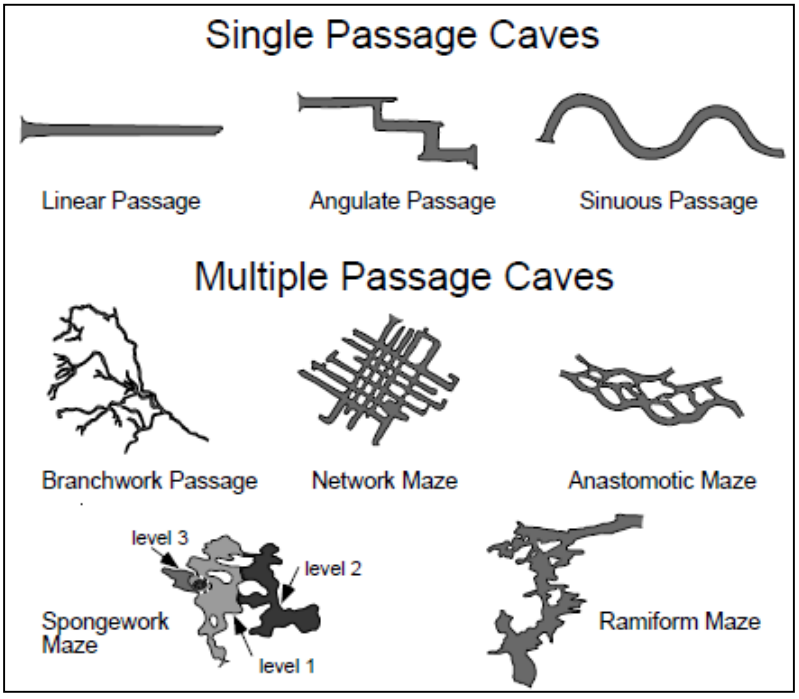


*Figure 1.3.1-3 Cave geometry from (Loucks, 1999)*

Cave geometries vary from linear single passage caves to multiple passage ramiform cave maze. The various cave passages are shown in Loucks´ (1999) Figure 1.3.1-3. These cave geometries are shown in map-view, but as stated above, caves can be highly three-dimensional as flow, and thereby dissolution, can be influenced by changing local base levels as well as the pre-existing fracture patterns. This creates several levels of the different cave geometries, and can lead to hugely complex channel and cave structures. Fracture direction, joints, rock stability, climate, and changes in water table control cave geometries (Loucks, 1999). If these factors are known, they provide important clues to forecast kind of cave geometries can be expected in certain formations.

Palmer (1991) classifies karst caves into epigenic and hypogenic caves. Epigenic caves form the starting point for most paleokarst reservoirs, and result from near- surface weathering of soluble rock. In continental environments, the dissolution of carbonates, is caused by surface runoff (rainwater) that is enriched with carbon dioxide and creates carbonic acid, like discussed in Chapter 1.2.1. In coastal environments, dissolution typically occurs where marine and meteoric waters mix (see Figure 1.2.9-2). Hypogenic caves, on the other hand, are formed by fluids from the deeper subsurface that are enriched by sulfuric acid. Whereas these caves are less common and formed by a different process than the epigenic caves, they are likely to follow the same burial history as epigenic caves.

### 1.3.2 Paleokarst

James and Choquette (1988) defines *paleokarst* as ancient karst. Loucks (1999) however defines paleokarst as karst systems that are no longer active. The latter provides a more precise description, as it specifies that the system is not only ancient, but also has to be inactive. Similarly *Paleocave* systems are defined as cave systems that are no longer physically related in time and or space to any active karst process that formed them (Loucks, 1999). This de-activation of the karst-forming processes can be caused by physical isolation, cessation of processes and burial which over time causes infill, collapse, compaction and mineralization. However, paleokarst systems may be re-activated and karst features often exhibit patterns of more than one karstification event (see Figure 1.3.3-2).

De-activation of the karst forming process is commonly followed by infilling of cavities by a wide range of sediments and cements. Loucks (1999) proposed a compositional classification scheme for cave infills (Figure 1.3.2-1). In this system, cave infill is classified according to its mixture of three end-member components: crackle breccia, chaotic breccia, and cave sediment.

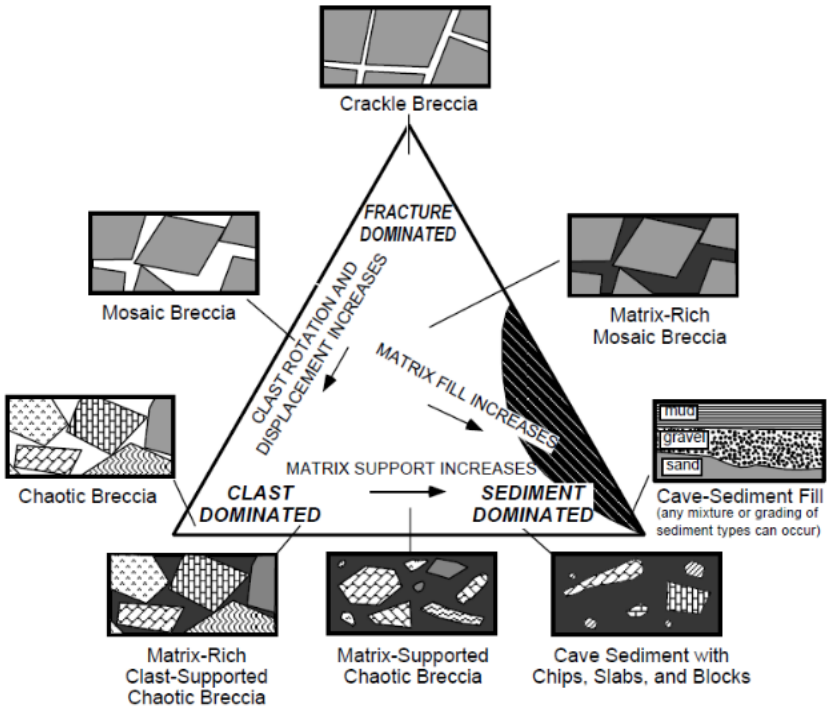


*Figure 1.3.2-1 Cave infill classification from (Loucks, 1999)*

Breccias are commonly associated with paleokarst. They typically form due to fracturing, stoping and collapse of caves, and commonly consist of angular clasts of the host rock with maximum clast sizes corresponding the spacing of fracture patterns in the host rock. Breccias can be classified according to the degree of internal displacement between clasts: crackle breccia show only minor displacement between clasts, and essentially represent pervasively fractured host rock. Mosaic breccia exhibit more displacement between clasts, but blocks can still be fitted together like a puzzle; chaotic breccia consist of jumbled blocks. The latter may contain evidence of having been subjected to transport and could include exotic clasts originating from collapse of overlying formations or from lateral transport into the cave. The composition and amount of matrix material in all these breccias may vary.

Paleokarst features are intimately linked to the karst features present at the time the karst process becomes inactive. Paleokarst systems are therefore likely to inherit some geometrical properties from the pre-existing karst system. Understanding the modern karst systems can therefore give important clues to understanding paleokarst systems, in particular with respect to karst formation, scale relationships, geometries and how their spatial distribution is linked to host rock lithology and structural geology.

### 1.3.3 Burial and diagenesis of paleokarst

Paleokarst systems are most commonly products of near-surface processes of karstification, with later burial and compaction. They form an important class of hydrocarbon reservoirs. Loucks (1999) states that while karst systems are well-studied; they are commonly not integrated into paleokarst studies. Paleocave data is limited to outcrop and well data, but burial evolution can be deciphered by comparing modern examples with different stages of ancient ones. Well-exposed outcrops are rare, and the spatial organization of the ancient cave system is difficult to establish even when using geophysical methods and well data, which in many cases can be difficult to interpret or lack sufficient spatial resolution to allow detailed reconstruction to be made. (Loucks, 1999)

Outcrops and well data only show parts of the system, but do not provide the full picture with respect to geometry and properties. Therefore, to get an impression of the 3-dimensional geometry, it is necessary to look at modern cave systems and use them as proxies. For karst, like carbonates, the term “The present is the key to the past” discussed earlier, refers more to the process than the result. Basically, every cave system in carbonate rocks is formed by the same, limited set of processes, but the resulting geometry differs due to local factors such as stress direction fractures and faults in the rock hosting cave formation, and the level of the transition zones where caving occurs. (Scholle and Scholle, 2014, Loucks, 1999).

Loucks (1999) shows a conceptual evolution of a single cave passage from its formation in the near-surface phreatic zone to its collapse during burial (Figure 1.3.3-1). The figure is based on a falling base level e.g. the cave system “moves” from the phreatic into the vadose zone. Loucks (1999) further explains that breakout domes, like the one shown in the figure, commonly form when base level drops. This because water supports 40% of the ceiling weight (White and White, 1969). When this support is lost, as water is drained out of the cave, ceiling and walls may collapse. From the collapse follows infill of chaotic breakdown breccia inside the former phreatic tube. Since the cave is collapsing, overlying strata tend to fracture, fault and sag downwards. During burial, the former tube gets filled with all sorts of breccia types and cave sediment infill (se Figure 1.3.2-1 above). A halo of crackle breccia surrounds the former cave passage as a result of stress relief in overlaying strata. As shown in Figure 1.3.1-2, compaction-related structures tend to radiate beyond the circumference of the cave passage. This produces a larger body of rock with

enhanced permeability than if just the former phreatic tube was filled with sediment. It is obvious that the former volume of the cave becomes distributed as pore space the new volume of breccia if no compaction has taken place. The collapse stops when the former cave is completely filled with cave infill.

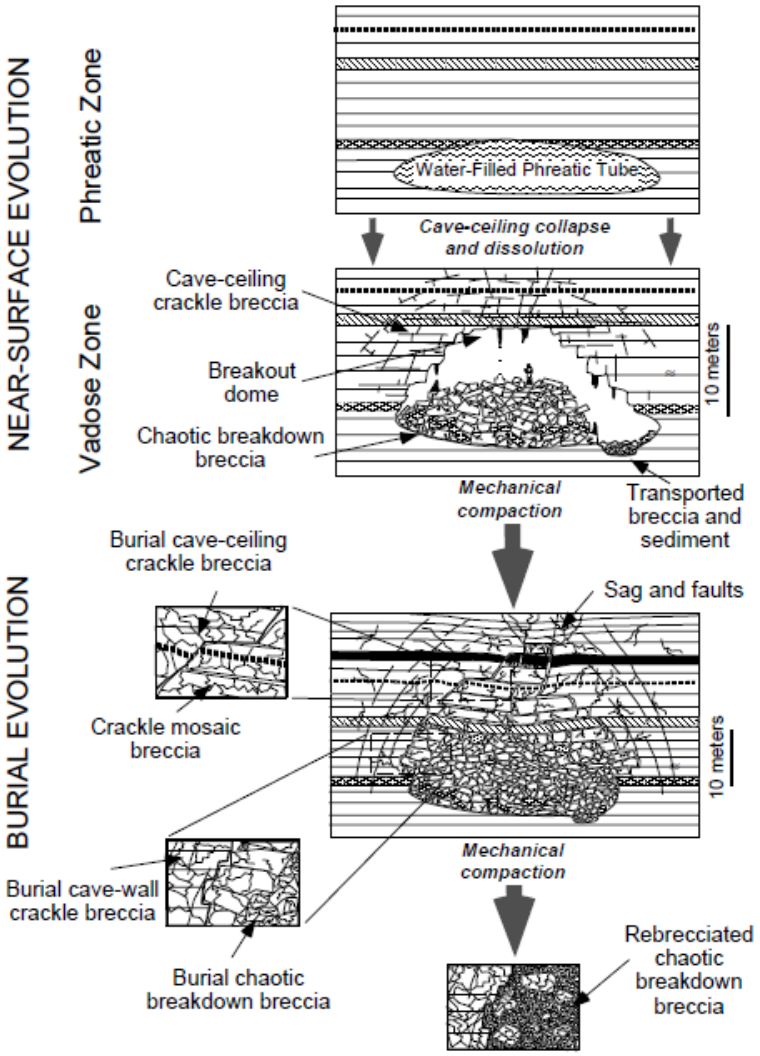


*Figure 1.3.3-1– Collapse of paleocave system from (Loucks, 1999) modified after (Loucks and Handford, 1992)*

The complexity observed in formations exhibiting paleokarst, in particular with respect to paleokarst formations being the result of multiple processes, can be illustrated by an example from a Paleozoic limestone succession in Billefjorden, Svalbard. The photographs below, clearly illustrate how cave infill (B2) can occur inside an older cave collapse breccia (B1). Furnée (2013) states that the interesting part of this location is the perfect indication that there has been more than one event of cave formation and collapse.

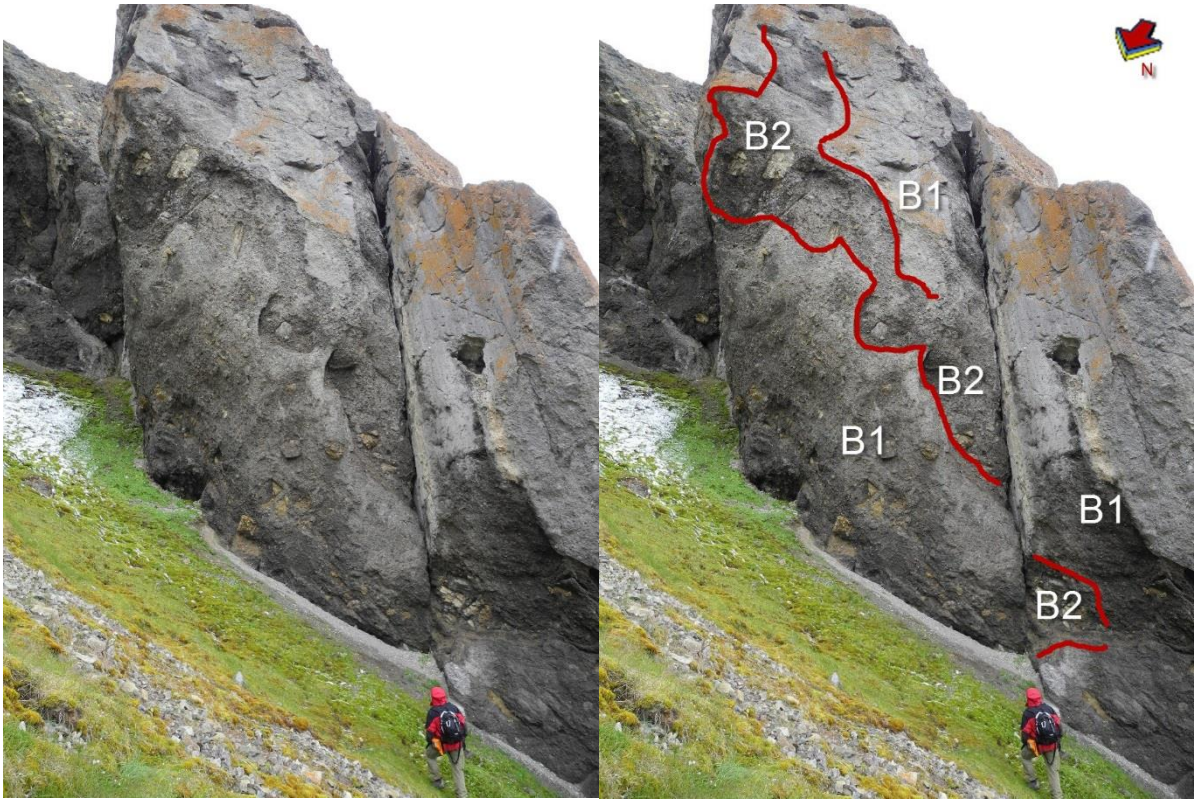


*Figure 1.3.3-2 Cave infill in cave collapse breccia. Note breccia B2 in B1. Jan Tveranger as scale. Photo: Jon Petter Furnée. Figure modified from (Furnée, 2013)*

Loucks (1999 and 2007) claimed that most paleocave reservoirs are not products of isolated collapsed passages but rather products of coalesced collapsed paleocave systems. These systems can be several thousands of meters long and across. This is an important concept because it shows that exploration targets on collapsed paleokarst reservoirs are likely to be much larger than individual cave systems, and likely to be connected through fractures systems. Figure 1.3.3-3 shows a schematic diagram of the evolution of coalesced collapsed paleocave systems. These systems develop as a result of several stages of development. As the multi-cave system subsides, wall- and ceiling rock collapses, and may intersect with fractures from other collapsed passages and older breccia's within the system. Loucks (1999) and several other authors (Loucks and Handford, 1992, Hammes, 1996, Mazzullo and Chilingarian, 1996, Kerans, 1988) explain that the result of this process gives a spatially complex reservoir system, and a much larger exploration target, than a single phreatic tube. Since the spatial complexity ranges from pore level to regional scale, qualification becomes difficult. The overall pattern of spatial complexity is controlled by original cave geometry and the number of cave passages. The distribution of porosity is controlled by distribution of cave-sediment fill. The original areal extent of rock with porosity and permeability enough to support fluid flow increases as the system collapses and fractures the rock around the former passages. In addition, cementation during burial may totally change and reduce porosity of the system. The final porosity and permeability is highly complex and spatially variable. Loucks (1999) concludes that karst-related paleocave systems represent an important class of carbonate petroleum reservoirs, and understanding their origin and burial history helps in exploring and developing these reservoirs. Stein-Erik Lauritzen (2015, pers. comm., 28 April), on the other hand, casts doubts on Loucks´ (1999) idea of coalesced collapsed paleocave systems. The doubts are based on observations of the strength of perforated metal plates, where the metal plates become stronger with holes. He further claims that isolated cave systems, do not merge into one big breccia body as easily as Loucks´ (1999) describes, because the system becomes stronger for each cave (up to a certain point) as for the metal plate.

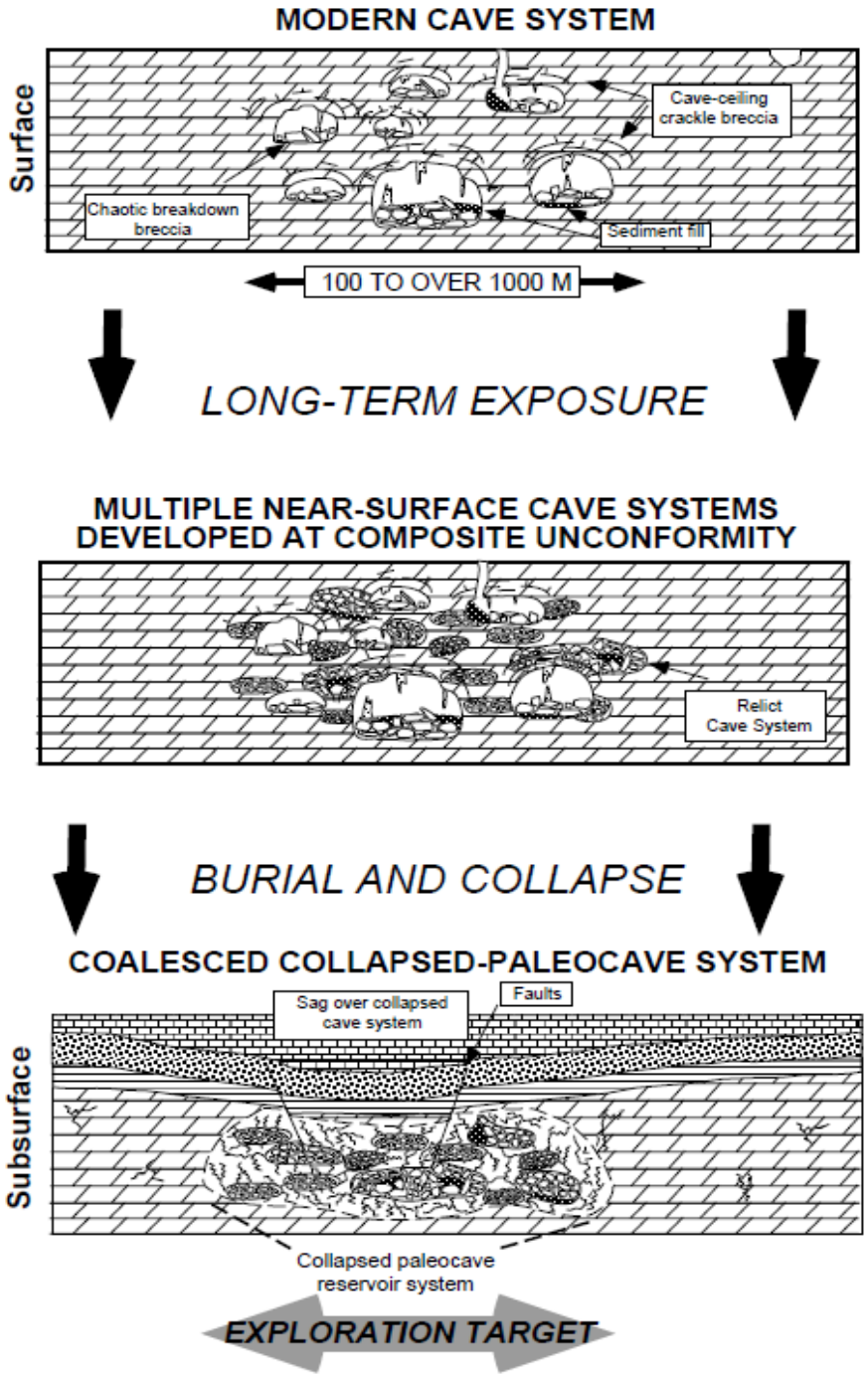


*Figure 1.3.3-3 Coalesced collapsed paleocave system from (Loucks, 1999). The figure shows how several cave passages can interact during burial and create a larger reservoir system and exploration target*

### 1.3.4 Cave collapse model

The collapse of a cave can be expressed as an increase of its initial cross-sectional radius. A simple geometric approach is carried out by an equation (see equation (1) below) derived from Stein-Erik Lauritzen (2014, pers. comm., 12 September). If the host rock is considered otherwise non-porous, and no compaction is taking place, the total amount of pore space stays unchanged after collapse. This initial porosity can be calculated based on the diameter of the cavities. As the cave collapses the radius of the cavity increases, but the expanding cavity is simultaneously filled in with breccia. Assuming that the collapse is evenly distributed along the caves periphery, the increase in radius caused by collapse can be approximated as being equal to the inverse of the square root of the porosity.

$$\pi {R_2}^2 = \frac{1}{\emptyset}\pi {R_1}^2 \quad \rightarrow \quad \frac{{R_2}^2}{{R_1}^2} = \frac{1}{\emptyset} \quad \rightarrow \quad \frac{R_2}{R_1} = \frac{1}{\sqrt{\emptyset}} \tag{1}$$

Porosity, $\emptyset$, is expressed as a decimal fraction, and not in percent. $R_2$ is radius after collapse, while $R_1$ is radius before collapse. A complete list of symbols is presented in Appendix 7.1.4.

Se the Table 1.3.4-1 and its corresponding graph (Figure 1.3.4-1) for resulting values of the calculation. The values marked with green color indicate the three cases for cave radius/porosity selected as input to the reservoir models subjected to detailed study in this thesis. The radius after collapse ($R_2$) was initially set to be twice the radius of the original cave radius ($R_1$). The other $R_2$ values (12 and 14 meters) were introduced to test the effect of radius increase on the production curves. For modeling simplicity the interval of 2 meters ($10 \rightarrow 12 \rightarrow 14$ meters) was used as the initial grid has grid cells with dimension $2\text{m} \times 2\text{m} \times 2\text{m}$.

*Table 1.3.4-1 Table showing the relationship between resultant porosity (Ø) and $R_2/R_1$ in a collapsed cave. The green values are the three radius- and resulting porosity cases used as input in the reservoir model.*

| Porosity, Ø | $R_2/R_1$ | $R_2$ |
|---|---|---|
| 1.000 | 1.00 | 5.0 |
| 0.950 | 1.03 | 5.1 |
| 0.900 | 1.05 | 5.3 |
| 0.850 | 1.08 | 5.4 |
| 0.800 | 1.12 | 5.6 |
| 0.750 | 1.15 | 5.8 |
| 0.700 | 1.20 | 6.0 |
| 0.650 | 1.24 | 6.2 |
| 0.600 | 1.29 | 6.5 |
| 0.550 | 1.35 | 6.7 |
| 0.500 | 1.41 | 7.1 |
| 0.450 | 1.49 | 7.5 |
| 0.400 | 1.58 | 7.9 |
| 0.350 | 1.69 | 8.5 |
| 0.300 | 1.83 | 9.1 |
| 0.250 | 2.00 | 10.0 |
| 0.200 | 2.24 | 11.2 |
| 0.173611 | 2.40 | 12.0 |
| 0.150 | 2.58 | 12.9 |
| 0.127551 | 2.80 | 14.0 |
| 0.100 | 3.16 | 15.8 |
| 0.050 | 4.47 | 22.4 |
| 0.010 | 10.00 | 50.0 |

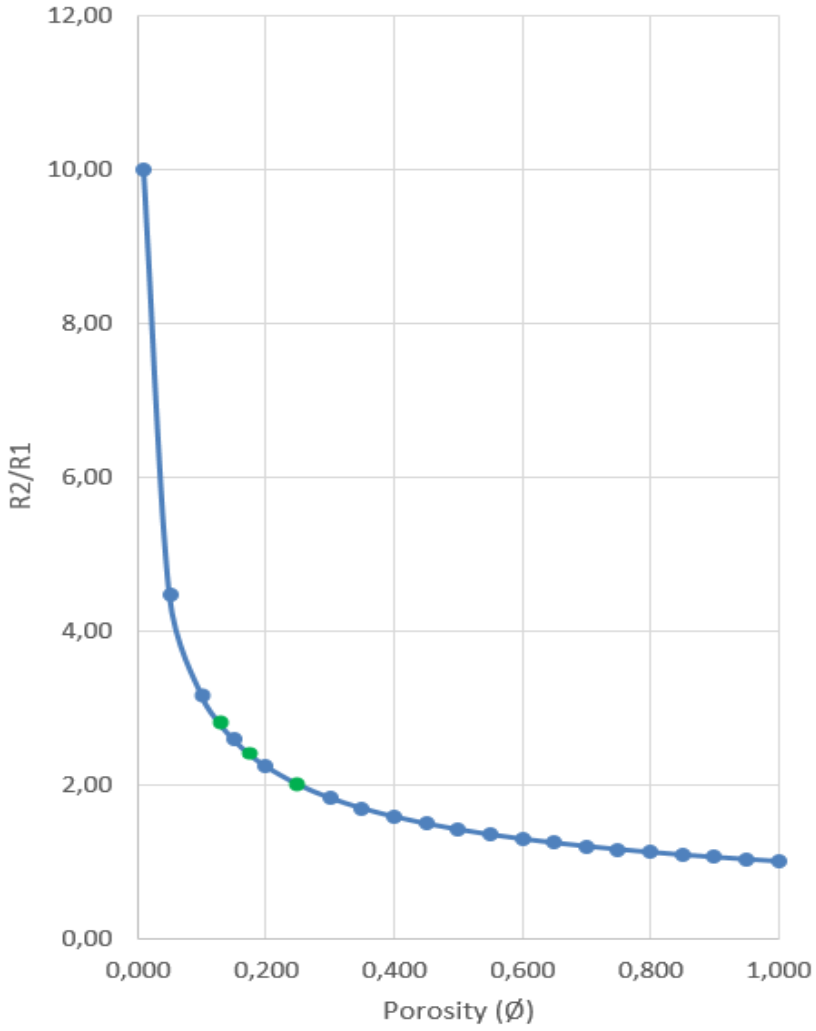


*Figure 1.3.4-1 Plot showing the relationship between porosity (Ø) vs. $R_2/R_1$ in a collapsed cave. Values shown in green values in the table are the three cases used as input in the reservoir model.*

Figure 1.3.4-1 shows that if the radius of the cave is increased by a factor of two through collapse ($R_2 = 2 \times R_1$), the cross-section area of the collapsed cavity is four times larger than that of the initial cave (Area $2 = 4 \times$ Area 1). If the initial cavity has a porosity of 100%, this translates into an average porosity of 25% in the collapsed and infilled cave.

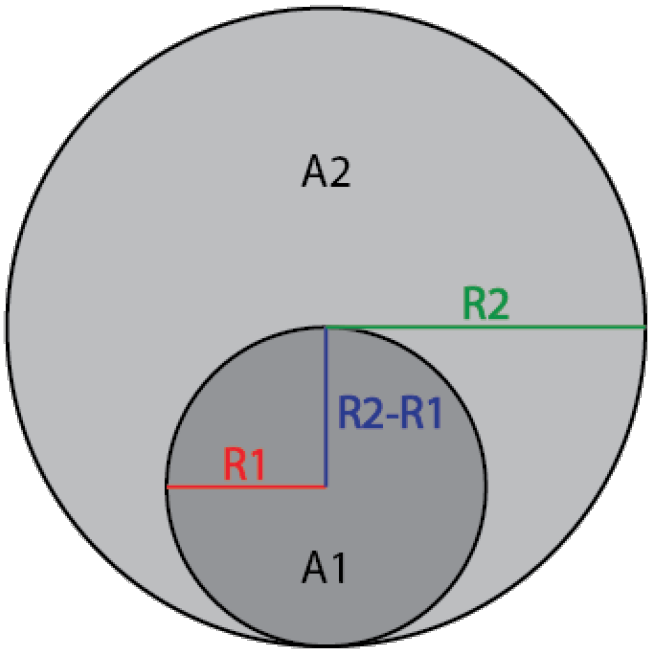


*Figure 1.3.4-2 Conceptual cross sectional view of cave before (A1) and after collapse (A2) $R_1$ and $R_2$ are the radii of the cavity before and after collapse, respectively. Note that the center of circle showing the cave after collapse is shifted upward to maintain the position of the cave floor.*

This approximation can be further improved: Collapse is a gravity-driven process; thus brecciation and gravity-driven expansion of the cave will not affect the initial cave floor. In order to provide a reasonable approximation of the resulting geometry of the collapsed cave, the center point of the collapse has to be moved $R_2$-$R_1$ up to maintain the same cave floor before and after collapse (see Figure 1.3.4-2).

The porosity of the breccia filling the collapsed cavity is not likely to be homogeneously distributed. For a collapsed cave filled purely by locally derived breccia, it is reasonable to assume a general trend with the highest porosity values near the position of the initial cavity and decreasing toward the margin of the collapse dome where it may show a gradual transition from inter-particle porosity to fracture porosity (e.g. Kerans (1988), Nordeide (2008), see Figure 1.3.3-1 and Figure 1.3.4-3). However, different porosity patterns and trends can be expected if the cave is filled by

cements and/or allochtonous sediments, in particular as larger pore spaces in the initial collapse breccia get filled-in by more fine-grained sediments.

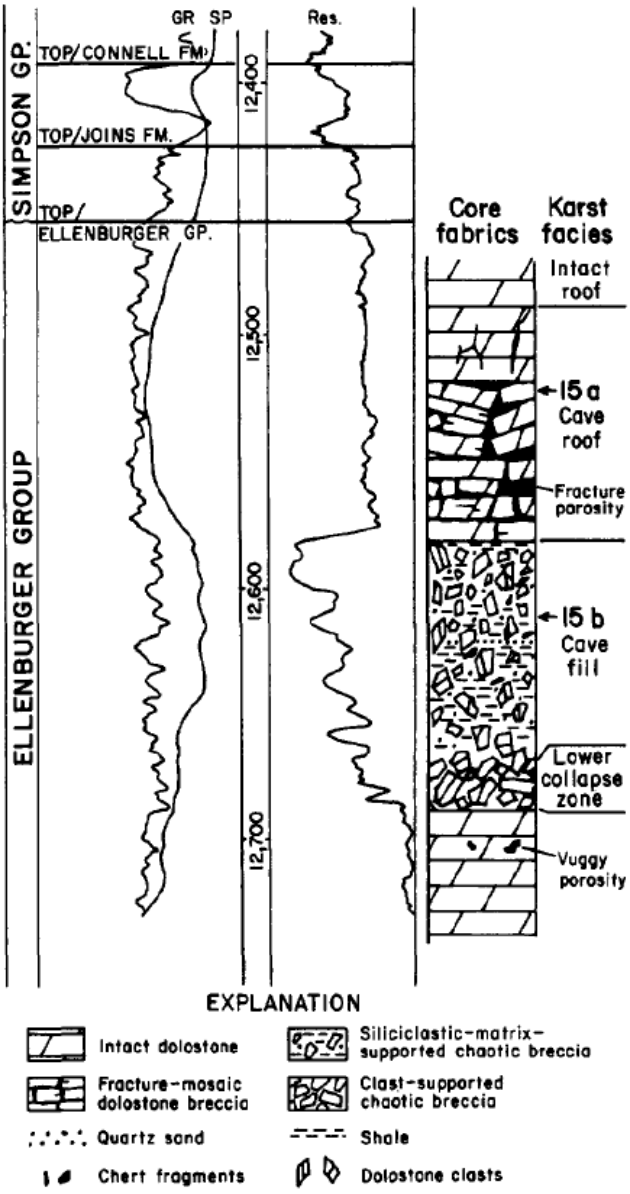


*Figure 1.3.4-3 Core and well logs showing a cave-infill/collapse succession from the Ellenburger Group, western Texas (Kerans, 1988)*

### 1.3.5 Compaction of collapsed cave model

Burial induces a vertically oriented pressure on the collapsed caves, and may cause additional fracturing, porosity reduction of the cavity infill and pressure solution/recementation. It may also conceivably change the overall geometry of the collapsed cave cross-section by flattening it; in particular if the cave is not completely filled by prior to compaction. The extent of these effects is closely linked to the mechanical strength of the host rock as well as burial depth, and needs to be considered when performing porosity calculations along the lines suggested in the preceding section. The effect of compaction is dependent on the time of occurrence. If the collapse occurs early during burial, the effect of compaction on the collapse geometry is greater than if it occurs late. For the porosity estimates employed in the models constructed as part of the present study, the impact of compaction has not been included.

The width of the collapsed cave will be little affected by the compaction. If the host-rock is a limestone with little porosity, compaction will be minor. If the host rock is a porous limestone, the compaction can be significant. The former is the more likely case, as cave systems are more prone to develop in rocks with low initial porosity.

However, none of the tools used in this study (see Chapter 1.4.2) include modules for explicit handling of compaction. There are dedicated rock-mechanical modeling tools (e.g. VISAGE by V.I.P.S and Eclipse Geomechanics by Schlumberger) some of which offer coupled flow and mechanical modeling. Simulation times for these are typically one to three orders of magnitude longer than pure fluid flow simulation, and they are generally not employed as part of the standard industrial modeling workflow. (Doornhof et al., 2006).

Based on these considerations compaction effects are not included in the present modeling study.

## 1.4 Modeling and simulation of paleokarst reservoirs

### 1.4.1 Previous work

The architectural and petrophysical complexity of collapsed karst systems make them very challenging to model. Providing realistic geo-models which can serve as a reliable input to forecasting production behavior is tricky because a range of processes are involved in the formation of such systems. Some of these have been addressed by previous workers.

Pardo-Igúzquiza et al. (2011, 2012) and Collon-Drouaillet et al. (2012) show different approaches to capture cave networks. Pardo-Igúzquiza et al. (2011) analyzes three-dimensional networks of karst conduits, while Pardo-Igúzquiza et al. (2012) builds further with stochastic simulations of these features. Collon-Drouaillet et al. (2012) stresses the fact that simulation of three-dimensional karstic networks is required to build realistic carbonate reservoir models. The paper focuses on branchwork karst, and how to simulate such networks with realistic, geologically consistent geometries.

Several oral presentations hosted by AAPG (Feazel, 2010, Xiaoqiang et al., 2012) show ways of modeling paleokarst reservoirs. Xiaoqiang et al. (2012) presents 3D modeling of the Tahe oil field in China, which, as mentioned in the introduction (Chapter 1), is a paleokarst reservoir. The model is based on a geostatistical analysis of karst geology as well as probability from both well and seismic. Feazel (2010) presents the use of modern cave systems as analogs for paleokarst systems, and illustrates that cave surveys can be used to assign properties in geocellular models of karsted reservoirs. Feazel (2010) further presents examples for seismic forward modeling and seismic velocity models with different sensitivities with respect to cave size and cave infill.

Petrophysical properties in carbonate rocks and collapse breccia is among others described by Lønøy (2006), Lucia (1995, 2004, 2007), and Loucks (1999, 2007). They all specify the complexity in these rocks, and describe the wide range of petrophysical values within the different cases. Lønøy (2006) is used in this thesis to assign average permeability to different porosity cases.

Studies related to flow behavior in paleokarst reservoirs have been carried out by former master students at Uni CIPR (Centre for Integrated Petroleum Research). Common for them all, is the vertical breccia pipe aspect of paleokarst.

Nordli (2009) investigated the impact of breccia pipe features on fluid flow behavior in a reservoir setting and assessed their relative influence. The study lists the factors that are most important to include in reservoir models where breccia pipes are present. Nordli (2009) based the geological input to the reservoir models on Nordeide (2008) who quantified several properties of collapse breccia in the Wordiekammen formation (Billefjorden, Svalbard). Nordli (2009) stresses the importance of including breccia pipes in reservoir models if present, or even suspected. *"The most significant factor affecting fluid flow was found to be the magnitude of permeability contrast between the pipe and background… an increased permeability contrast will result in poorer sweep of the background volume and enhanced flow of fluids through the pipe."* (Nordli, 2009). Further Nordli (2009) states that if the reservoir model includes high permeable beds in background (structural subdivision of layers), fluids will be "lost" in these layers, resulting in poorer sweep. Nordli (2009) hereby confirms the suggestion made by Nordeide (2008), that permeable beds in background has a significant impact on fluid flow.

Dalva (2012) expanded on Nordli´s (2009) thesis by presenting a reservoir with pipes present, and investigating if the presence of breccia pipes in a reservoir could be deduced from observed production behavior. One of his major conclusions in addition to the evidence that pipes were present in the system, was that "*The breccia pipe shape can be simplified to that of a square box instead of a cylindrical (radial) shape, provided the breccia pipe volumes are kept equal."* (Dalva, 2012). This suggests that the impact of at least some paleokarst features on production can be captured even if some simplifications are employed in the modeling.

### 1.4.2 Introduction to the software

Reservoir models are primarily used for visualizing, integrating and analyzing all available datasets from subsurface reservoirs, and serve as common platforms for linking geology, geophysics, petrophysics and reservoir engineering. The integration and analysis of data coupled to geological know-how and the laws of physics make them powerful tools for forecasting reservoir properties, calculating volumes and predicting their dynamic behavior over time. Thus reservoir models are key tools for hydrocarbon exploration and production; identifying prospects and ensuring safe, optimized and financially sound field management.

The geo-modeling was performed using *RMS™ 2013* by Roxar Software Solutions; a standard industrial reservoir modeling tool. For flow simulations *Eclipse 2013.2*; a reservoir simulation tool by Schlumberger was employed. For creating a fracture rose based on cave directions, GeoRose 0.4.0, designed by Yong Technology Inc. was used.

According to Pettersen (2006) reservoir simulators "…simulate the exploitation of a real reservoir without the costs of real life trial and error, e.g. to test different productions scenarios to find an optimal one before the reservoir is actually put on production". Eclipse does this by solving numerous dynamic equations on a discretized (gridded) 3D rendering of a body of rock/reservoir populated with relevant properties, providing an accurate prediction of dynamic behavior for all types of reservoirs. (Schlumberger, 2014b).

However, "an accurate prediction" still comes with attached uncertainties, in particular if geology is involved. Forecasting-precision is mainly dependent on the accuracy of input parameters, but software implementation aspects such as grid resolution and the manner in which geological structures and properties are rendered may also affect results. Deterministic reservoir models, involving a fixed input and a single outcome (realization) are therefore of limited use if input parameters are poorly constrained. To overcome this problem reservoir models employ stochastic methods which generate a range of possible outcomes (realizations) weighed by the likelihood or probabilities of a given set of circumstances. The resulting spread of outcomes reflects uncertainty of the forecast.

The present study focuses on the impact of certain modeling parameters on reservoir performance. Thus, although stochastic modeling is the most commonly used method in “real life” settings, we

here employ sets of deterministic models in order to retain full control of the input parameters and subsequent simulation outcomes.

# 2 Methods

## 2.1 RMS; model set up and design

The study focuses on a medium scale reservoir with a constant thickness of 58 meters, and maximum length and width 670 and 255 meters respectively.

Note that underlined words in the text are explained in Appendix 7.1.3.

### 2.1.1 The Setergrotta cave

Setergrotta Cave, near Mo i Rana in northern Norway (Figure 2.1.1-1) is one of the largest limestone caves in Norway. (Lauritzen et al., 2005) (Setergrotta, 2015). The cave system mainly consist of marble and mica schist lithology. The age of Setergrotta Cave system is not determined. Estimations however, give an absolute minimal age of 15000 years. But the system is probably much older (Øvrevik, 2002). A survey of the cave geometry (Unpublished mapping data, S.E. Lauritzen and R.Ø. Skoglund 2014, pers. comm., 7 April) was used as input for the reservoir model in this thesis.

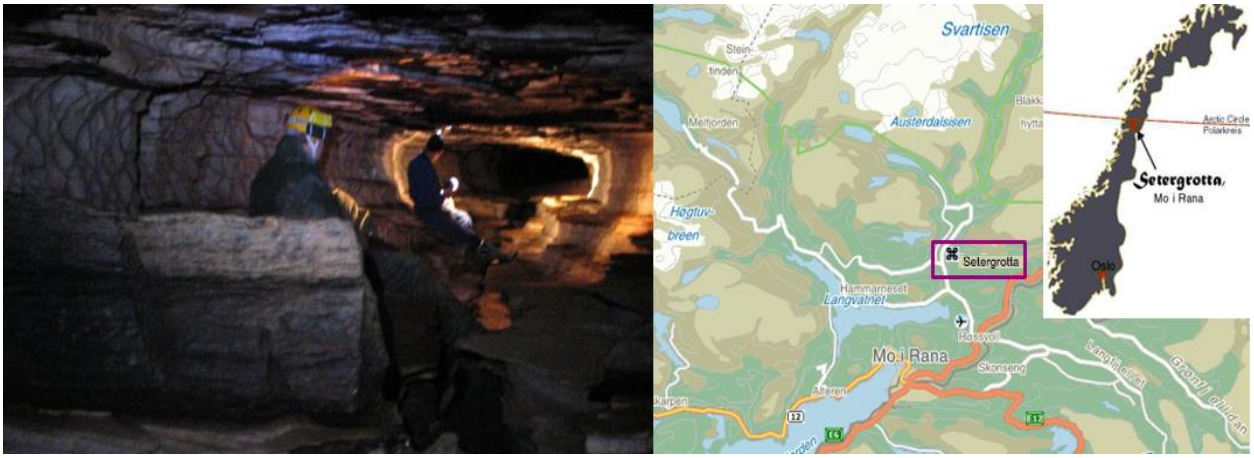


*Figure 2.1.1-1 Pictures derived from (Setergrotta, 2015)*

### 2.1.2 2D data and skeleton lines

To create a realistic cave geometry for further modeling and simulation of paleokarst reservoirs, survey points from Setergrotta Cave were used. These were imported to RMS as *general 2D data* points. The survey data include center-, wall-, floor-, and ceiling points given as local XYZ-coordinates (Unpublished mapping data, S.E. Lauritzen and R.Ø. Skoglund 2014, pers. comm., 7 April). In order to remove any negative coordinate values, the values were multiplied with (-1) and 500 meters was added to all points. This was done in Excel before importing the points as .txt-format.

In *Clipboard* an empty polygon was created, and used to analyze the path between the center points of the survey. This polygon was named *SkeletonLines*, and added to the *General 2D data*. The points for wall, floor, and ceiling, were only used to understand the geometry of the cave. See Figure 2.1.2-1.

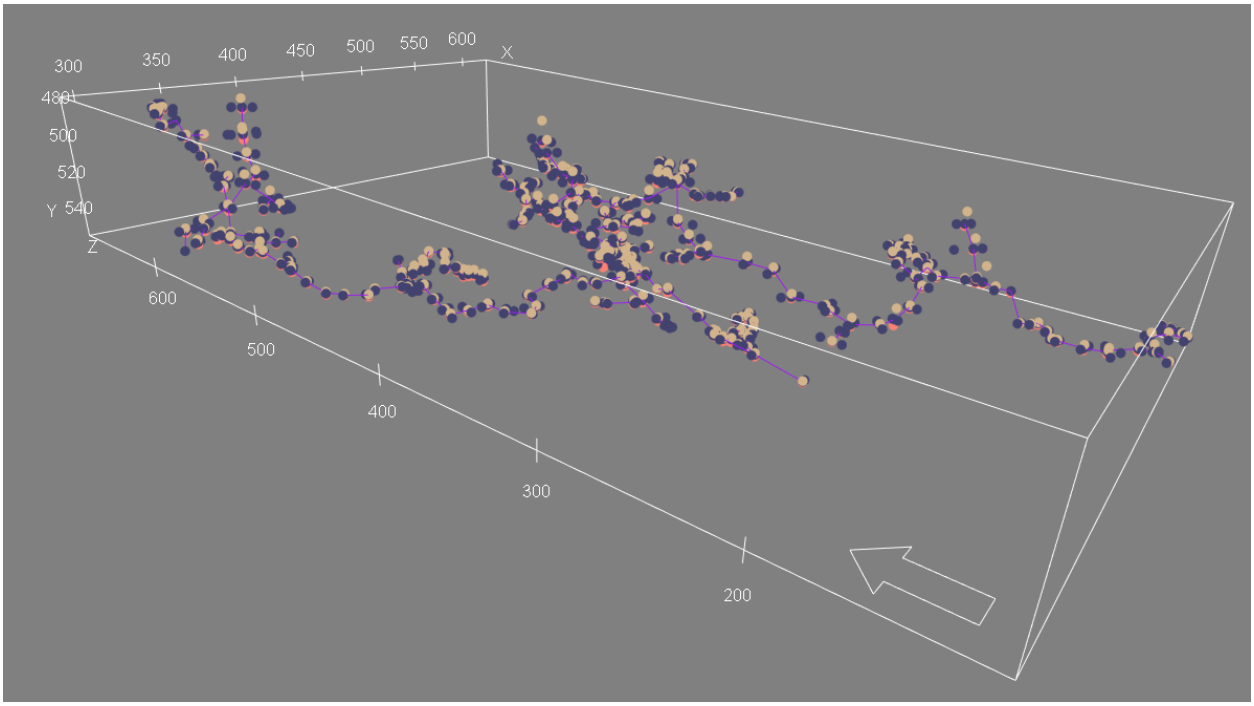


*Figure 2.1.2-1 SkeletonLines polygon based on input measure points (Unpublished mapping data, S.E. Lauritzen and R.Ø. Skoglund 2014, pers. comm., 7 April) from Setergrotta Cave.*

In order to provide a more realistic depth for later flow simulation, 1518 meters was added to the z-coordinates of the *SkeletonLines*, so that the depth range of the new *SkeletonLines2000* is 2000-2071 meters below mean sea level, therefore the name *SkeletonLines2000*.

*SkeletonLines2000* is based on a 3D point dataset of a multistoried cave passage. The starting point for further surface mapping was done by adapting the depth trend of the *SkeletonLines2000* to a boundary as described in the next chapter.

### 2.1.3 Stratigraphic framework and horizon mapping

Three horizons where defined to serve as input to the structural framework and later used to create a horizon model (Chapter 2.1.4).

*Cave_top*

*Cave*

*Cave_bottom*

All with *Type* as *Interpreted Horizon*. The *SkeletonLines2000* polygon was dropped on top of *SkeletonLines* under the horizon *Cave*. No faults are included in the model.

In order to map the *Cave_top* and *Cave_bottom horizons;* representing the top and bottom of the stratigraphic interval included in the model, *DepthPoints* are needed. To create these, the easiest way was to make a copy of the *SkeletonLines2000* from horizon *Cave* in *Clipboard*, right click and select *create boundary*. The resulting polygon (*BoundarySkeletonLines2000*) outlines the areal extent of the model. This polygon was slightly adjusted to avoid intersection points between the boundary and the *SkeletonLines2000*. This space is essential to build a grid with background in addition to the cave structure. See Figure 2.1.3-1.

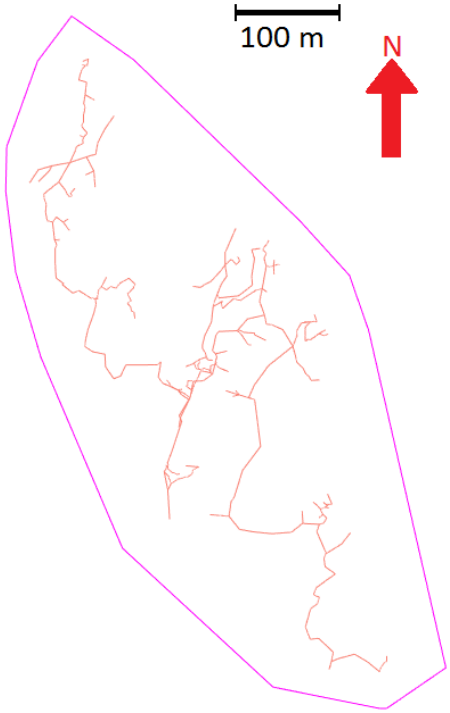


*Figure 2.1.3-1 Boundary (BoundarySkeletonLines2000) of cave model. Notice the adjustments made so that the boundary leaves some space for the SkeletonLines. This space is essential to build a grid with background in addition to the cave structure.*

Two copies of the boundary were made in *Clipboard*, *Boundary43up* and *Boundary27down*. These were adjusted respectively to 43 meters up and 27 meters down from *BoundarySkeletonLines2000*. As a result, all of the center points of the cave fell within the framework of these boundaries (see Figure 2.1.3-2). The boundaries were dragged and dropped onto *DepthPoints* for *Cave_top* and *Cave_bottom* under *Horizons*, and used as input for horizon mapping.

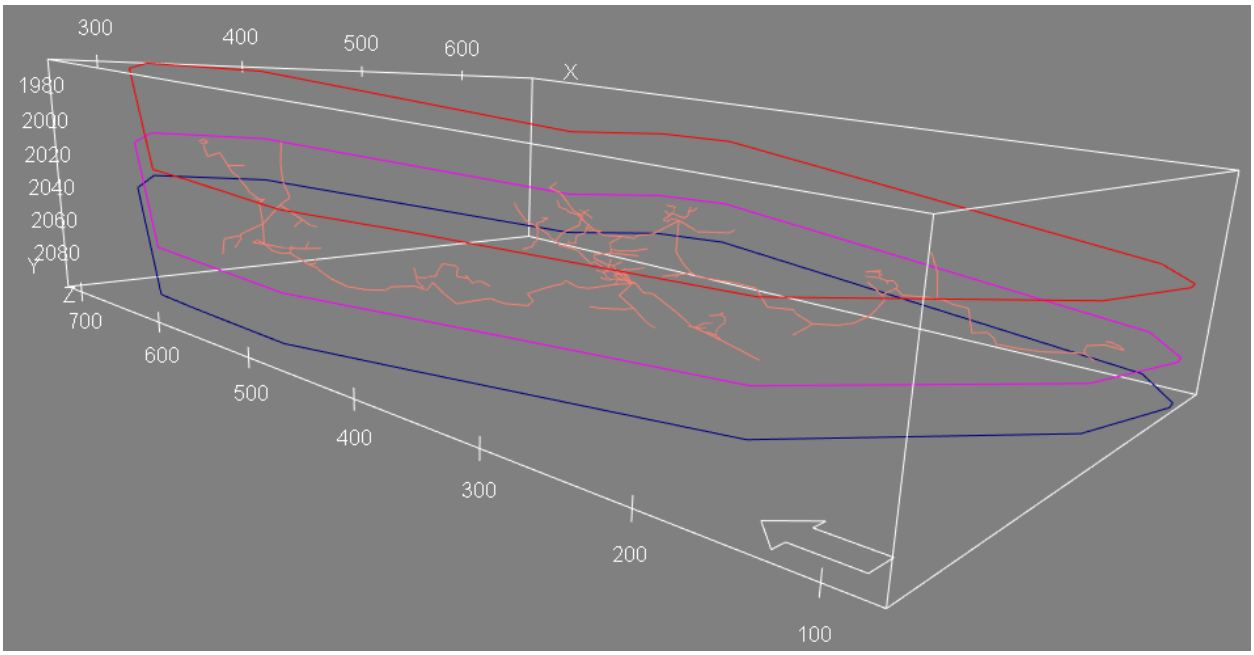


*Figure 2.1.3-2 Boundary43up (red), Boundary27down (blue) and BoundarySkeletonLines2000 (purple) which is based on the SkeletonLines2000 (orange).*

Horizon mapping was carried out for the *Cave_top* and *Cave_bottom*. The inputs were the *DepthPoints* created by the boundaries above, and the outputs were *DepthSurface*. See Figure 2.1.3-3 for the horizons. The default algorithm "Local B-spline" was used for mapping the horizons. It gives good results for all types of mapping, and does not require any user-defined settings (Roxar, 2013b). The polygons were used to constrain the areal extent of the horizons.

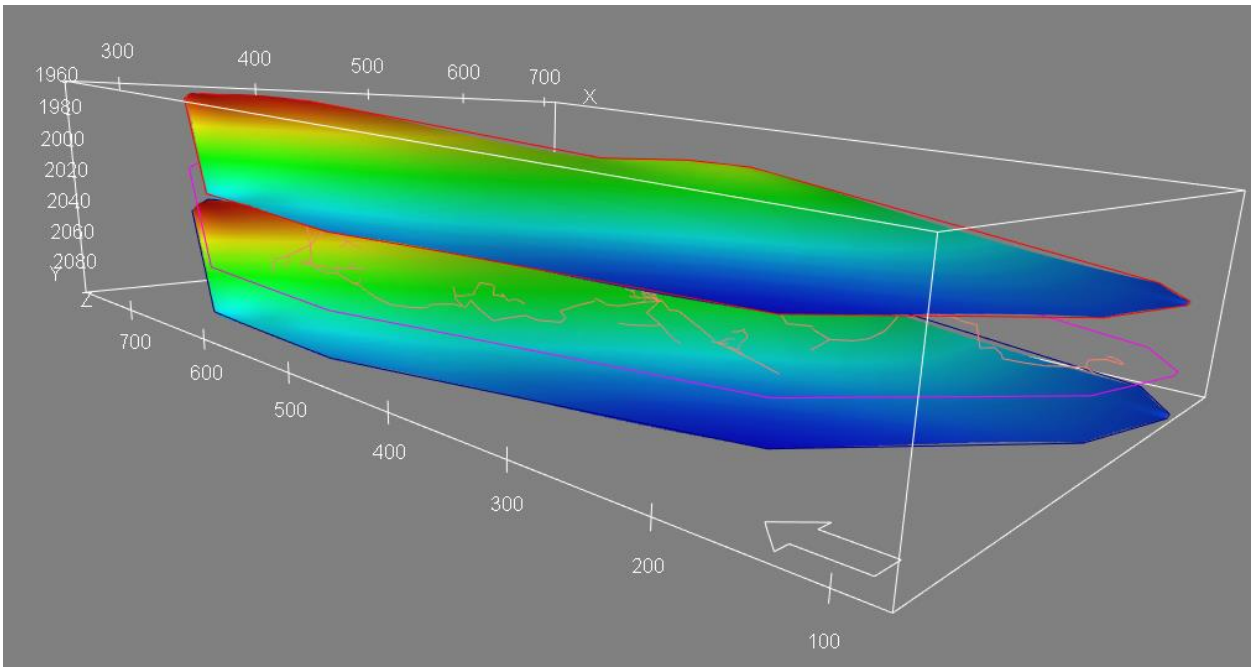


*Figure 2.1.3-3 Horizons Cave_top and Cave_bottom with Boundary43up (red), Boundary27down (blue) and BoundarySkeletonLines2000 (purple) which is based on the SkeletonLines2000 (orange).*

These two horizons define the top and base of the reservoir model and serve as base for the structural modeling, horizon modeling and subsequent grid-building.

### 2.1.4 Structural model and horizon modeling

To create a grid, it is necessary to have a horizon model. A structural model *Cave* was made, and a model box was defined based on the spatial range from object *BoundarySkeletonLines2000*, with adjusted XYZ-length. A horizon model *Cave2000* was made based on the structural model and the horizons *Cave_top* and *Cave_bottom* from Chapter 2.1.3.

*Table 2.1.4-1 Box definition based on the range from object BoundarySkeletonLines2000, with adjusted XYZ-length*

| | Centre | Length |
|---|---|---|
| X | 475.90 | 500.00 |
| Y | 394.46 | 750.00 |
| Z | 2036.75 | 170.00 |

Selected horizons were:

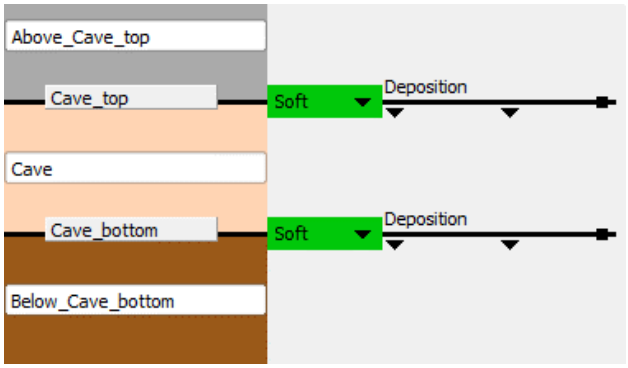


*Figure 2.1.4-1 Horizons in horizon model Cave2000. Compare to the structure in Figure 2.1.4-2 and Figure 2.1.4-3.*

The input data types were the *DepthSurfaces* described above. The resolution and increment in XY-direction was set to 1 meter. The outputs from the structural modeling are the horizons *Cave_top* and *Cave_bottom* in Figure 2.1.4-2 and the horizon model in Figure 2.1.4-3.

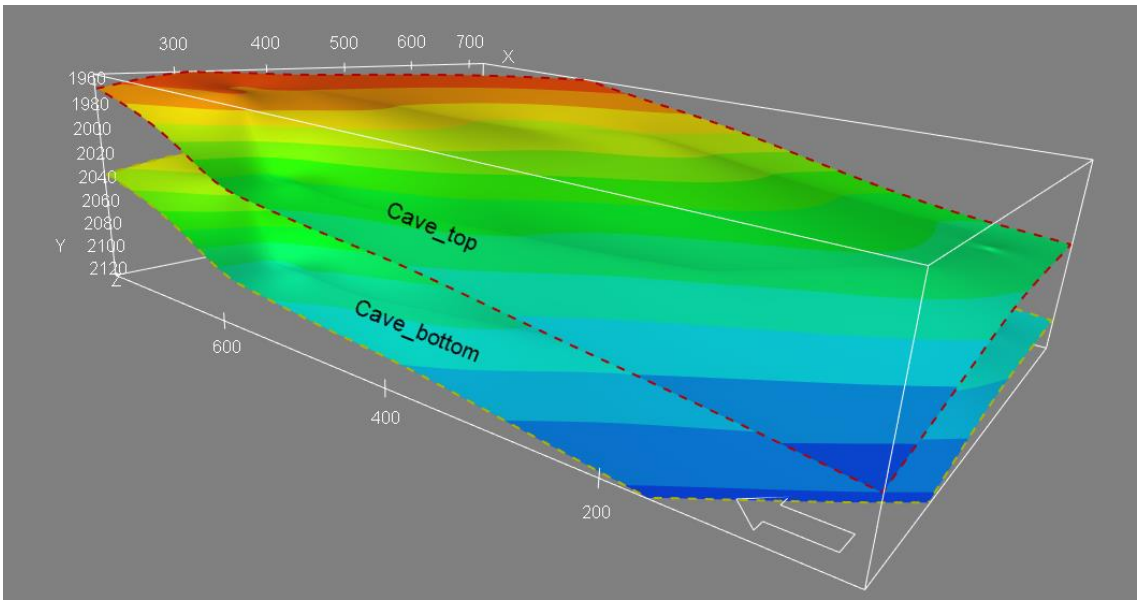


*Figure 2.1.4-2 Horizons Cave_top and Cave_bottom*

The body of rock "Cave" in blue in Figure 2.1.4-3 is used to create a reservoir grid model.

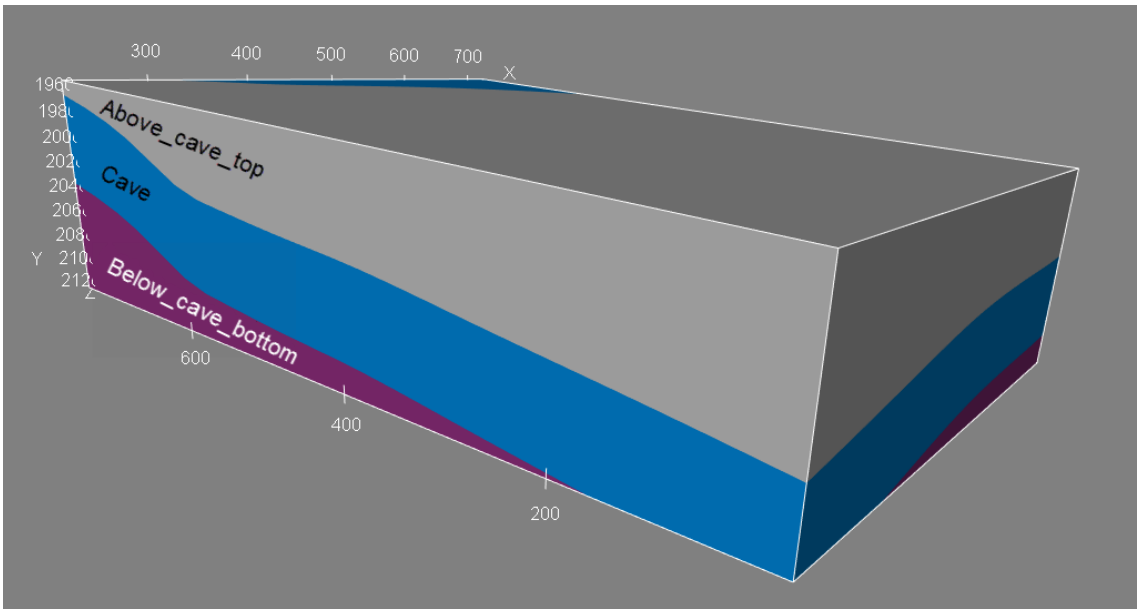


*Figure 2.1.4-3 Horizon model Cave2000, based on horizons Cave_top and Cave_bottom. Note the blue section "Cave". This is the body of rock between these two horizons delimiting the spatial extent of the reservoir grid.*

### 2.1.5 Grid models

A grid model called *Grid2000_2_10_high* (see Appendix 7.1.1 for explanation of the Grid model names) was created, with horizon model *Cave2000* as input. Under *2D layout*, the grid was clipped using the *BoundarySkeletonLines2000* polygon, to save number of grid cells (see Figure 2.1.5-1). The grid is rotated by 15 degrees to adapt it to the structural trend and lineaments evident from the cave structure (see Chapter 2.1.8). Then *Auto-calculate best fit* option was selected, and grid dimensions were set to an increment of 2 meters in x- and y-direction. Under *Zone layout* number of cells was set to be 35. This because the grid is built between the *Cave_top* and *Cave_bottom* surfaces which were adjusted respectively to 43 meters up and 27 meters down from the *BoundarySkeletonLines2000* (see Chapter 2.1.3). This equals a total thickness of 70 meters, and to get an increment of 2 meters in z-direction, number of cells is set to be $70/2 = 35$ cells. The grid consists of 1323735 grid cells with cell dimensions $2\text{m} \times 2\text{m} \times 2\text{m}$. Total reservoir volume is $1323735 \times 2 \times 2 \times 2\ \text{m}^3 \approx 10.6\ \text{MSm}^3$.

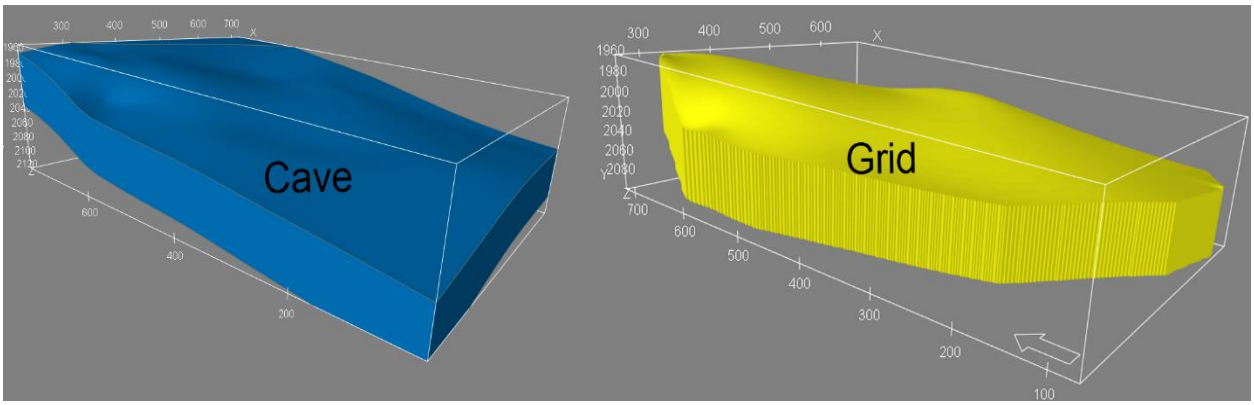


*Figure 2.1.5-1 Left picture shows Cave in horizon model Cave2000. This volume defines the region to be gridded. To the right is the resulting grid model Grid2000_2_10_high that is clipped outside the polygon BoundarySkeletonLines2000 to save number of cells. Grid2000_2_10_high has grid diameter of 2 meters.*

### 2.1.6 Geometric modeling

The *Geometric modeling* functionality in RMS was used to implement and visualize the cave passages inside the grid. This functionality allows the definition and calculation of distance to a given point, well or surface. It was not possible to use the *SkeletonLines* as an input object directly. Therefore, points based on the *SkeletonLines2000* were made by refining the segments between the initial center points. This was carried out by selecting all lines in the 3D window and clicking on *refine selected segments* until the points were as close as needed to not lose any information or get gaps while gridding. After refining the lines/polygon, *empty points* were created in the *Clipboard* and the refined *SkeletonLines2000* were dragged onto these. The *RefinedPoints_SkeletonLines2000*, as they were named, could now be used as object in geometric modeling. A geometric model, *Geometric_5* was generated. When selecting calculation type *Distance to objects*, the cell values increase for each meter from the centerline. See Figure 2.1.6-1 below.

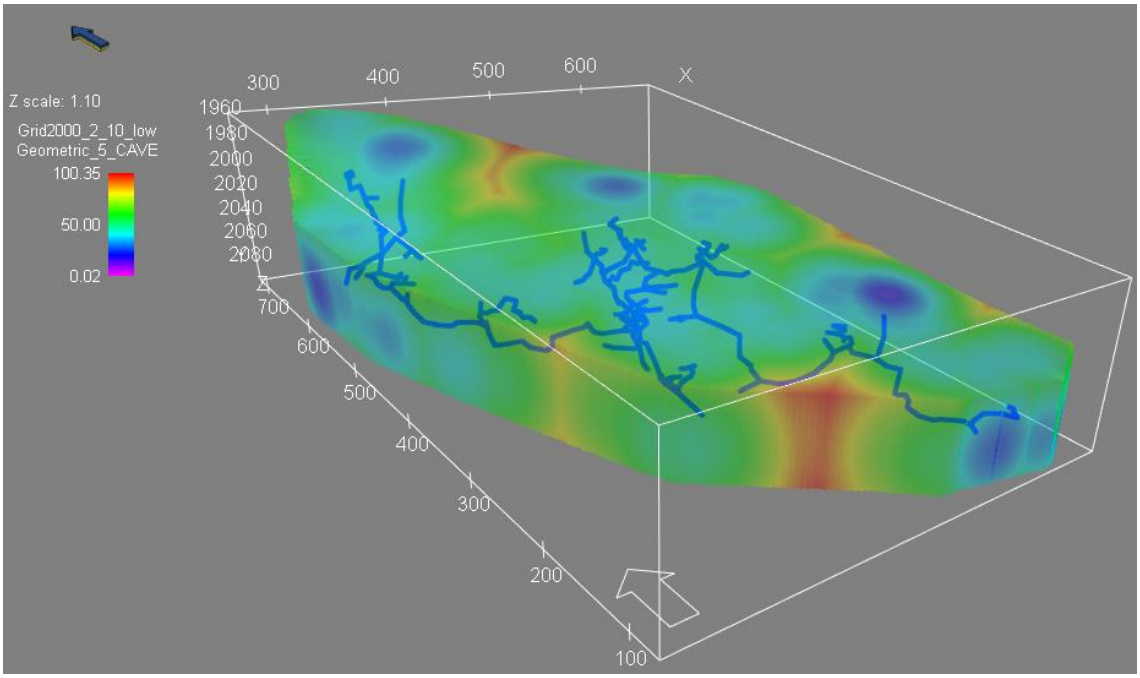


*Figure 2.1.6-1 Geometric model (Geometric_5) measuring distance from the centerline of the cave (RefinedPoints_SkeletonLines2000). Blue is near, and red far away from the centerline.*

When right clicking on *Grid* and selecting *Filter*, it is possible to activate the geometric parameter and filtering the parameter at any given distance away from the object (*RefinedPoints_SkeletonLines2000*). When setting the filter at 5 meters for *Geometric_5*, the cave body stands out as a completely gridded cave with a radius 5 meters distant from the original skeleton lines defining the cave (see Figure 2.1.6-2). The resulting "cave" in the model has an unrealistic homogenous diameter, but this can be refined by splitting the skeleton lines into segment and performing geometrical modeling on these separately.

Attempts were made using *intrusions* in RMS to map and grid the cave, but unfortunately it was not possible to grid the intrusions. The version of RMS used in the present study did also not allow property modeling for bodies defined as intrusions. If intrusions could be gridded, the resulting reservoir model would have had irregular cave width based on distance to wall-, ceiling- and floor points, and therefore be a more realistic cave system.

The best way to visualize the cave geometry with the available tools is to create a parameter that differentiates between "cave" and "no cave". A discrete parameter, *Cave_nocave*, with cell values 0 is created. When the filter from above (Geometric_5 with radius 5 meter) is active, these values can be set to value 1 by using the Calculator (*Grid - Tasks - Parameter utilities - Calculator*) in RMS. Everything within the 5 meter radius from the RefinedPoints_SkeletonLines2000 in the parameter *Cave_nocave* was set to *Cave* (blue), while the rest was set to *No_cave* (red). See Figure 2.1.6-2, Figure 2.1.6-3, and Figure 2.1.6-4 below.

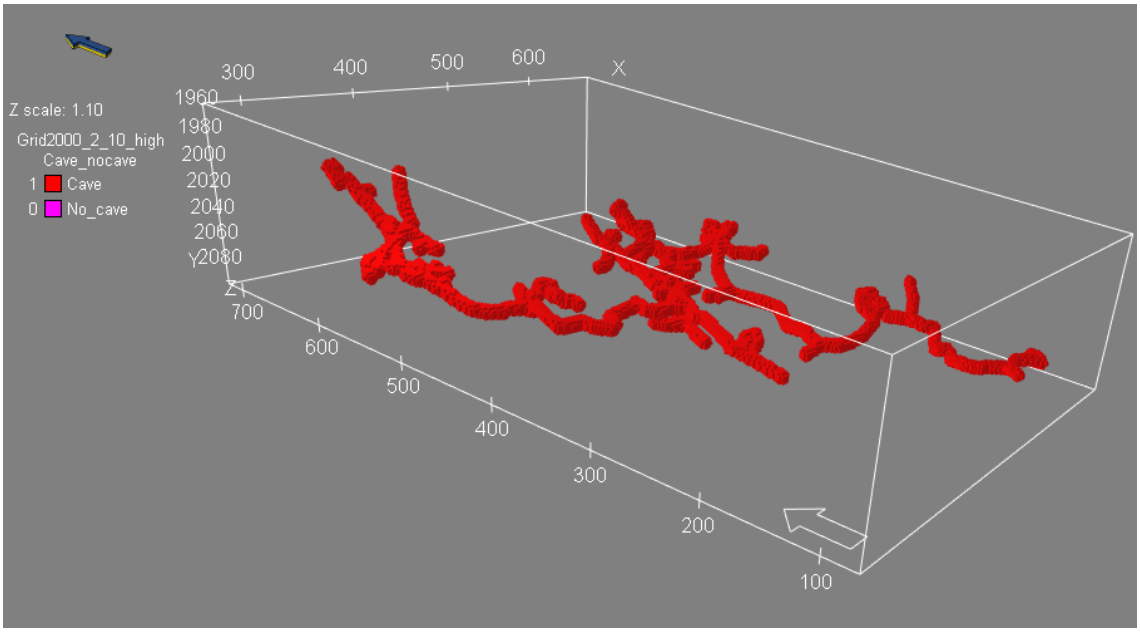


*Figure 2.1.6-2 Gridded cave (red) with a total of 26440 cells (2x2x2meters)*

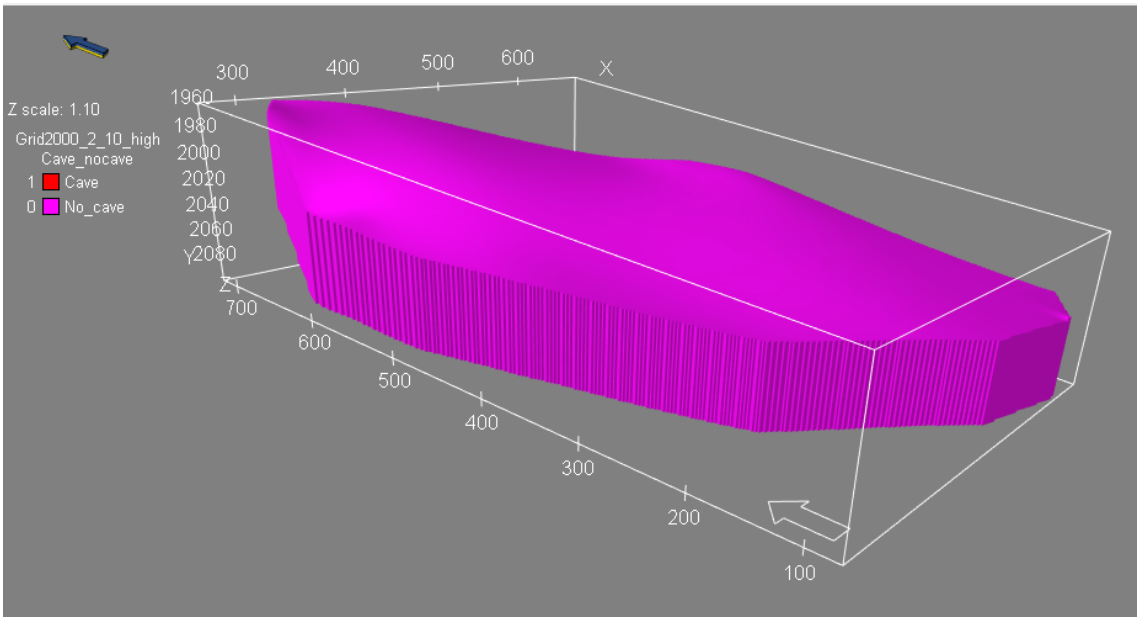


*Figure 2.1.6-3 Gridded no_cave (purple) with cave (red) with a total of 1323735 cells. No_cave has 1297295 cells.*

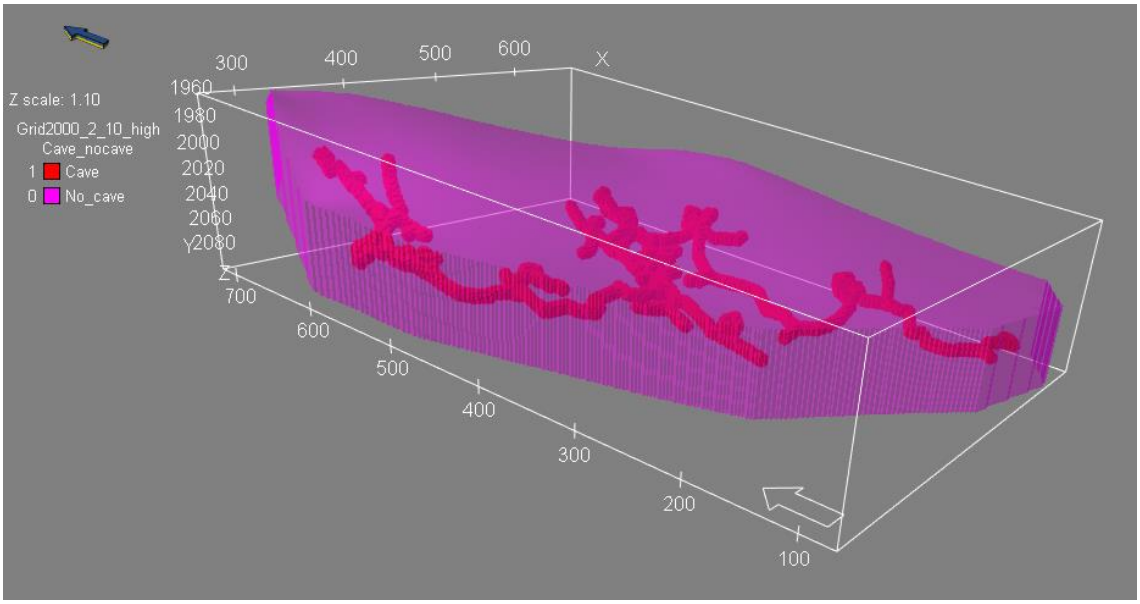


*Figure 2.1.6-4 Gridded no_cave (purple) with cave (red) inside.*

As outlined in Chapter 1.3.4, there is a link between the radius of the collapsed cave, the radius of the initial cave and average porosity of the collapsed cave. As the collapse progresses upwards and to each side of the cave, the initial floor stays in the same position. Figure 1.3.4-2 illustrates that the centerline of the cave has to move $R_2$-$R_1$ in Z-direction upwards. In RMS, this is captured by *Scalar operations* of the *RefinedPoints_SkeletonLines2000*. For later use, an additional set of seven geometric models were made based on different centerlines. These are elevated 3, 1, -1, -3, -5, -7, and -9 meters relative to the *RefinedPoints_SkeletonLines2000* and the resulting geometric model *Geometric_5* (see Table 2.1.6-1 and Figure 2.1.6-5).

Figure 2.1.6-5 presents a method of capturing the decreasing porosity trend (see Figure 1.3.4-2 and Figure 2.1.7-3) in collapsed cave systems in RMS. Refined points are used as center lines for geometric modeling. Each line has an own geometric model, and by using *Filter* and *Calculator* in RMS, petrophysical properties can be assigned to the circle sectors.

*Table 2.1.6-1 Additional Geometric Models for later calculation*

| Elevated refined points as input for geometric modeling | Geometric model | Elevation from original *RefinedPoints_SkeletonLines2000* |
|---|---|---|
| *RefinedPoints_SkeletonLines2000_+3* | *Geometric_2* | 3 meters |
| *RefinedPoints_SkeletonLines2000_+1* | *Geometric_4* | 1 meter |
| *RefinedPoints_SkeletonLines2000_-1* | *Geometric_6* | -1 meter |
| *RefinedPoints_SkeletonLines2000_-3* | *Geometric_8* | -3 meters |
| *RefinedPoints_SkeletonLines2000_-5* | *Geometric_10* | -5 meters |
| *RefinedPoints_SkeletonLines2000_-7* | *Geometric_12* | -7 meters |
| *RefinedPoints_SkeletonLines2000_-9* | *Geometric_14* | -9 meters |

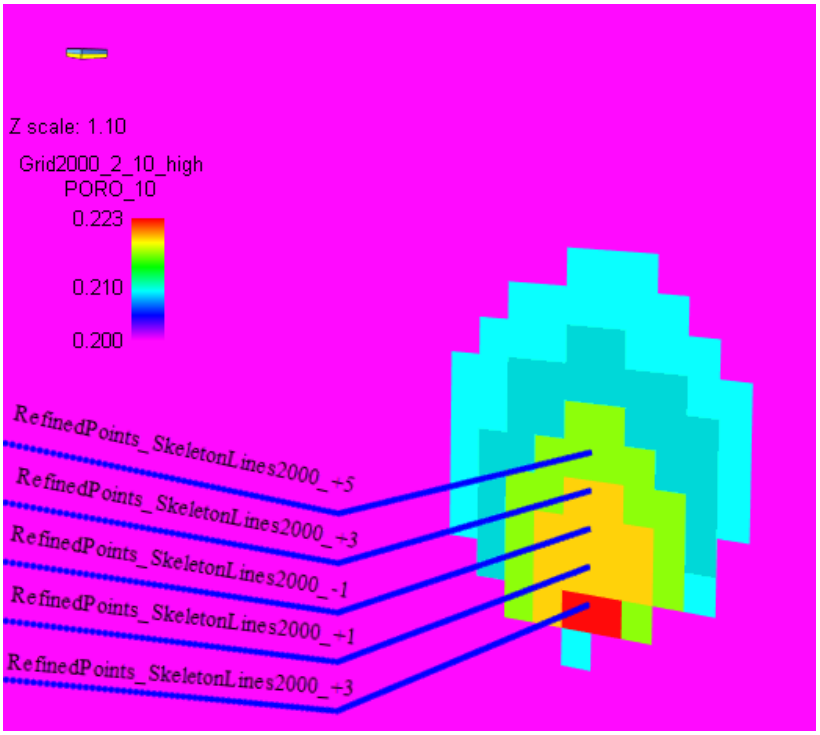


*Figure 2.1.6-5 This figure presents the method of capturing the decreasing porosity trend (see* **Figure 1.3.4-2** *and Figure 2.1.7-3) in collapsed cave systems in RMS. Refined points (see Appendix 7.1.3 for explanation) are used as center lines for geometric modeling. Each line has an own geometric model, and by using Filter and Calculator in RMS, petrophysical properties can be assigned to the circle sectors. Here porosity for Grid2000_2_10_high is presented.*

### 2.1.7 Porosity and permeability in the reservoir model

The determination of porosity and permeability values for use in a paleokarst reservoir model is not straight forward. First of all, porosity values vary both between and within carbonate systems as a result of their complexity (see Chapters 1.1.1 and 1.2.8). As mentioned in Chapter 1.2.8, Brown (1997), Goldhammer (1997), and Schmoker and Halley (1982) describe different carbonate systems and their porosity values plotted against depth. From these studies, carbonate systems like grainstones seem to have a porosity varying between 5 and 20 % on a typical hydrocarbon reservoir depth of 2000 meters (below mean sea level). This will be treated as minimum and maximum case for the background porosity.

The porosity inside of the collapsed cave is dependent on the resulting radius of the collapsed cave and sediment fill. As described in Chapter 1.3.4, the end radius after collapse ($R_2$) for the three cases in this thesis will be 10, 12, and 14 meters. These radii result in different average porosities for the resulting collapsed cave. See  below.

*Table 2.1.7-1 Radius after collapse (R2) for the three cases in this thesis will be 10, 12, and 14 meters. These are the green values from Table 1.3.4-1.*

| $R_2$ | Ø % |
|---|---|
| 10.0 | 25.00 |
| 12.0 | 17.36 |
| 14.0 | 12.76 |

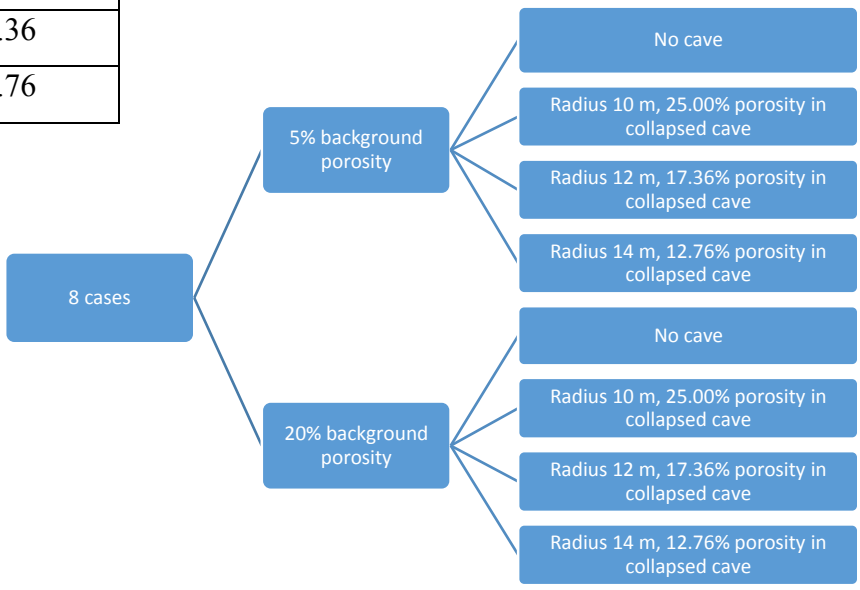


*Figure 2.1.7-1 This figure describes the eight cases for geometry and porosity/permeability in this thesis.*

As Figure 1.3.4-2 describes the geometry of the cave after collapse, Figure 2.1.7-3 shows how to model such a feature in RMS. It shows a propagating collapse of the original cave structure, with three end-cases based on the radius of the collapsed cave. The centerline has to be moved upwards as Figure 1.3.4-2 and Table 2.1.6-1 shows, to keep the initial cave floor at a constant elevation. Figure 2.1.7-2 illustrates a cave opening, and a potential cave collapse halo of cave roof and walls.

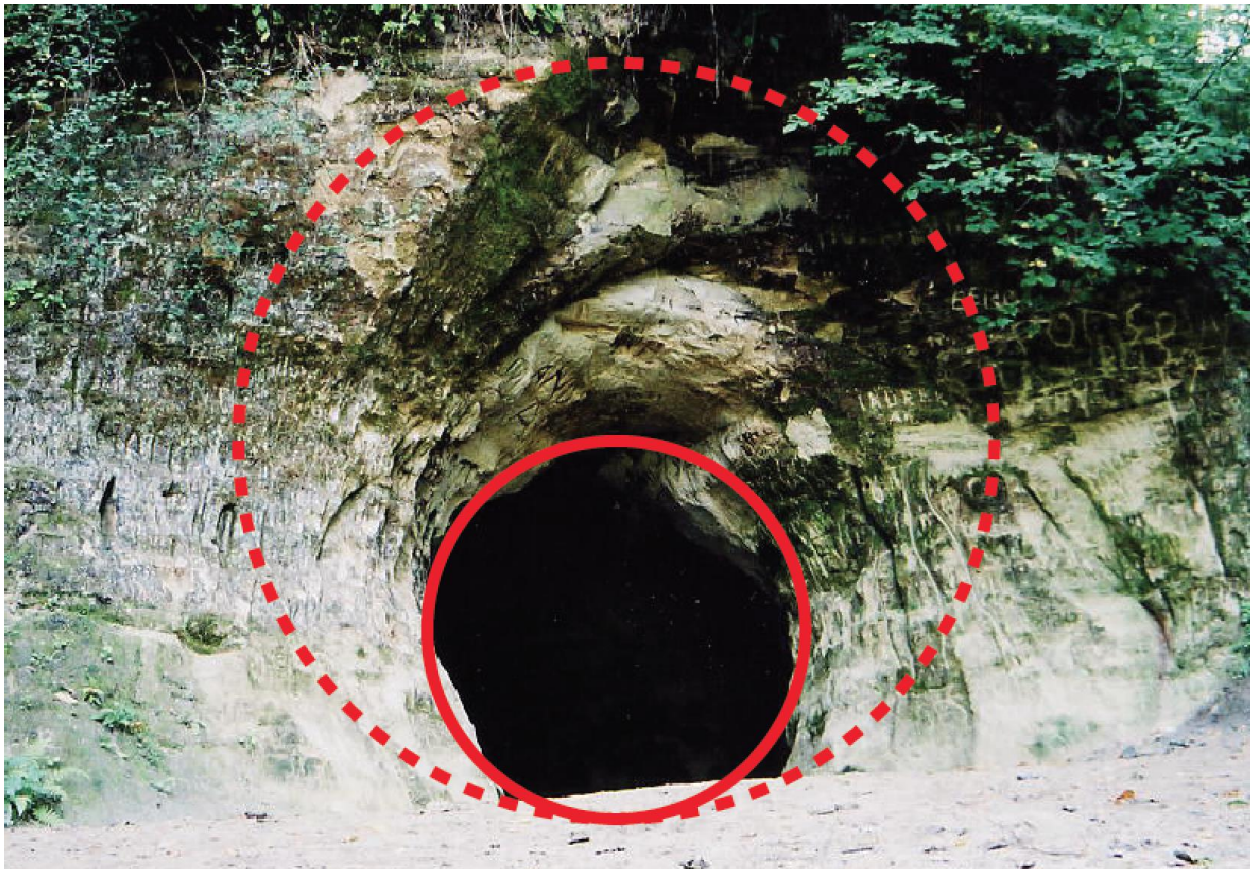

*Figure 2.1.7-2 This picture illustrates a cave opening, and a potential cave collapse halo of cave roof and walls. Compare to Figure 2.1.7-3.*

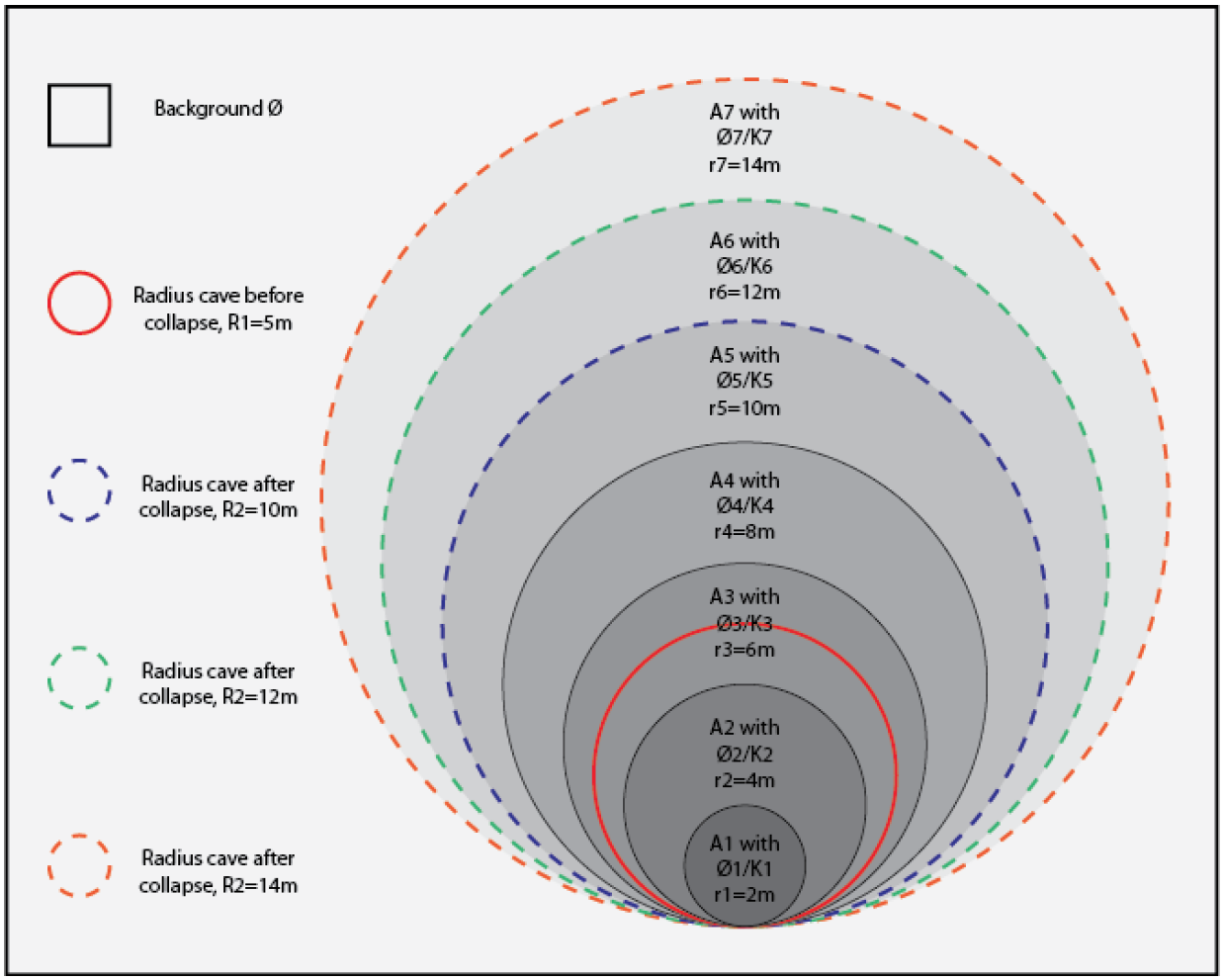


*Figure 2.1.7-3 Model set up of propagating collapse of cave in RMS. **Øn** = porosity and **Kn** = permeability for each segment **An**. **rn** represents the radius for each segment **An**. **$R_2$** and **$R_1$** are the radiuses of the collapsed cave and cave before collapse respectively. Is should be pointed out that the circular shape of the collapse is an approximation – the shape of the collapse will depend on the mechanical properties of the host rock, which in turn is related to lithology, bedding and the presence of faults and fractures.*

To calculate porosity in each section of the collapsed cave, the formulas below are used to maintain the average porosity of the collapsed cave presented in Table 2.1.7-1. Here a trial and error approach was used to choose reasonable porosity values for each section, with porosity values decreasing outwards (see Chapter 1.3.4). For porosity values in each section for the three radii cases, see 2nd column in Table 2.1.7-3, Table 2.1.7-4, and Table 2.1.7-5.

The formulae below ensure that the average porosity in the collapsed cave remains constant as in Table 2.1.7-1. A complete list of symbols is presented in Appendix 7.1.4.

$$A_n \times \emptyset_n + \cdots + A_1 \times \emptyset_1 = A_t \times \emptyset_t \quad (2)$$

$$\pi(r_n{}^2 - r_{n-1}{}^2) \times \emptyset_n + \cdots + \pi(r_2{}^2 - r_1{}^2) \times \emptyset_2 + \pi r_1{}^2 \times \emptyset_1 = \pi r_t{}^2 \times \emptyset_t \quad (3)$$

$$(r_n{}^2 - r_{n-1}{}^2) \times \emptyset_n + \cdots + (r_2{}^2 - r_1{}^2) \times \emptyset_2 + r_1{}^2 \times \emptyset_1 = r_t{}^2 \times \emptyset_t = \underline{2500} \quad (4)$$

To calculate permeability for the host rock, in this case a grainstone a with porosity of 5 or 20 %, the chart "Intercrystalline macroporosity" from Lønøy (2006) is used.

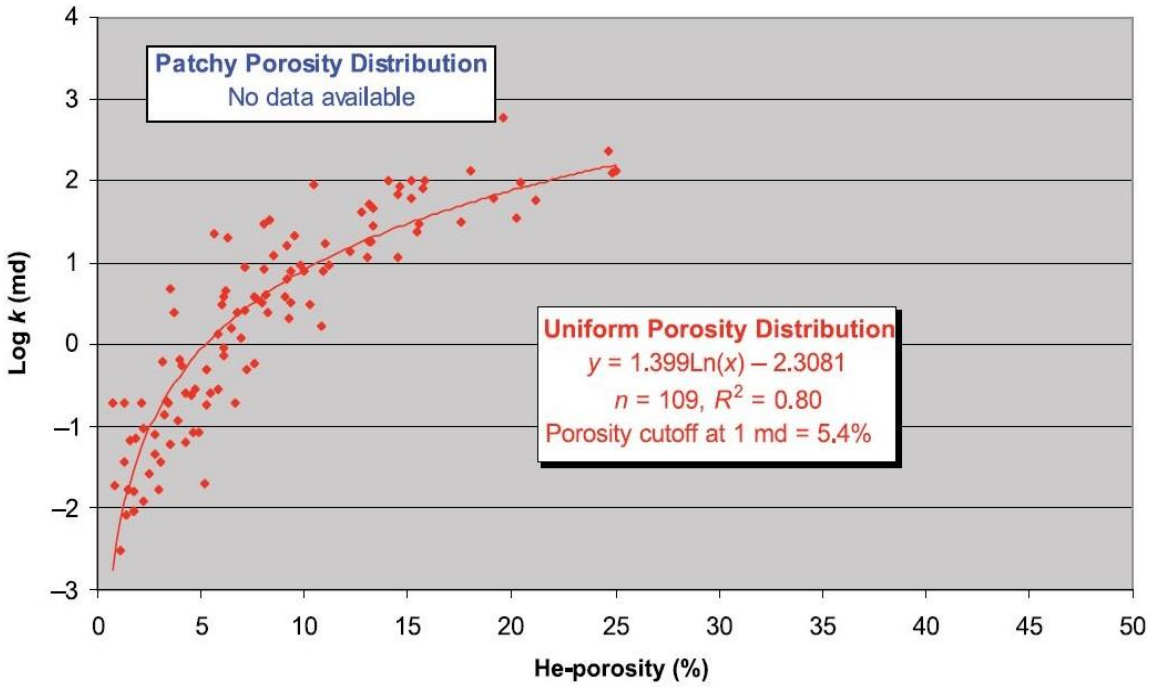


*Figure 2.1.7-4 (Lønøy, 2006) Intercrystalline Macroporosity. Macropores are most common in moderately to wellsorted, high-energy grainstones.*

The formula gives permeability from porosity. A complete list of symbols is presented in Appendix 7.1.4.

$$log(K) = 1.399 \times Ln(\emptyset) - 2.3081 \quad (5)$$

To see the effect of differences in the background grainstone, the pore spaces in the conceptual collapsed cave model are filled with sandstone with constant porosity and permeability values. Averaging the porosity and permeability inside of the collapsed cave is needed because it is filled with both clasts from background and sandstone fill.

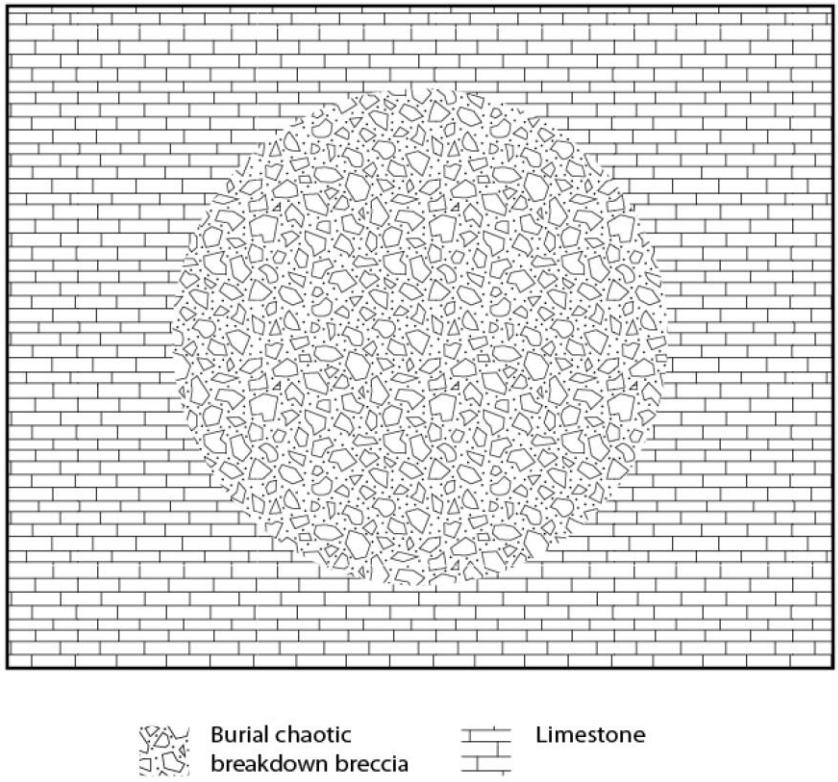


*Figure 2.1.7-5 The clasts in the chaotic breakdown breccia consists of both background limestone, and sandstone sediment fill.*

Uniform porosity distribution from Figure 2.1.7-4 (Lønøy, 2006) in grainstone, gives:

*Table 2.1.7-2 Input values high- and low case*

| | HIGH CASE | LOW CASE |
|---|---|---|
| Porosity (Ø) in background (BG) [%] | 20 | 5 |
| Permeability (*K*) in background (BG) [mD] | 76.37 | 0.88 |
| Porosity (Ø) in sandstone fill (Fill) [%] | 25 | 25 |
| Permeability (*K*) in sandstone fill (Fill) [mD] | 2000 | 2000 |

To average the porosity inside of the collapsed cave, arithmetic averaging is used. (Roxar, 2013a). A complete list of symbols is presented in Appendix 7.1.4.

$$P_A = \left(\frac{\sum_n W_n P_n}{\sum_n W_n}\right) \quad (6)$$

Example:
Values from Table 2.1.7-2 (high case) and Table 2.1.7-3 (Area A1, high case, porosity).

$$\underline{\text{Porosity } (\emptyset)} = \left(\frac{46\times 25\ \% + 54\times 20\ \%}{46+54}\right) = \frac{2230\ \%}{100} = \underline{22.3\ \%} \quad (7)$$

Because of the chaotic nature of the system, geometric averaging is used for permeability. This yields a value between arithmetic and harmonic average. (Roxar, 2013a). A complete list of symbols is presented in Appendix 7.1.4.

$$P_G = \exp\left(\frac{\sum_n W_n \mathrm{Ln} P_n}{\sum_n W_n}\right) \quad (8)$$

Example:
Values from Table 2.1.7-2 (high case) and Table 2.1.7-3 (Area A1, high case, permeability).

$$\underline{\text{Permeability } (K)} = \exp\left(\frac{46\times \mathrm{Ln}(2000\ \text{mD}) + 54\times \mathrm{Ln}(76.37\ \text{mD})}{46+54}\right) = \mathrm{e}^{5.83764} = \underline{342.97\ \text{mD}} \quad (9)$$

See Table 2.1.7-3, Table 2.1.7-4, and Table 2.1.7-5 for complete calculation of porosity and permeability values for each area in the six collapsed cave cases.

*Table 2.1.7-3 Radius collapsed cave ($R_2$) = 10 → $R_2/R_1$ = 2.0 → $Ø_t$ = 25.0 %. See Table 2.1.7-2 for explanations of BG and Fill*

| | | | HIGH CASE | | LOW CASE | |
|---|---|---|---|---|---|---|
| Area | Ø Fill [%] | Ø BG [%] | Tot. Ø [%] | Tot. Perm [mD] | Tot. Ø [%] | Tot. Perm [mD] |
| A1 | 46.00 | 54.00 | 22.30 | 342.97 | 14.20 | 30.76 |
| A2 | 39.00 | 61.00 | 21.95 | 272.89 | 12.80 | 17.90 |
| A3 | 32.00 | 68.00 | 21.60 | 217.13 | 11.40 | 10.42 |
| A4 | 20.00 | 80.00 | 21.00 | 146.74 | 9.00 | 4.12 |
| A5 | 18.00 | 82.00 | 20.90 | 137.46 | 8.60 | 3.53 |
| BG | 0.00 | 100.00 | 20.00 | 76.37 | 5.00 | 0.88 |

*Table 2.1.7-4 Radius collapsed cave ($R_2$) = 12 → $R_2/R_1$ = 2.4 → $Ø_t$ = 17.4 %. See Table 2.1.7-2 for explanations of BG and Fill*

| | | | HIGH CASE | | LOW CASE | |
|---|---|---|---|---|---|---|
| Area | Ø Fill [%] | Ø BG [%] | Tot. Ø [%] | Tot. Perm [mD] | Tot. Ø [%] | Tot. Perm [mD] |
| A1 | 43.00 | 57.00 | 22.15 | 310.97 | 13.60 | 24.39 |
| A2 | 38.00 | 62.00 | 21.90 | 264.12 | 12.60 | 16.57 |
| A3 | 31.00 | 69.00 | 21.55 | 210.16 | 11.20 | 9.65 |
| A4 | 20.00 | 80.00 | 21.00 | 146.74 | 9.00 | 4.12 |
| A5 | 18.00 | 82.00 | 20.90 | 137.46 | 8.60 | 3.53 |
| A6 | 1.00 | 99.00 | 20.05 | 78.91 | 5.20 | 0.95 |
| BG | 0.00 | 100.00 | 20.00 | 76.37 | 5.00 | 0.88 |

*Table 2.1.7-5 Radius collapsed cave ($R_2$) = 14 → $R_2/R_1$ = 2.8 → $Ø_t$ = 12.8 %. See Table 2.1.7-2 for explanations of BG and Fill*

| | | | HIGH CASE | | LOW CASE | |
|---|---|---|---|---|---|---|
| Area | Ø Fill [%] | Ø BG [%] | Tot. Ø [%] | Tot. Perm [mD] | Tot. Ø [%] | Tot. Perm [mD] |
| A1 | 41.00 | 59.00 | 22.05 | 291.31 | 13.20 | 20.90 |
| A2 | 36.00 | 64.00 | 21.80 | 247.43 | 12.20 | 14.20 |
| A3 | 30.00 | 70.00 | 21.50 | 203.40 | 11.00 | 8.93 |
| A4 | 20.00 | 80.00 | 21.00 | 146.74 | 9.00 | 4.12 |
| A5 | 18.00 | 82.00 | 20.90 | 137.46 | 8.60 | 3.53 |
| A6 | 1.00 | 99.00 | 20.05 | 78.91 | 5.20 | 0.95 |
| A7 | 1.00 | 99.00 | 20.05 | 78.91 | 5.20 | 0.95 |
| BG | 0.00 | 100.00 | 20.00 | 76.37 | 5.00 | 0.88 |

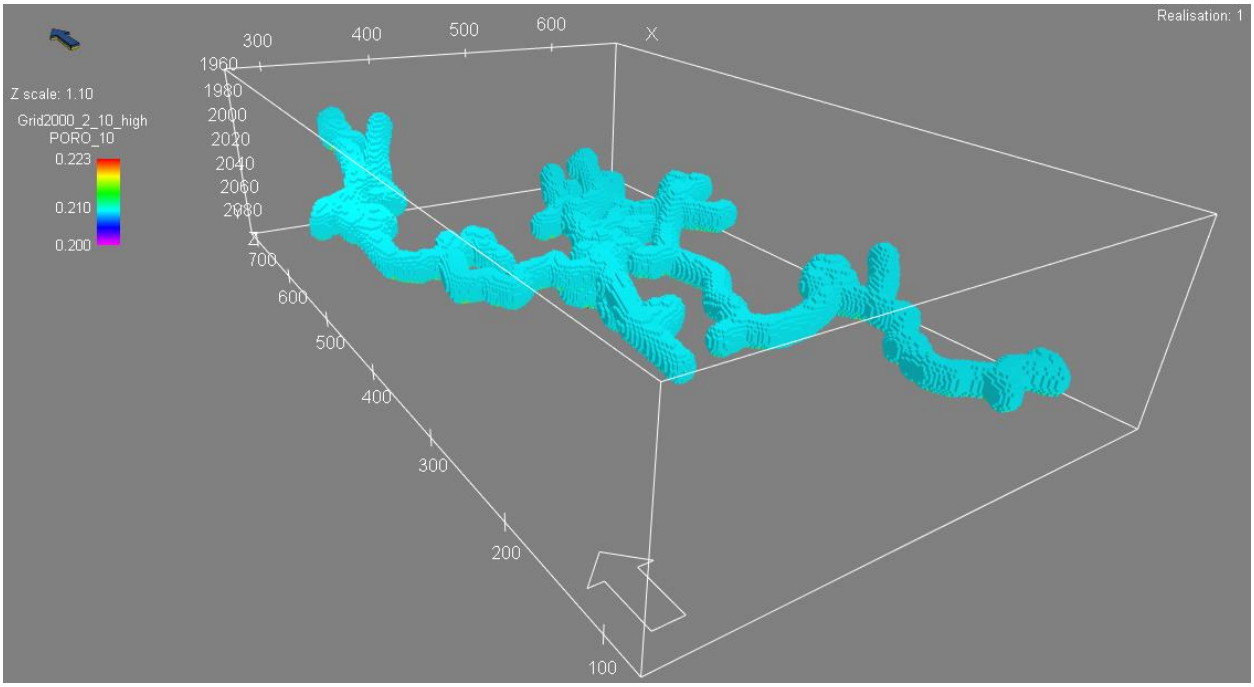


*Figure 2.1.7-6 Cave after collapse, $R_2$ = 10 meters, high case porosity distribution.*

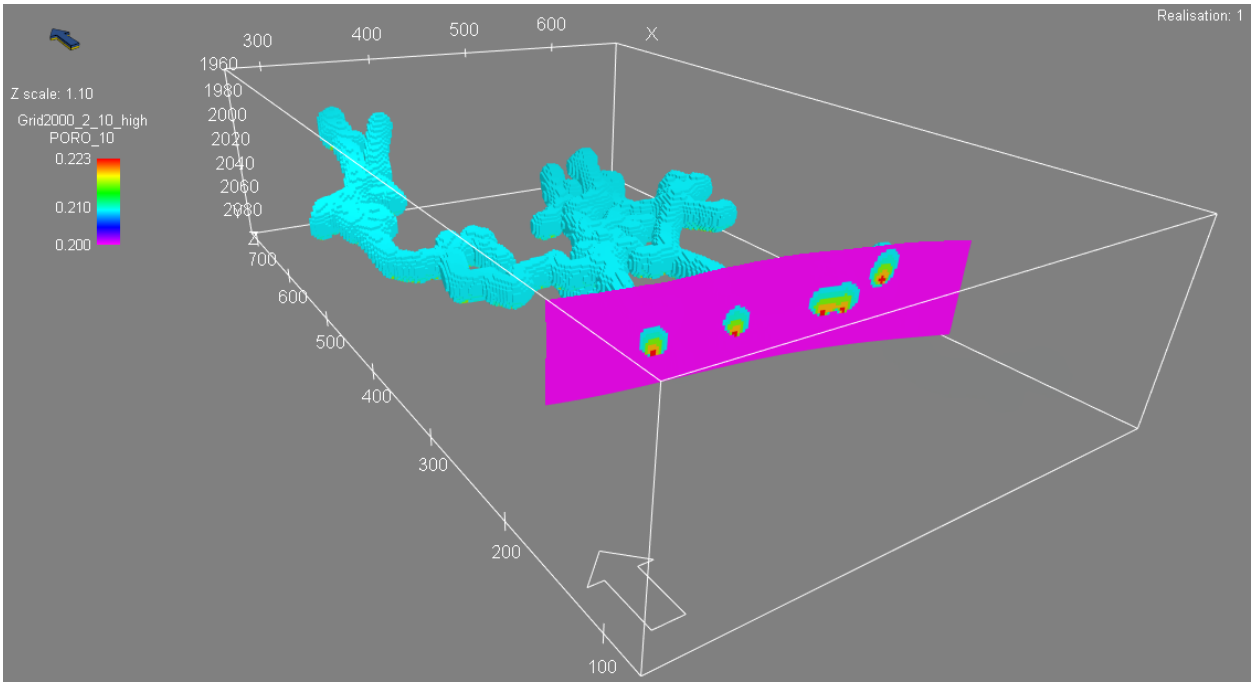


*Figure 2.1.7-7 Cave after collapse, $R_2$ = 10 meters, high case porosity distribution. Cross section of the hole reservoir model shows the decreasing porosity from highest at the base of the cave.*

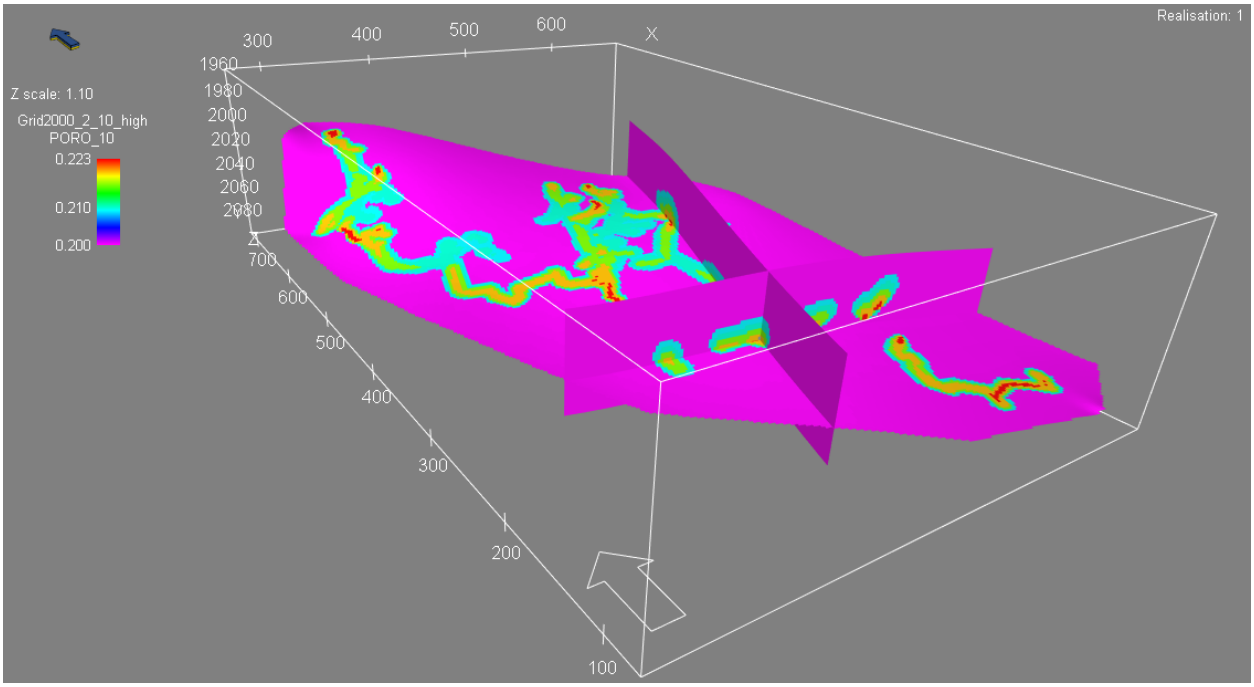


*Figure 2.1.7-8 Cross section of high case porosity distribution with $R_2$ = 10 meters. Notice the decreasing porosity outwards.*

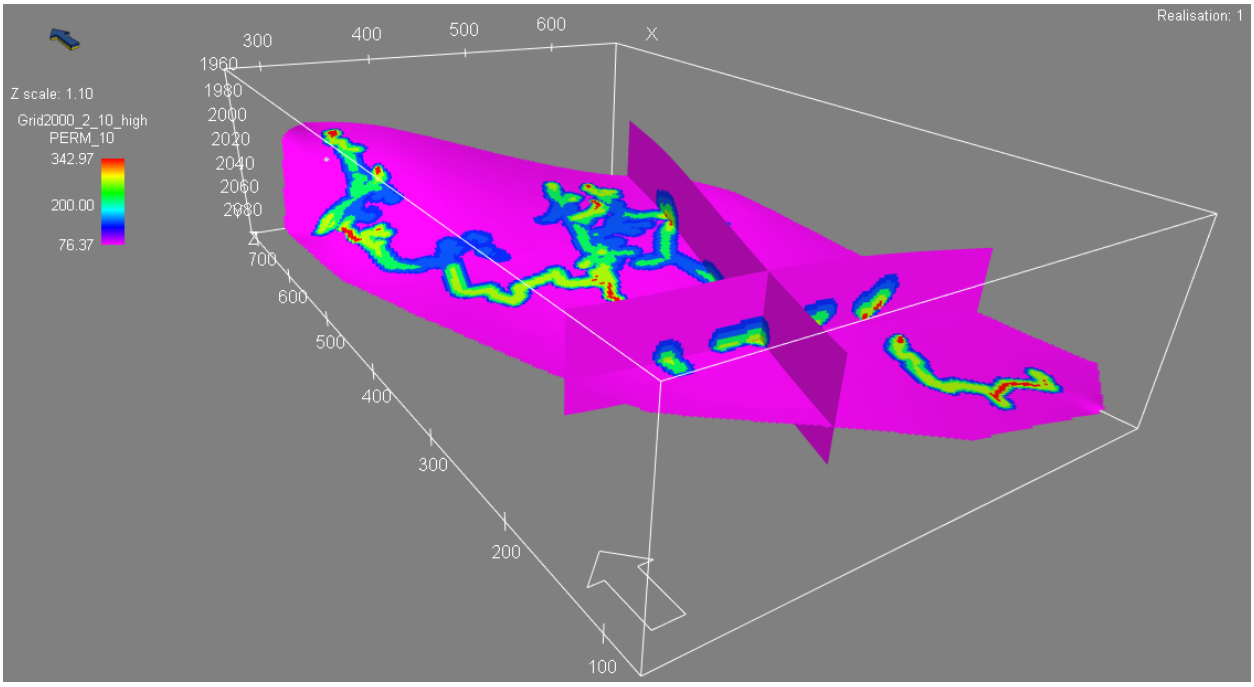


*Figure 2.1.7-9 Cross section of high case permeability distribution with $R_2$ = 10 meters. Notice the decreasing permeability outwards.*

### 2.1.8 Fracture model

To create a realistic reservoir model of a karst system, fractures have to be accounted for. Large caves develop in and expand pre-existing fractures (see section 1.3.1). Figure 2.1.8-1 below shows an image of the cave geometry as seen from above and a rose diagram presenting the main direction of the cave passages. The cave passage directions and the resulting rose diagram were found by measuring length and direction of each passage, and use these values to stack up total length for each measured direction. Then a macro in Excel was used to split up each direction in one meter segments, and the values were used as input for dip direction in GeoRose 0.4.0, designed by Yong Technology Inc.

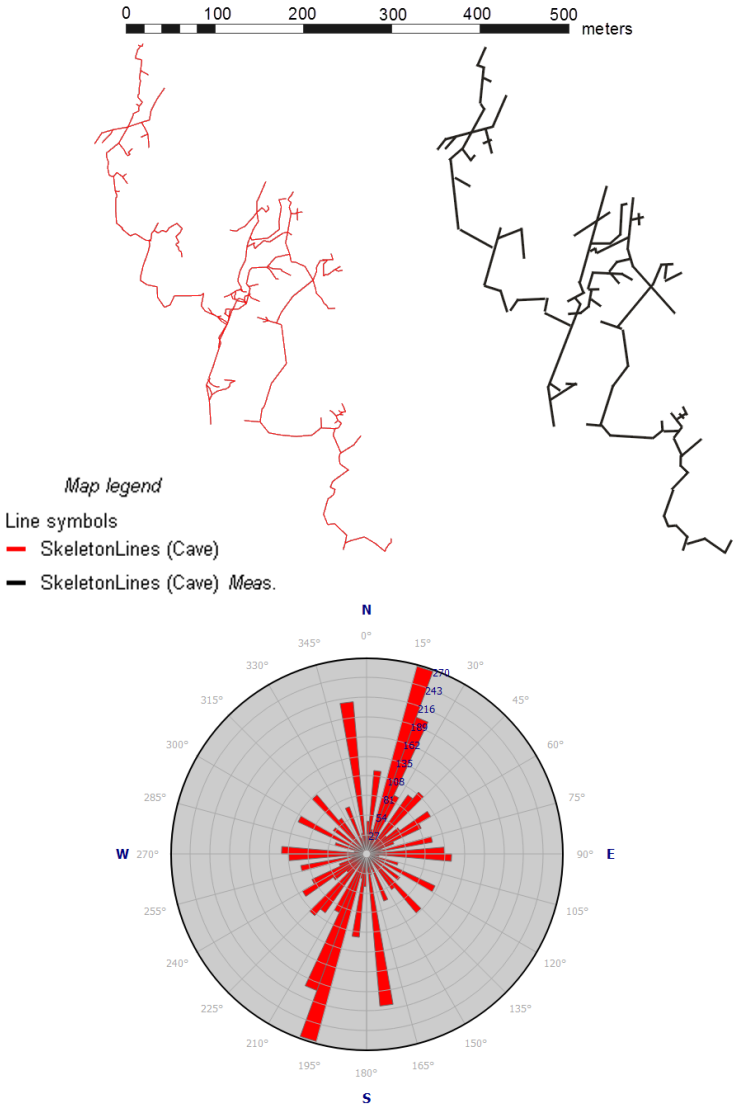


*Figure 2.1.8-1 Fracture rose of cave passages. Three main fracture directions are 15, 90, and 170 degrees. Figure from GeoRose 0.4.0, designed by Yong Technology Inc. These are cumulative lengths of measured fracture directions.*

This rose diagram suggests three main fracture directions, which are listed in Table 2.1.8-1 below. These directions are used as input to fracture modeling in RMS. We see that the assumption in Chapter 2.1.5 to set the grid rotation to an angle of 15 degrees, matches one of the main fracture directions of the cave system.

*Table 2.1.8-1 Input for fracture modeling in RMS.*

| Fracture name | Orientation [degrees] | Orientation variability | Fracture Thickness [m] | Density [fractures/m] | Length [m] | Length Variability |
|---|---|---|---|---|---|---|
| Frac15 | 15 | 5 | 1 | 1 | 50 | 5 |
| Frac90 | 90 | 5 | 1 | 1 | 50 | 5 |
| Frac170 | 170 | 5 | 1 | 1 | 10 | 1 |

The rest is set to default RMS values.

*Table 2.1.8-2 Default RMS values in fracture modeling.*

| | |
|---|---|
| Aperture [µm] | 50 |
| Stiffness | 0.8 |
| Thickness variability | 0 |
| Truncation probability | 1 |

A *fracture model* is created based on Table 2.1.8-1 and presented in Figure 2.1.8-2.

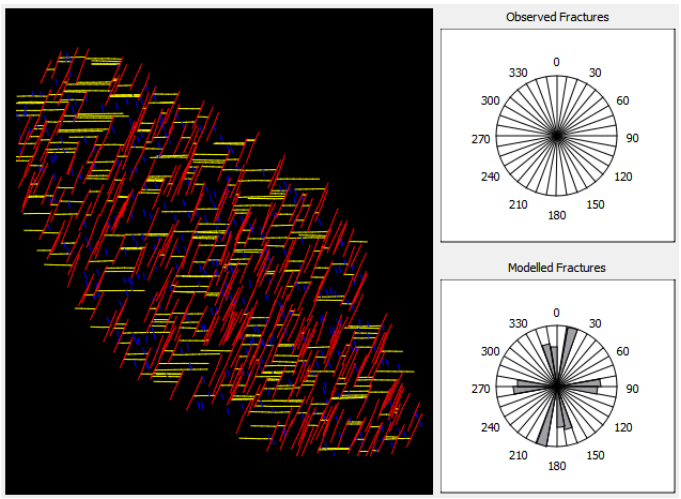


*Figure 2.1.8-2 Screenshot showing modelled fractures in RMS in one grid layer. The fractures are distributed stochastically based on input values from Table 2.1.8-1*

The fracture modeling module in RMS facilitates *dual-porosity modeling* and *single-porosity modeling*. Dual-porosity modeling is used to create the fracture porosity based on input from the fracture model (i.e, fracture length, aperture and orientation). The fracture porosity is added to the porosity parameter using the calculator in RMS, so that the final porosity parameter is ready for export in the reservoir model. Single-porosity modeling, however, is used to create permeability parameters in X and Y direction. Here the fracture permeability is added to the matrix permeability and two new permeability parameters are created for the X and Y direction respectively. There is, however, no function to add fracture permeability in the Z-direction, so this remains the same. This is a shortcoming of the software which will lead to the vertical permeability being underestimated. This will not be further addressed here as it goes beyond the scope of this thesis.

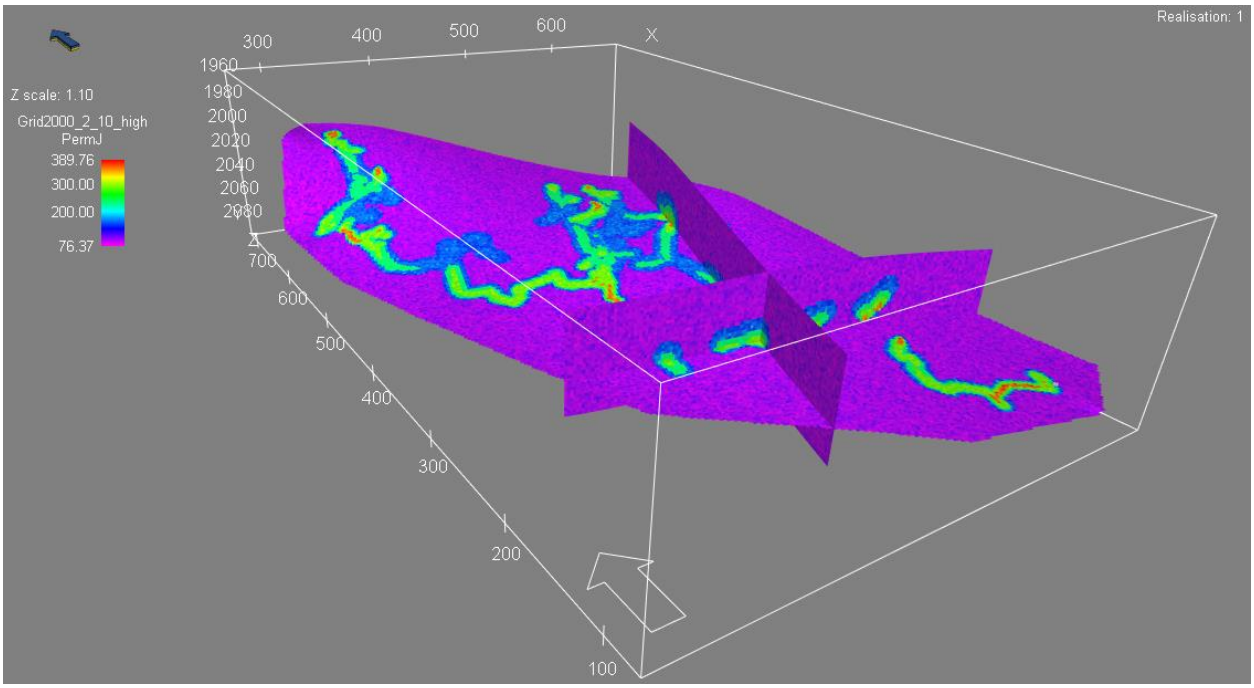


*Figure 2.1.8-3 Cross sections of high case permeability (Y-direction) distribution with $R_2$ = 10 meters including fractures. Notice the decreasing permeability outwards. Compare to Figure 2.1.7-9, the permeability has increased with 46.79 mD.*

### 2.1.9 Upscaling of grid model for fluid flow

Geo-models commonly contain a lot of detailed information, not all of this information has bearing on flow behavior. To save computing time while simulating fluid flow in Eclipse, it is important to minimize the number of grid cells used while maintaining enough detail to ensure that features critical to fluid flow are captured. The process of reducing the number of grid cells by merging them is known as upscaling. A simulation model normally has a coarser grid-resolution than the geological grid model. It is important to ensure that no information that could influence flow is lost during upscaling. A number of test runs were carried out on each model to check the performance of the upscaling.

Roxar (2013b) defines rescaling as the process of assigning values to an *Output Grid* based on the values in an *Input Grid* with different geometry, or in this case the same model volume with a coarser grid. Typically, an input grid is a result of a geological modeling process, while an output grid is designed for flow simulation. In general:

- Upscaling - The output grid is coarse, while the input grid has a finer resolution
- Downscaling - The output grid is fine while the input grid is coarse

The output grid should ideally be aligned with the input grid and cover approximately the same volume. (Roxar, 2013c, Roxar, 2013a).

New Grid models were created (Table 3.1.1-1). They were generated in the same manner as described above for *Grid2000_2*. The only difference is that they have 4, 8, 16, and 32 meters grid cell diameter. A grid cell diameter of 4 meters, results in a 64 $m^3$ grid cell. As the grid cells are cubes, each side should be equal length. Redefining grid resolution is straightforward, the challenging part is to recalculate parameter properties for these cells. This is carried out by *Rescaling* (*Tasks – Flow properties – Rescaling*). As input grid model, *Grid2000_2* is used. The main properties to assign to the four new grid models are porosity (1 parameter) and permeability (3 parameters for X-, Y- and Z-direction. The available rescaling methods for porosity and permeability in RMS are given in Table 2.1.9-1 below.

*Table 2.1.9-1 Available rescaling methods for porosity and permeability in RMS. Green mark on used methods.*

| Output type | Input type | Method |
|---|---|---|
| Porosity | Parameter | Arithmetic |
| Permeability | Parameter | Diagonal tensor |
| | | Arithmetic |
| | | Geometric |
| | | Harmonic |
| | | Power |
| | | Arithmetic-Harmonic |
| | | Harmonic-Arithmetic |
| | | Full tensor |
| | | Well permeability |

For porosity, the choice of rescaling method is easy. The *arithmetic* method is used.

For permeability, there are several methods available, and the choice of method can affect the results. For this case, the *diagonal tensor* method is sufficient, and has been chosen. *Full tensor* method would be the best, but Eclipse cannot handle a total of six directional permeability's. Problems with rescaling can occur in the transition between the high permeability in the collapsed cave, and the lower permeability outside the cave. This because the averaging of cell parameters in these cases become challenging. This will not be further addressed as it goes beyond the scope of this thesis.

*Arithmetic mean* averages all of the grid squares in the fine grid into the new square.

*Diagonal tensor* method solves a pressure system for each cell with certain boundary conditions.

A detailed evaluation of the upscaling methods implemented in RMS is outside the scope for this thesis. For theory behind these methods, see the Roxar (2013a, 2013b) user manual.

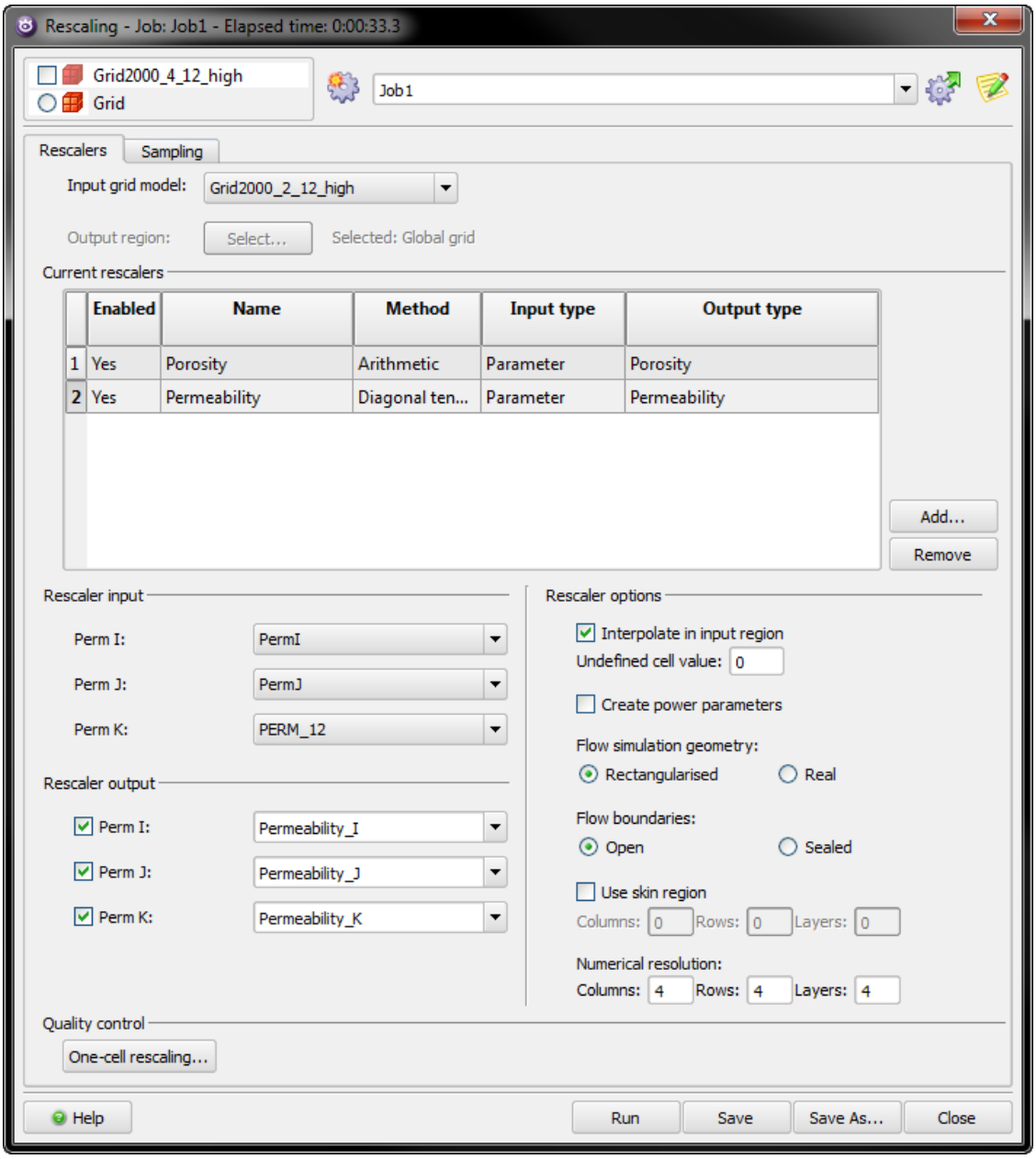


*Figure 2.1.9-1 Rescaling from GRID2000_2_12_high to GRID2000_4_12_high. From the names it follows that high case including collapsed cave with radius 12 meter is upscaled from grid cell diameter 2 to 4 meters. It follows that 8 grid cells in the finer grid becomes one in the coarser grid. See Appendix Chapter 7.1.1 for grid model names.*

### 2.1.10 Export of grid (RMS) model to simulation model (Eclipse)

A total of 26 grid models (see list Table 3.1.1-1) were exported as Eclipse simulation models. Figure 2.1.7-1 shows the eight cases for grid cell dimension 2m × 2m × 2m. Identical sets of 8 cases where produced using cell dimensions of 4m × 4m × 4m and 8m × 8m × 8m. Two additional low-resolution cases for "low case" (i.e. host rock porosity of 5 %) with a collapsed radius 10 meters were generated, having grid cell dimension of 16m × 16m × 16m and 32m × 32m × 32m respectively. Names of grid and simulation models are explained in Appendix 7.1.1 and 7.1.2. Figure 2.1.10-1 shows how simulation models are exported from RMS, and which petrophysical parameters are included. The simulation model uses porosity- and permeability (in three directions) including fractures as described in Chapter 2.1.8.

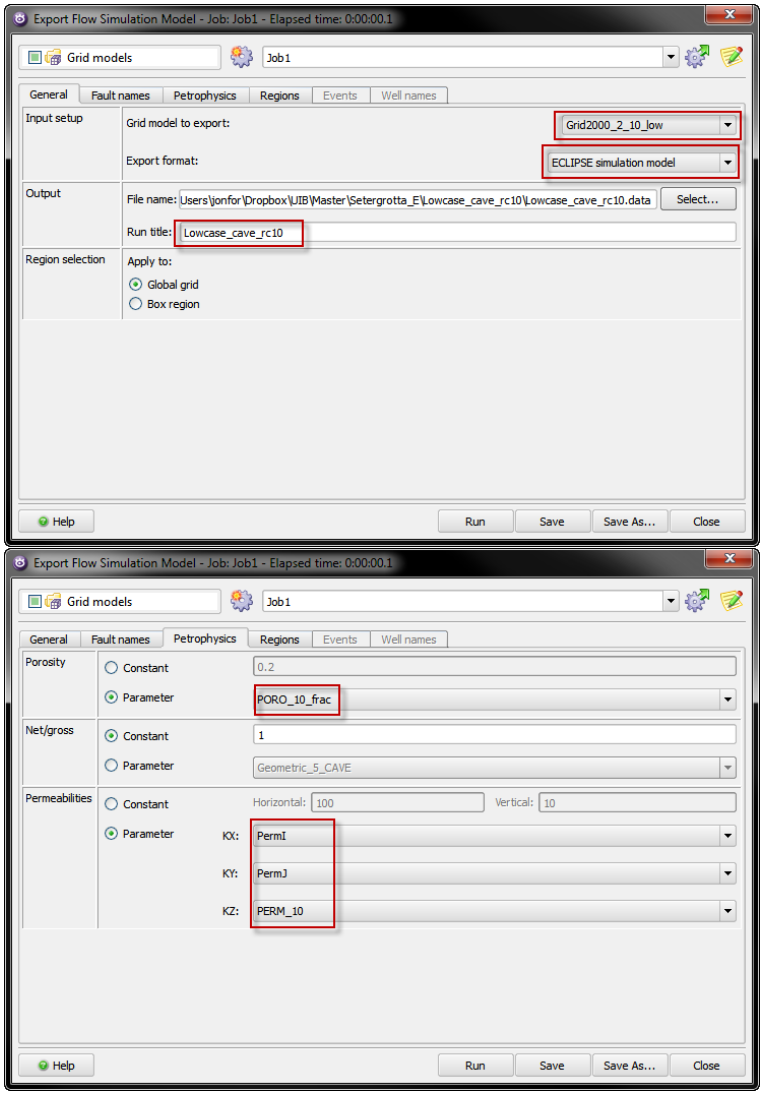


*Figure 2.1.10-1 how simulation models are exported in RMS, and which petrophysical parameters are included. The simulation model uses porosity- and permeability (in three directions) including fractures as described in Chapter 2.1.8.*

## 2.2 Eclipse; simulation of fluid flow

### 2.2.1 Introduction to Eclipse

The RMS models were exported as Eclipse flow simulation models. Some of the default values from the exported simulation settings were changed and are discussed in the following sub-chapters. A complete .data-file, Lowcase_cave_rc10.data, is attached in the Appendix Chapter 7.3 as an example. The names of the .data-files are largely self-explanatory: First it states whether the model is high- or low case with respect to porosity, secondly whether it includes a cave (else nocave). If the model includes a cave, the radius after collapse is defined (here 10 meters, as it follows from the name rc10). Throughout this thesis, 40 different cases have simulated with respect to high- and low case, cave radiuses, upscaling, and increased maximum injection rate (see Table 3.1.1-1. Although the .data-file was exported as a fluid simulation model from RMS, it is modified quite a bit to obtain the best result and layout, as outlined below.

### 2.2.2 RUNSPEC section

The RUNSPEC section defines run specifications. It includes a description of the run, such as grid size, table sizes, number of wells, which phases to include and so forth. The title of the .data-file was changed to *Lowcase_cave_rc10* the name of the .data-file. Start date was set to 01. January 2014, and the system was defined as a dead oil system (only oil and water).

The linear solver stack size, NSTACK, was set to the value 100 (equal to LITMAX, which specifies the maximum number of linear iterations in a Newton iteration). NSTACK is set equal to LITMAX if enough memory on computer. NUPCOL was raised to 10, as a result of a warning while simulating that the value should be raised from 3.

### 2.2.3 GRID section

The GRID section defines the grid dimensions and shape, including petrophysics (porosity, permeability, net-to-gross etc.). This was all kept default from the export .data-file from RMS.

### 2.2.4 PROPS section

The PROPS section defines fluid and rock properties such as relative permeability, PVT data, rock compressibility, surface density and dissolved gas concentration. Values are defined in the .data-file in the appendix. These values are kept constant in all simulation cases. Below, two figures showing the relative permeability curves for oil and water, and PVT data for dead oil are presented. The data presented in the curves are derived from a semester assignment (exam) in the Reservoir Simulation course (MAT255), at the University of Bergen spring semester 2013.

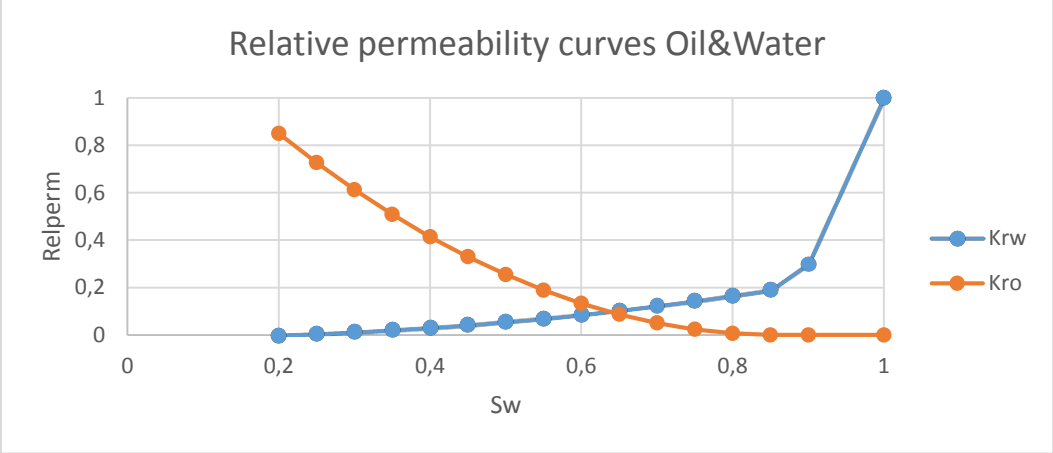


*Figure 2.2.4-1 Relative permeability curves for oil (Kro) and water (Krw)*

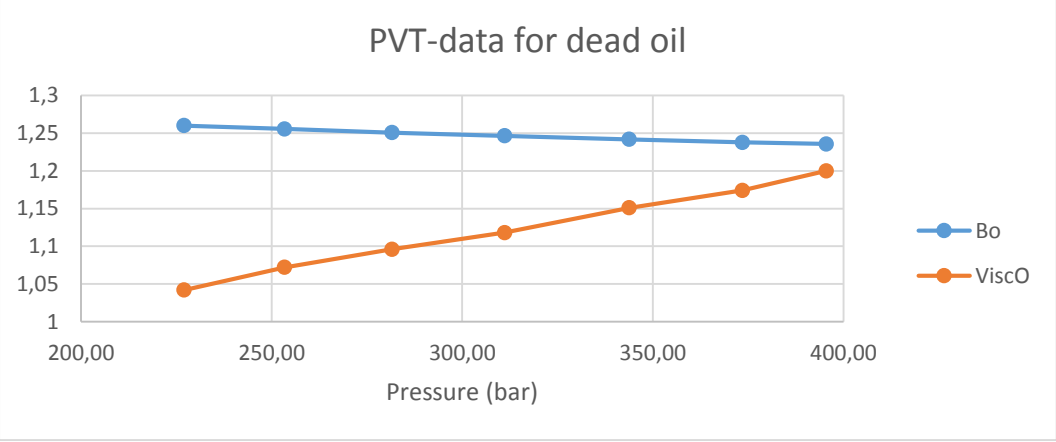


*Figure 2.2.4-2 PVT-data for dead oil. Bo – Volume formation factor for oil, ViscO – Oil viscosity.*

### 2.2.5 REGIONS section

The REGIONS section is used to give user defined report regions. All is kept default from the exported .data-file from RMS, there is only one region.

### 2.2.6 SOLUTION section

The SOLUTION section gives the models equilibration data e.g. a description of how the model is to be initialized. "The *EQUIL* keyword sets the contacts and pressures for conventional hydrostatic equilibrium" (Schlumberger, 2013). The oil-water contact is defined below the reservoir to get a completely oil-filled reservoir with no mobile water present. The gas-oil contact is defined above the reservoir to avoid including gas in model.

### 2.2.7 SUMMARY section

This section is used to define simulation output by specifying which data items to write to report files.

### 2.2.8 SCHEDULE section

The SCHEDULE section specifies the operations to be simulated in Eclipse. This includes production and injection controls and constraints, and the times at which output reports are required (Schlumberger, 2013). See SCHEDULE section in .data-file in Appendix, Chapter 7.3, for the setup. The setup is the same for all simulation cases, with minor changes such as well placement (fewer grid cells as grid cell diameter increases) for upscaled models, and production and injection rates for high- and low case. To be able to compare the different simulations, production and injection rates are kept constant within the high- and low cases.

Wells are defined, as well as tuning parameters and time control. Table 7.1.5-1 in Appendix 7.1.5 summarizes the placement of wells *WP1* (Well Producer 1), *WI1* and *WI2* (Well Injector 1 and 2) in all models. Varying grid cell size leads to different cell numbers were the wells are completed. Visual inspection ensures that the wells are completed at the same location for all cases.

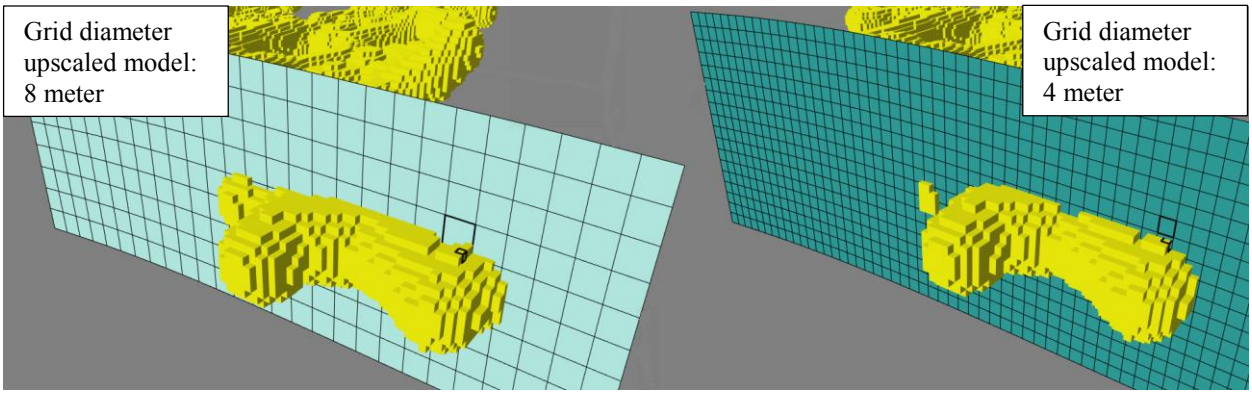


*Figure 2.2.8-1 Visual inspection of grid cells that give approximately the same well placement in the different upscaled grid models. The original well placement in the grid with cell diameter of 2 meters is used as base for the other grids.*

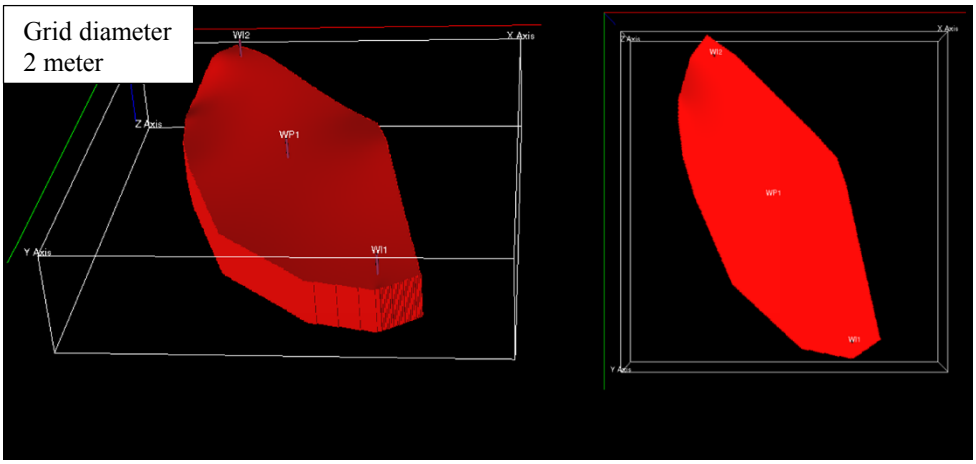


*Figure 2.2.8-2 Well placement original (not upscaled) model. Grid diameter 2 meter. WP1 (Well Producer 1), WI1 and WI2 (Well Injector 1 and 2)*

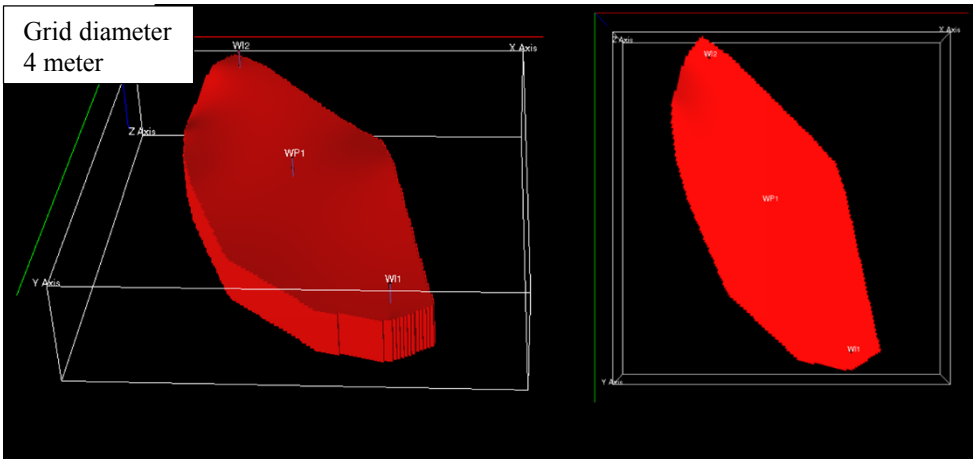


*Figure 2.2.8-3 Well placement upscaled model. Grid diameter 4 meter. WP1 (Well Producer 1), WI1 and WI2 (Well Injector 1 and 2)*

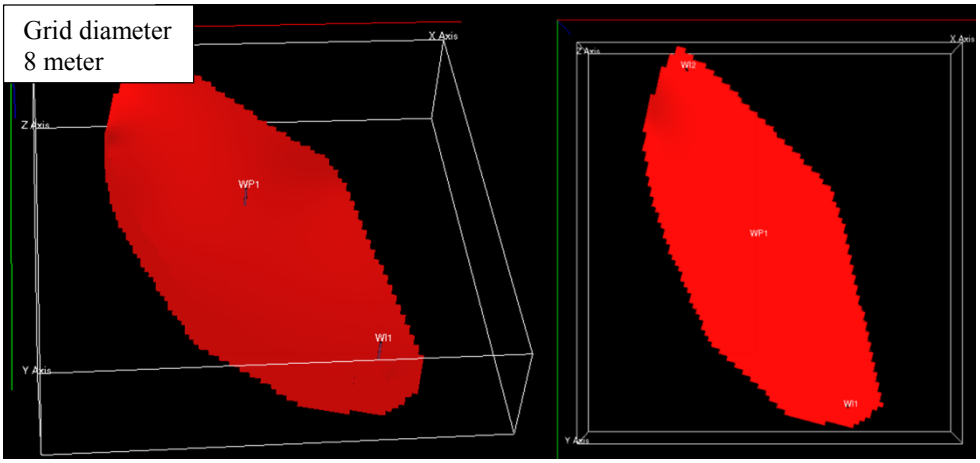


*Figure 2.2.8-4 Well placement upscaled model. Grid diameter 8 meter. WP1 (Well Producer 1), WI1 and WI2 (Well Injector 1 and 2)*

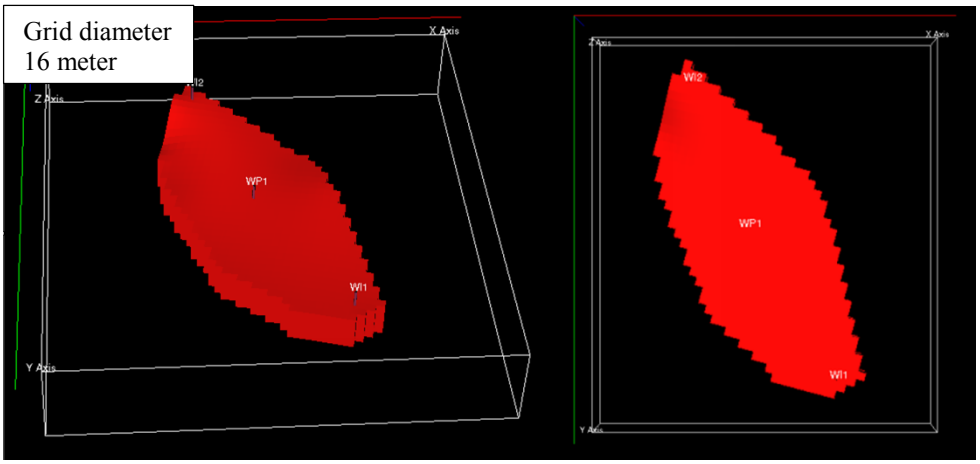


*Figure 2.2.8-5 Well placement upscaled model. Grid diameter 16 meter. WP1 (Well Producer 1), WI1 and WI2 (Well Injector 1 and 2)*

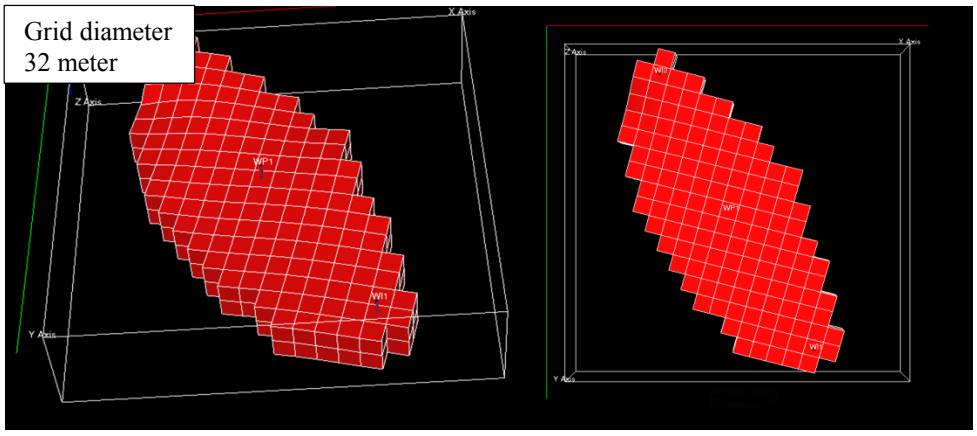


*Figure 2.2.8-6 Well placement upscaled model. Grid diameter 32 meter. WP1 (Well Producer 1), WI1 and WI2 (Well Injector 1 and 2)*

The production rates are defined (using *WCONPROD* keyword) based on complete drainage of the reservoir in 10 years. For high case the volume of oil in place is approximately 1387000 $Sm^3$. Production distributed over 10 years gives a daily production of 380 $Sm^3$/day. For low case, the production was set to 100 $Sm^3$ based on the same calculation with a lower oil volume. Total maximum injection rate (spread equal on the two injection wells) for high- and low case is set to 400 $Sm^3$ and 100 $Sm^3$ respectively (with *WCONINJE* keyword).

It is however not expected that the reservoir can produce all of the oil in place. The pressure loss and water production will ensure that production rates will eventually fall. The list of report dates were set with the *DATES* keyword. It was set write report files every 1st of the month, with the first report date set to 1. Feb 2014 and the last to 1. Jan 2029. This gives a simulation run for 15 years.

The *TUNING* keyword was set to default on all values except those presented in Table 2.2.8-1.

*Table 2.2.8-1 Values not defaulted in TUNING keyword in SHEDULE section*

| Parameter | Description of parameter | Value |
|---|---|---|
| TSINIT | Maximum length of next time step | 0.1 |
| TSMAXZ | Maximum length of time steps after the next | 5 |
| TSMINZ | Minimum length of all time steps | 0.1 |
| NEWTMX | Maximum number of Newton iterations in a time step | 40 |
| NEWTMN | Minimum number of Newton iterations in a time step | 1 |
| LITMAX | Maximum number of linear iterations in a Newton iteration | 100 |
| LITMIN | Minimum number of linear iterations in a Newton iteration | 1 |

*LITMAX* was set to the same value as *NSTACK* in the RUNSPEC section. Other changes were made because of the number of warnings that appeared during simulation, telling to increase certain values. *LITMAX* specifies the maximum number of linear iterations in a Newton iteration. To avoid the calculations to run circles, a high enough NSTACK has to be set. Usual these two are set equal.

The keyword *GCONINJE* (Group Control Injection) was included to try to reduce pressure loss in reservoir under production. The record *VREP* under *GCONINJE* keyword ensures that the pressure

is stable, by increasing or decreasing water injection. The purpose of including this, is to match the total reservoir volume injection rate of the field with its production voidage rate. The specified water injection rate under *WCONINJE* keyword, is the maximum injection rate, this means that if the production voidage rate demands another injection rate to maintain the reservoir pressure it will adjust automatically. If however, maximum injection rate is set to low, this will not be possible.

The data-file was ended with the *END* keyword.

# 3 Results and discussion

## 3.1 Results and discussion

This thesis presents a workflow for modeling paleokarst reservoirs in RMS using information about the geometry of a pre-existing cave system as a starting point. Furthermore, an attempt is made to investigate how fluid flow will be affected by changing certain model parameters. The effect of changing the radius of the collapse is investigated and the impact of upscaling the reservoir model is studied. Finally, some simulation results are presented to illustrate fluid flow behavior in this reservoir model. The results can be used by the industry to compare with real time production curves from karst reservoirs. The publicly available data on this type of research is limited and therefore simulation results can at present not be compared to any similar previous work or examples.

### 3.1.1 The paleokarst reservoir model

One of the main results of the present study is a workflow for building reservoir models representing a real case geometry of a collapsed cave system. The method provides the basic concepts for building reservoir models using any conceivable cave geometry as a starting point. In other words, if a skeleton line of a cave geometry is provided (based on any real- or synthetic data), it will be possible to recreate this geometry in RMS as parts of a reservoir model.

To sum up the methods chapter (see Figure 3.1.1-1, numbers (x) in the text indicates the marks in the figure), a survey point dataset from Setergrotta cave is used to create a skeleton line of the cave geometry (1). Further, the stratigraphic framework was created and the horizons were mapped (2). These mapped horizons were used to create a structural model and horizon model (3), which were essential for creating a grid (4). The grid consists of 1323735 grid cells with diameter 2 meters. Total reservoir volume equals $1323735 \times 2 \times 2 \times 2\ \mathrm{m}^3 \approx 10.6\ \mathrm{MSm}^3$. Further, geometric modeling (5) defines the radial distance from the refined points of the skeleton line, and is used to create the original cave geometry with radius 5 meters (6). Another seven geometric models are created to be able to assign petrophysical values and recreate the decreasing porosity and permeability trend from cave bottom to the collapsed cave roof (7). After assigning petrophysical values to the models (8), fractures (9) are introduced. These fractures increase the porosity and permeability of the reservoir model. The final model (10) includes fractures.

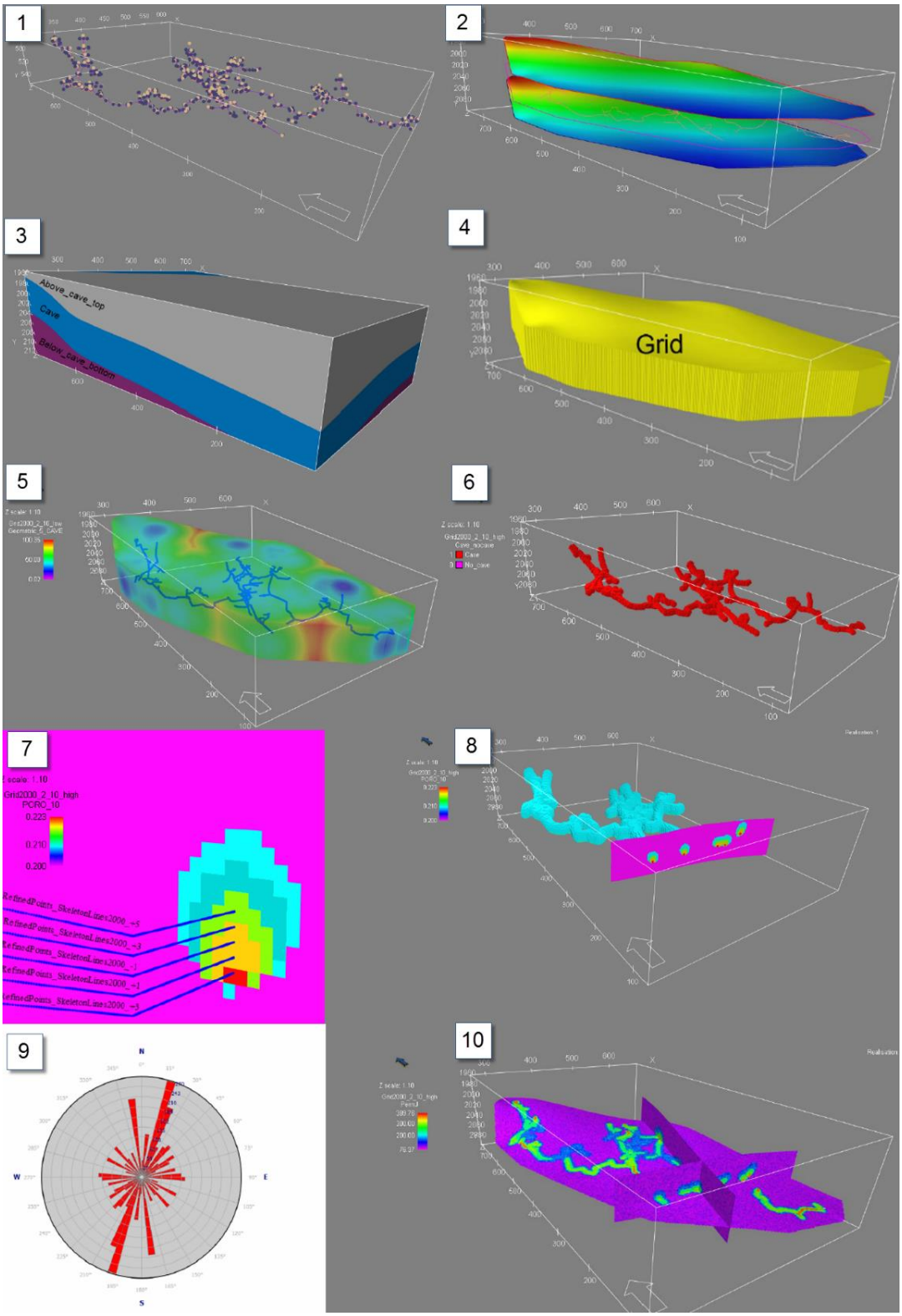


*Figure 3.1.1-1 Figure that sums up building the models in RMS. (1) measure points/skeleton line, (2) stratigraphic framework/horizon modeling, (3) structural model/horizon model, (4) grid model, (5) geometric model, (6) cave with radius $R_1$ = 10 meters, (7) assigning petrophysical properties with different geometric models, (8) petrophysical properties, (9) fracture rose, (10) final model with fractures.*

Finally, the eight cases described in Figure 2.1.7-1 were upscaled to grid cell dimensions of 4, 8, 16, and 32 meters to run test on the effects of upscaling. All reservoir models listed in Table 3.1.1-1 were exported as Eclipse simulation models, and simulated with the production- and maximum injection rates specified, as well as well placement described in Figure 2.2.8-2, Figure 2.2.8-3, Figure 2.2.8-4, Figure 2.2.8-5, Figure 2.2.8-6, and Table 7.1.5-1. The maximum injection rate had to be increased for some of the simulations to maintain the reservoir pressure with the GCONINJE-keyword, as described in Chapter 2.2.8.

The suite of "high case" paleokarst reservoir model refers to a background/host rock porosity of 20%, while "low case" refers to models with a background/host rock porosity of 5 % (see Chapter 2.1.7). If a collapsed cave is present, porosity and permeability values are higher within the radius of the collapsed cave, than in the background. For the models used here, the collapsed cave radius ($R_2$) was set at 10, 12 and 14 meters. Grid cells used here are cubes, and grid cell dimension is 2 meters for the original reservoir model, while the upscaled models have a grid cell diameter of 4, 8, 16, and 32 meters. In Chapter 2.2.8, it is mentioned that it is desirable to maintain the pressure within the reservoir. Hence, the GCONINJE-keyword defines the maximum injection rate, and had to be set higher for some simulations (see Table 3.1.1-1). Consequently, a distinction between a low- and high maximum injection rate for low case (100 and 200 $Sm^3$/day respectively) and high case (400 and 800 $Sm^3$/day respectively) has been made.

*Table 3.1.1-1 A total of 40 simulations were carried out throughout this thesis. 26 different cases (blue color) with respect to high- and low case, geometry, and upscaled versions. In addition to this 14 re-simulations (green color) were carried out with injection rates doubled (we will come back to why in Chapter 3.1.4).*

| Grid cell Diameter [m] | High/Low case | Radius collapsed cave [m] | Production rate [$Sm^3$/day] | Max Injection rate [$Sm^3$/day] |
|---|---|---|---|---|
| 2 | High | No cave | 380 | 400 |
| 2 | High | 10 | 380 | 400 |
| 2 | High | 12 | 380 | 400 |
| 2 | High | 14 | 380 | 400 |
| 4 | High | No cave | 380 | 400 |
| 4 | High | 10 | 380 | 400 |
| 4 | High | 12 | 380 | 400 |
| 4 | High | 14 | 380 | 400 |
| 8 | High | No cave | 380 | 400 |
| 8 | High | 10 | 380 | 400 |
| 8 | High | 12 | 380 | 400 |
| 8 | High | 14 | 380 | 400 |
| 2 | Low | No cave | 100 | 100 |
| 2 | Low | 10 | 100 | 100 |
| 2 | Low | 12 | 100 | 100 |
| 2 | Low | 14 | 100 | 100 |
| 4 | Low | No cave | 100 | 100 |
| 4 | Low | 10 | 100 | 100 |
| 4 | Low | 12 | 100 | 100 |
| 4 | Low | 14 | 100 | 100 |
| 8 | Low | No cave | 100 | 100 |
| 8 | Low | 10 | 100 | 100 |
| 8 | Low | 12 | 100 | 100 |
| 8 | Low | 14 | 100 | 100 |
| 16 | Low | 10 | 100 | 100 |
| 32 | Low | 10 | 100 | 100 |
| 2 | High | No cave | 380 | 800 |
| 2 | High | 10 | 380 | 800 |
| 2 | Low | No cave | 100 | 200 |
| 2 | Low | 10 | 100 | 200 |
| 4 | High | No cave | 380 | 800 |
| 4 | High | 10 | 380 | 800 |
| 4 | Low | No cave | 100 | 200 |
| 4 | Low | 10 | 100 | 200 |
| 8 | High | No cave | 380 | 800 |
| 8 | High | 10 | 380 | 800 |
| 8 | Low | No cave | 100 | 200 |
| 8 | Low | 10 | 100 | 200 |
| 16 | Low | No cave | 100 | 200 |
| 32 | Low | 10 | 100 | 200 |

### 3.1.2 The effect of the collapsed cave radius

One of the research questions in this thesis deals with the radius of the collapsed cave ($R_2$), and if this radius will affect the production. To investigate this, graphs for both high case (Figure 3.1.2-2) and low case (Figure 3.1.2-3) are presented for the paleokarst reservoir model with grid cell diameter 2 meters. The Field Oil Production Ratio (FOPR) [$Sm^3$/day], Field Pressure (FPR) [bar], and the Field Water Production Rate (FWPR) [$Sm^3$/day] were compared for the case with no cave present, and with a collapsed cave present with radius ($R_2$) equal to 10, 12, and 14 meters (see Figure 3.1.2-1).

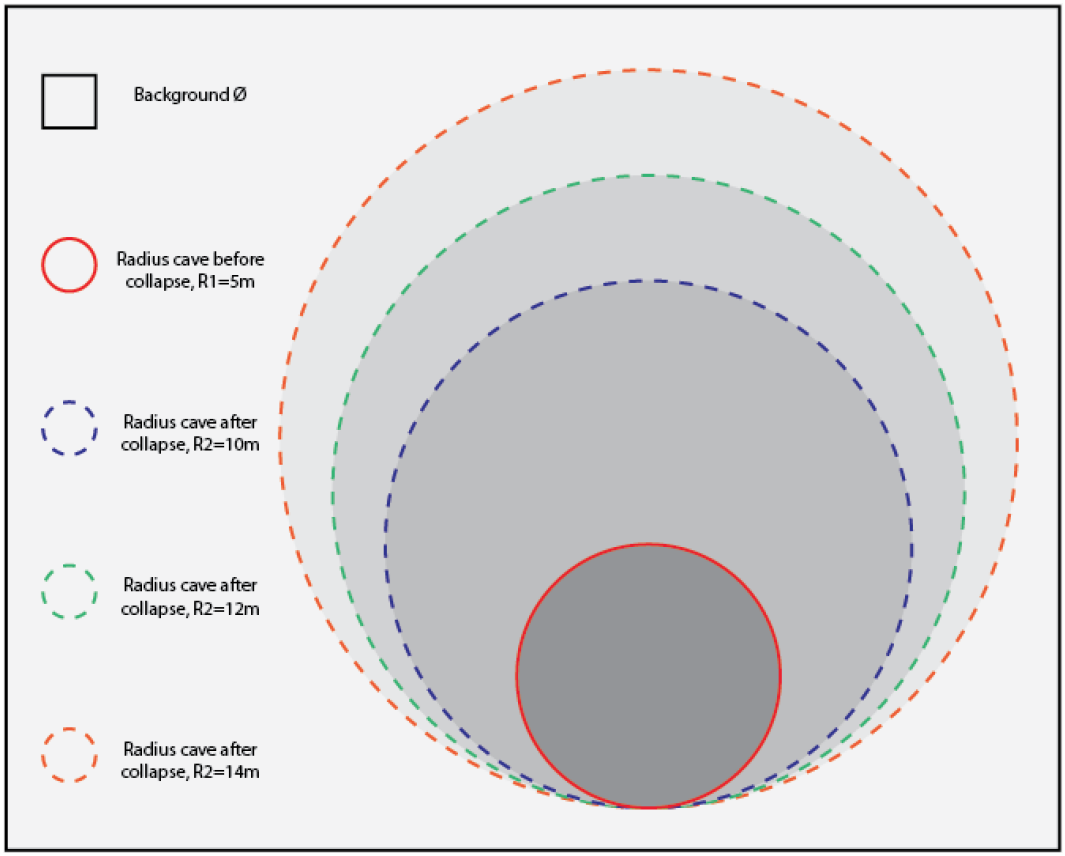


*Figure 3.1.2-1 The different collapsed cave radius ($R_2$) cases, compared to the radius before collapse ($R_1$).*

As shown in Chapter 2.1.7, the different cave collapse radii ($R_2$) represent different porosity and permeability distributions, derived from the original cave radius ($R_1$) which is the same for all cases. Both high- and low case show a difference between the no cave case and the cases with a collapsed cave present (see Figure 3.1.2-2 and Figure 3.1.2-3). However, the graphs for FOPR, FPR and FWPR show no- or minimal difference between the collapsed cave cases.

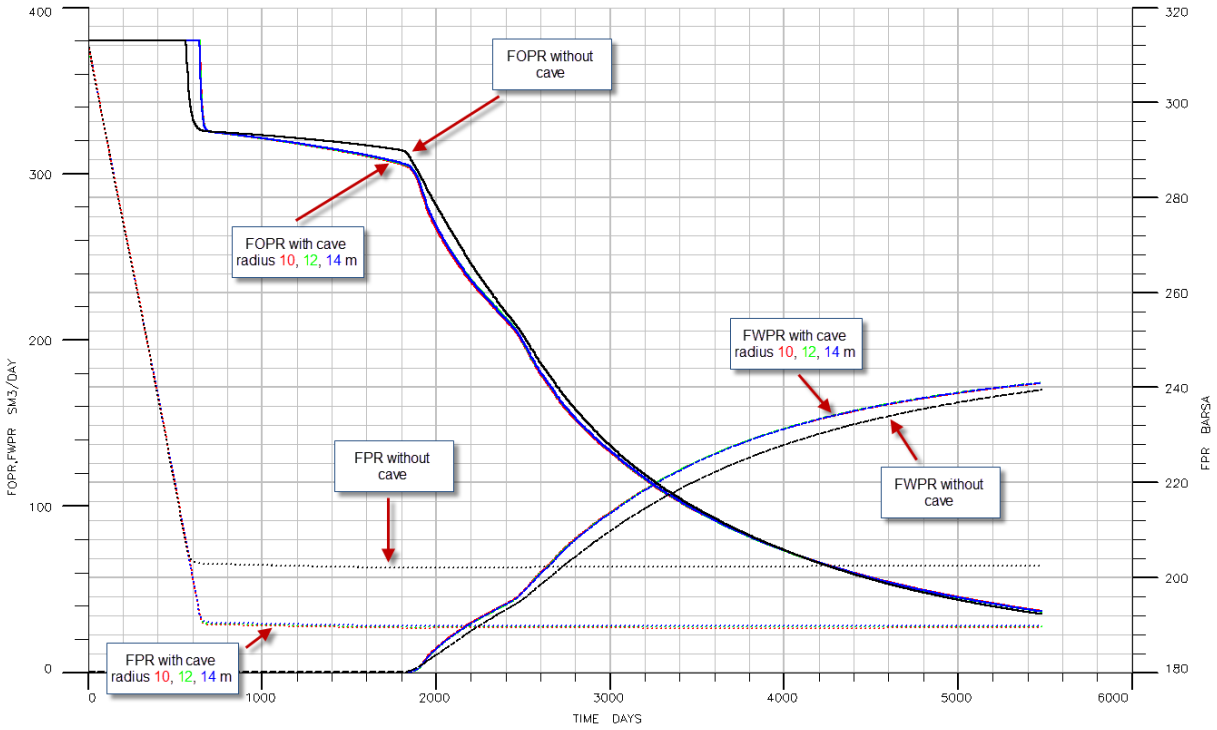


*Figure 3.1.2-2 High case with low injection rate. Test of the effect of the radius of the collapsed cave ($R_2$).*

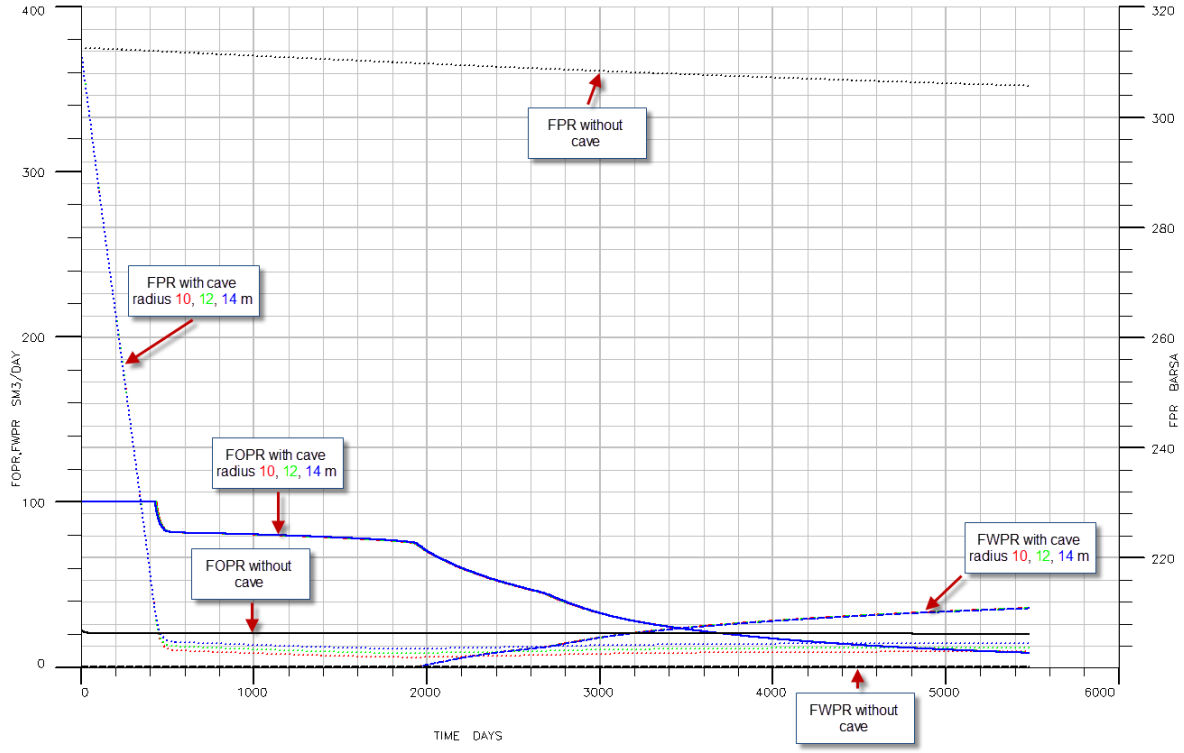


*Figure 3.1.2-3 Low case with low injection rate. Test of the effect of the radius of the collapsed cave ($R_2$).*

It appears that the different collapse radius ($R_2$) cases tested in this thesis yield the same production results. When introducing a void volume (original cave volume with radius ($R_1$) equal 5 meters) to the background, the increase in porosity and permeability added to the background when the cave collapses, will be constant, no matter how big the radius collapse would be. The increase in volume is derived directly from the volume of the original cave geometry and is a constant volume added to the background in all cases.

If the original cave volume had been spread evenly and homogenized the background on an infinite volume, the increase would most likely not be noticed at all. However, since the increase of radius goes from 5 meters ($R_1$) to 10, 12, or 14 meters ($R_2$), the production curves will notice the difference from the no-cave example, but not the difference between the radius increases. Within the scope of test performed in this thesis, no effect is shown from the increase of collapse radius from 10 to 12 or 14 meters. The drainage volume and pore volume remains the same, but the distribution of the volume within these cases, will not matter for the production curves. Figure 3.1.2-4 sums up the observations of the radius ($R_2$) cases, and concludes that there is no difference between the collapsed cave radii. Therefore, the green boxes highlights which cases should be targeted for further research, whereas further work on the red cases has less priority.

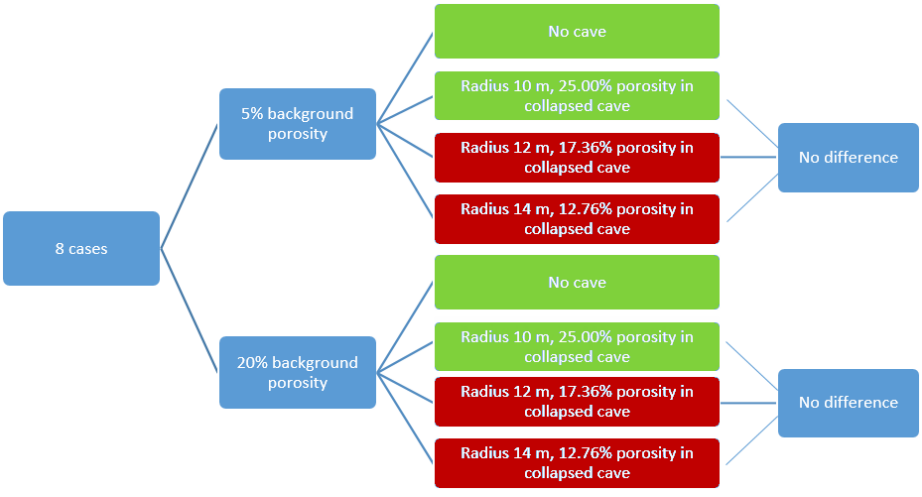


*Figure 3.1.2-4 This figure is an continuation of Figure 2.1.7-1 and sums up the observations done when it comes to the radius of the collapsed cave ($R_2$). It shows that there is no difference between the collapsed cave radiuses, and the green boxes represent the cases for further research, while the red boxes are dropped cases.*

As presented above, there is no difference between the production curves in the paleokarst reservoir models including three different collapsed cave radius cases ($R_2$). It follows that if the radius before collapse ($R_1$) is constant within the boundaries of this thesis, the increase in porosity and permeability is constant and added to the background in all cases, and will result in the same simulation results. However, if cave radius ($R_1$) would be larger, more pore space could potentially be added to the background, and production curves would presumably look different.

For further simulation comparison, it will be sufficient to compare the "no cave" case with one of the collapsed cave cases. For simplicity, the paleokarst reservoir model will include a collapsed cave with radius ($R_2$) equal to 10 meters as Figure 3.1.2-4 illustrates.

### 3.1.3 Upscaling of paleokarst reservoir models

As discussed in Chapter 2.1.9 it is desirable to upscale the reservoir grid model to reduce simulation time. However, the coarsened grid may lose vital information about the reservoir petrophysical properties when merging cells. As an example, eight grid cells in the reservoir model with grid cell dimension 2m × 2m × 2m meters and different parameter values are averaged into one grid cell in the 4 meter grid cell diameter cases. Furthermore, 64, 512 and 4096 grid cells with diameter 2 meters are needed to create one single grid cell in the 8, 16 and 32 meter grid cell diameter cases, respectively. As follows, it is vital that upscaling is well tested before potentially running the rest of the simulations on a coarser grid. Figure 3.1.3-1 shows how the paleokarst reservoir grid model looks on different scales. Visually, much of the collapsed cave structure is still captured at an 8 meter scale. For the 16 and 32 meter scale however, the petrophysical properties are smoothened on a too large scale in order to be able to detect the cave geometry.

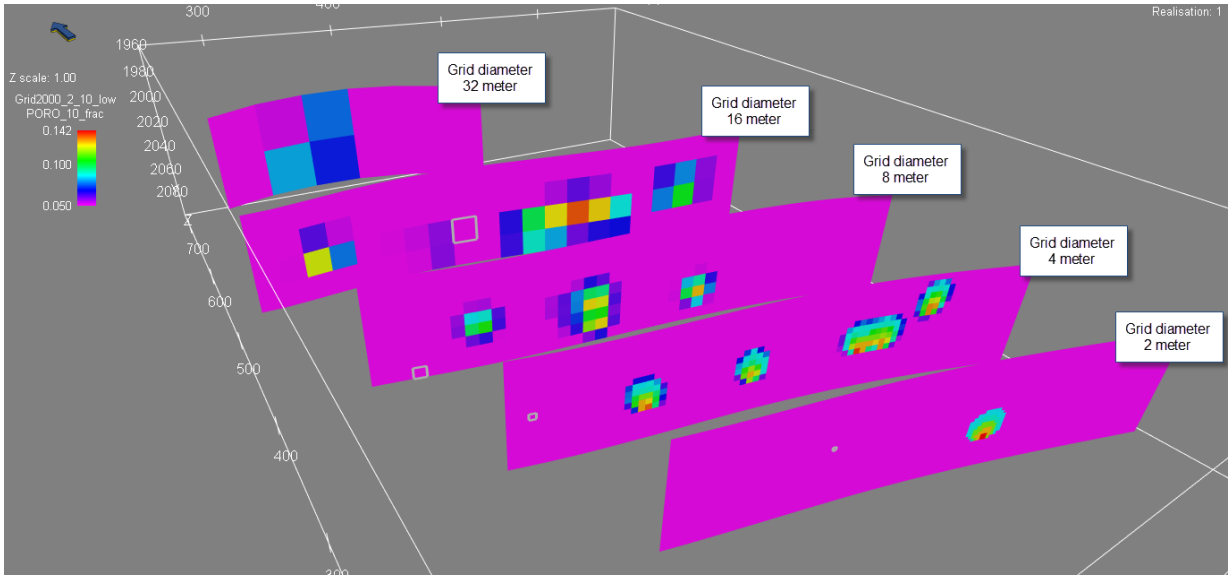


*Figure 3.1.3-1 The figure illustrates how the paleokarst reservoir grid model looks on different scales. Upscaled models have a grid cell diameter of 4,8,16,and 32 meters. Here the porosity distribution for low case with fractures is shown, with a collapsed cave with radius $R_2$ present.*

It becomes obvious that there is a constraint with respect to well placement in the coarser grids, as in the finer grid cells, the wells are placed within the collapsed cave structure, whereas in the coarse models the target becomes less easy to define. The upscaled models should ideally have been upscaled as a power of three; it would then always be possible to set a well in the center point. For the completion depth as well, problems occur, especially for the 32 meter grid cell diameter case. Here there are only two layers to choose between when it comes to well placement and completion.

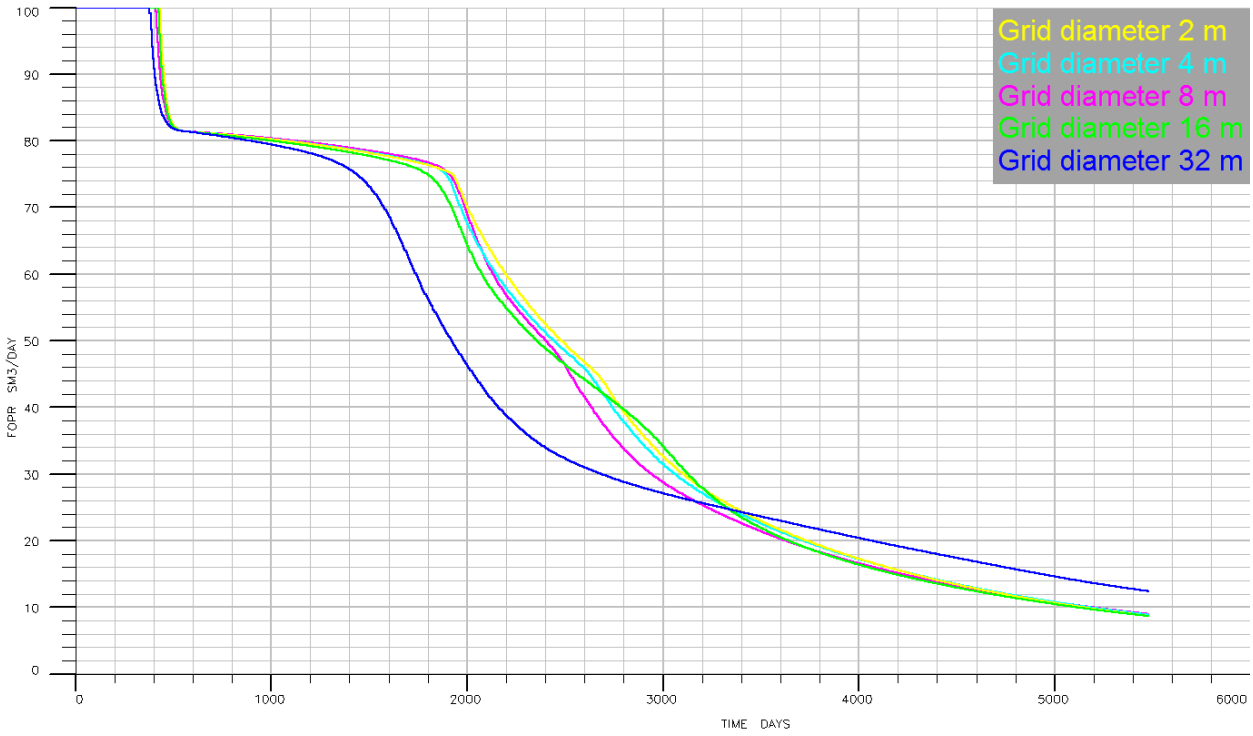


*Figure 3.1.3-2 All curves represent the Field Oil Production Rate (FOPR) for all upscaled cases with a low injection rate. All production curves are simulations from the same case; low case with a collapsed cave radius ($R_2$) equal to 10 meters.*

Figure 3.1.3-2 above represents the Field Oil Production Rate (FOPR) for all upscaled cases with low injection rate. All of the production curves are simulations derived from the same case; low case with a collapsed cave radius ($R_2$) equal to 10 meters. It seems that the production curves more or less are similar for grid cell diameter up to 16 meters. However, the 32 meter grid cell diameter case deviates from the other curves.

Figure 3.1.3-3 below represent the same graph as Figure 3.1.3-2 above. The difference between the two cases however, is that the increased maximum injection rate is doubled. As a result, the FOPR-curves in Figure 3.1.3-3 differ from the ones in Figure 3.1.3-2, but the same observation is made, the 32 meter grid cell diameter case deviates from the other curves.

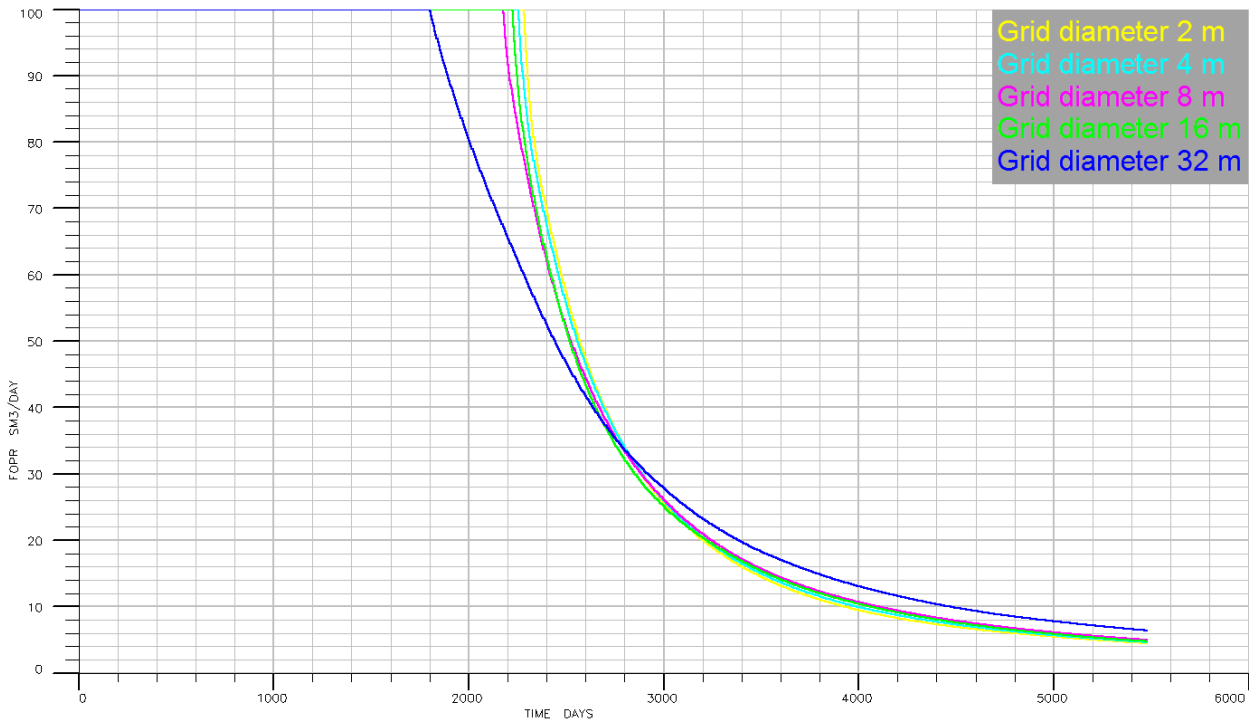


*Figure 3.1.3-3 All curves represent the Field Oil Production Rate (FOPR) for all upscaled cases with a high injection rate. All production curves are simulations from the same case; low case with a collapsed cave radius ($R_2$) equal to 10 meters.*

It seems that if the grid cell diameter exceeds the diameter for the collapsed cave diameter ($R_2 =$ 10 meters, so the diameter $= 2 \times 10 = 20$ meters), the production curves will start to deviate. Even though the paleokarst reservoir model with grid cell diameter of 32 meters deviates from the other cases, it still represents a quite good representation of the oil production. It should however be emphasized that the well placing becomes more difficult for the coarser grid models, and it will be impossible to set the Z-axis well interval to be equal for the 32 and 2 meter grid cell diameter cases. This will have effects on the production curves.

Ø. Pettersen (2015, pers. comm., 14 April) mentioned that the difference between the production curves (up to 16 meter grid cell diameter), could be caused by weight effect of the fluids. The larger grid cells could result in a different flow pattern in Eclipse.

Figure 3.1.3-4 illustrates the time usages in seconds for the simulation of the different upscaled paleokarst reservoir models. The X-axis represents the grid cell diameter in meters, while the Y-axis shows the simulation duration in seconds. The practical utility of upscaling becomes very evident. By increasing the grid cell dimension from 2 meters to 4 meters, simulation time falls

from 18600 seconds (more than 5 hours) to 730 seconds (approximately 12 minutes). In other words, by increasing the grid cell dimension eight times, the time usage cut by 96%. The grid cell diameter of 8 meters uses 64 seconds, while the 16 and 32 meter cases uses 20 and 17 seconds respectively.

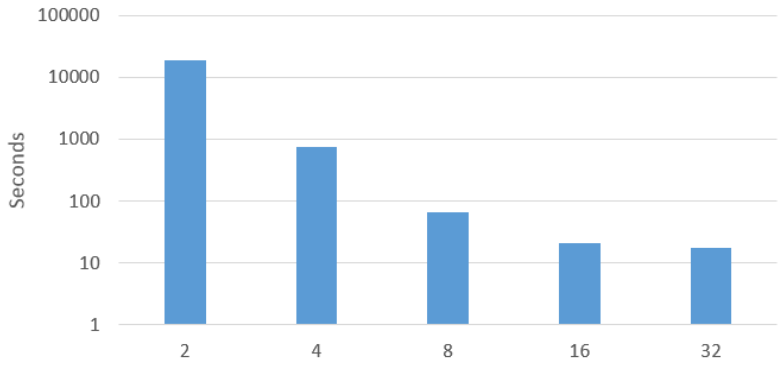


*Figure 3.1.3-4 Time usages in seconds for the simulation of the different upscaled models. The x-axis represent the grid cell diameter in meters, while the y-axis shows the simulation time in seconds.*

### 3.1.4 Production curves in paleokarst reservoirs

Graphs for Field Oil Efficiency (FOE) (see equation 10), Field Pressure (FPR) [bar], Field Oil Production Rate (FOPR) [$Sm^3$/day], Field Water Production Rate (FWPR) [$Sm^3$/day], Field Water Injection Rate (FWIR) [$Sm^3$/day], and Field Water Cut (FWCT) (see equation 11) are presented and compared for the following cases (Figure 3.1.4-1).

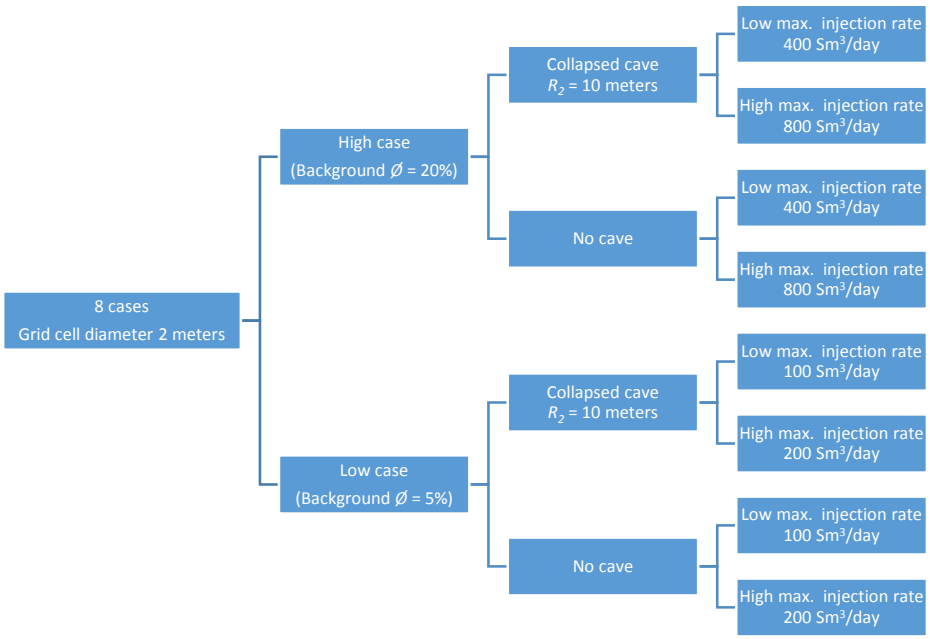


*Figure 3.1.4-1 This figure gives an overview over the different cases where production curves are compared*

$$FOE = \frac{\text{Oil in place}_{\text{initial}} - \text{Oil in place}_{\text{present}}}{\text{Oil in place}_{\text{initial}}} \quad (10)$$

$$FWCT = \frac{\text{Produced water}}{\text{Total liquids produced}} \quad (11)$$

A complete list of symbols is presented in Appendix 7.1.4. Below, the graphs for high- and low case with low injection rate (Figure 3.1.4-2 and Figure 3.1.4-3) are compared.

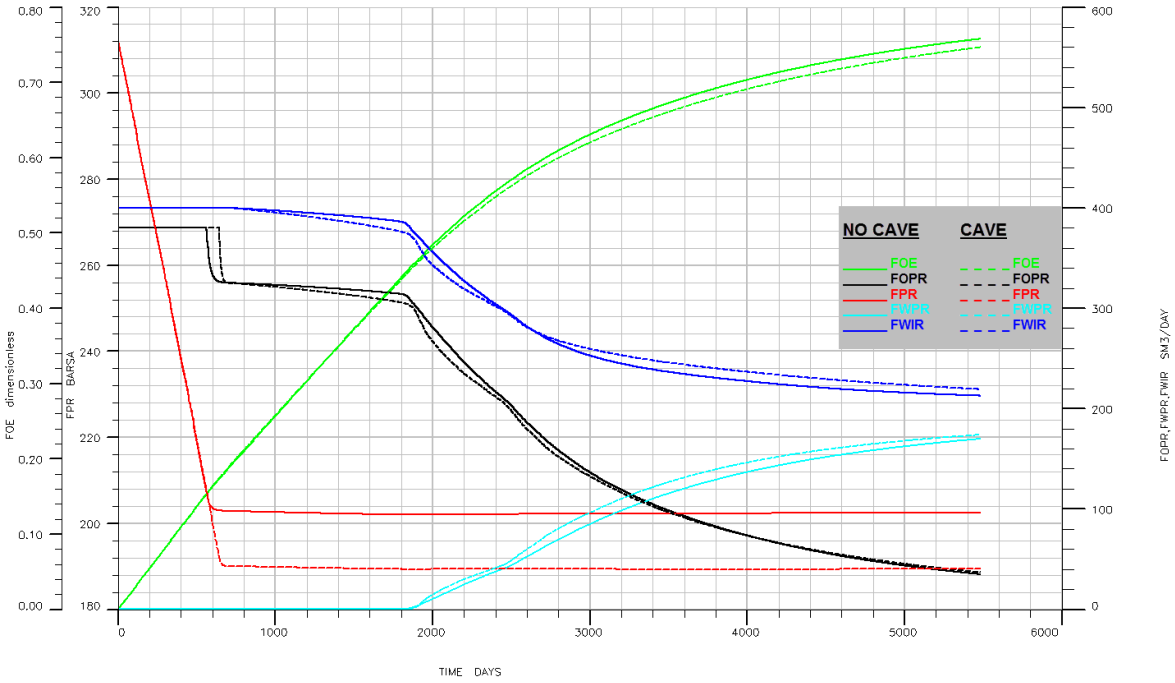


*Figure 3.1.4-2 This graph presents the FOE, FOPR, FPR, FWPR, and FWIR for high case with low injection rate.*

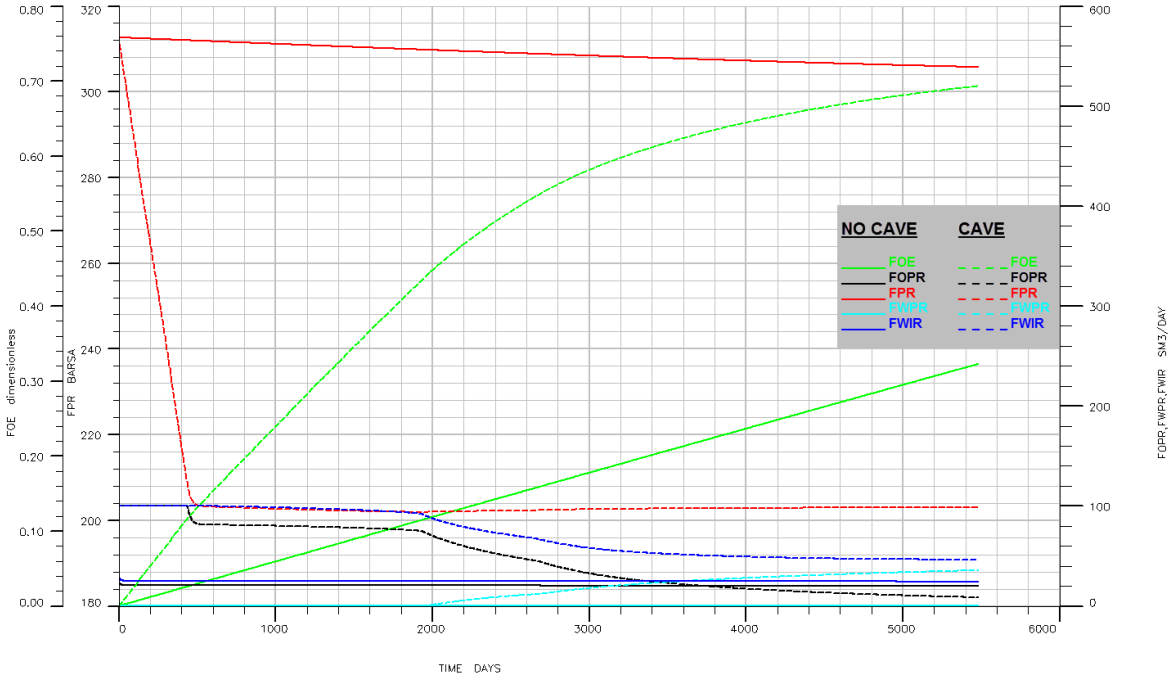


*Figure 3.1.4-3 This graph presents the FOE, FOPR, FPR, FWPR, and FWIR for low case with low injection rate.*

The production curves for high case with low injection rate (see Figure 3.1.4-2) do not differ much from the collapsed cave case and the case without a cave present. The main difference between the two is that the pressure in the collapsed cave case stabilizes at a reservoir pressure (FPR) of 190 bar, while the FPR of the "no cave" case stabilizes at 202 bar. The pressure difference causes a difference between the FOPR curves, as maximum production rate (380 $Sm^3$/day) of the "no cave" case shows an earlier drop than the collapsed cave case. The pressure (FPR) difference between the collapsed cave case and "no cave" case originates from the pressure difference needed to keep fluids from flowing to the well ($\Delta P$ in equation 12). A lower pressure difference between reservoir and well is needed in the collapsed cave case because the well is placed in a high-permeability region (inside the collapsed cave). The pressure that drives the fluids from the reservoir towards the well does not need to be high because the permeability is high. Figure 3.1.4-4 shows that both the collapsed cave case and the "no cave" case are limited to the minimum BHP of 180 bar. The higher FPR in the "no cave" case is directly derived from Darcy's equation (see equation 12). A lower permeability needs a higher pressure difference to maintain the same fluid rate $q$. A complete list of symbols is presented in Appendix 7.1.4.

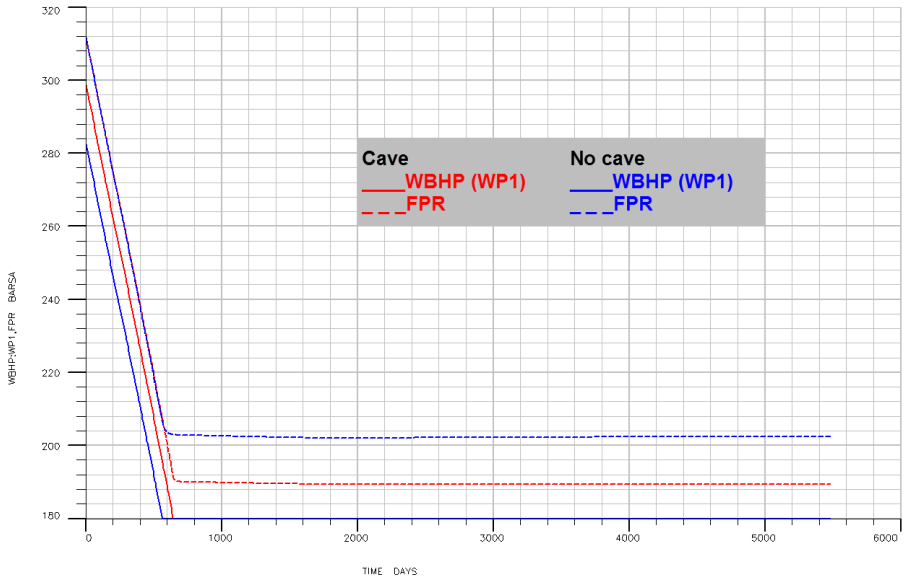


*Figure 3.1.4-4 This graph presents the Field Pressure (FPR) and Bottom Hole Pressure (BHP) for production well 1 (WP1) for high case with low injection rate.*

$$q = \frac{KA\Delta P}{\mu L} = \frac{KA(P_{FPR} - P_{BHP})}{\mu L} \quad (12)$$

The production curves for low case with low injection rate (see Figure 3.1.4-3) show a difference between the collapsed cave and the “no cave” case. When the permeability is low, the contrast between the high permeability inside of the cave and the low permeability in the background/host rock, is clearly reflected in the graphs. The ”no cave” case cannot produce with the same rates as the collapsed cave case, simply because flow properties are poor. As Figure 3.1.4-5 illustrates, the low case without a collapsed cave present is limited to by the Well Bottom Hole Pressure (WBHP) from the start of production. This limits oil production and therefore the field oil efficiency. The field pressure (FPR) however does not fall much because of the low production rate.

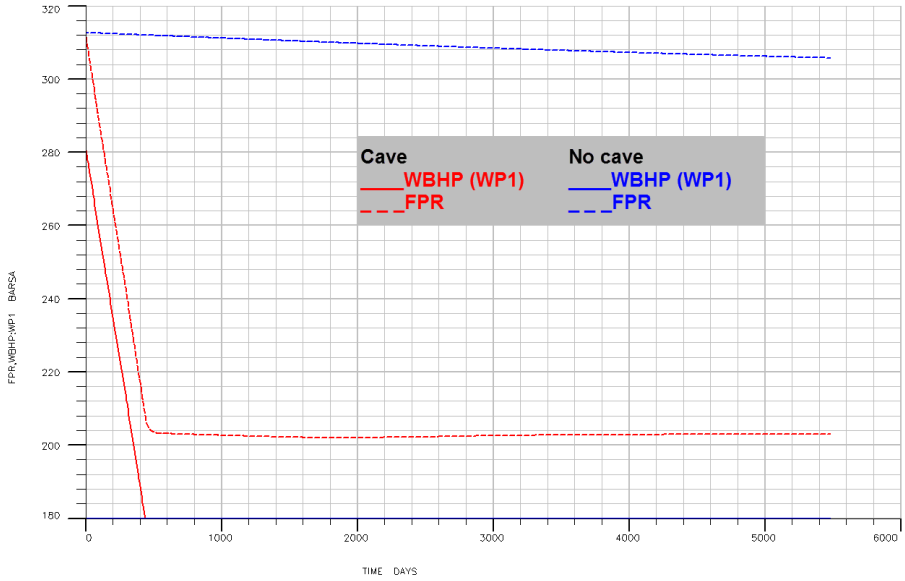


*Figure 3.1.4-5 This graph presents the Field Pressure (FPR) and Bottom Hole Pressure (BHP) for production well 1 (WP1) for low case with low injection rate.*

The following graphs (Figure 3.1.4-6 and Figure 3.1.4-7) show production curves for high- and low case with a high injection rate. The maximum injection rate is doubled from the previous cases, to keep reservoir pressure relatively stable.

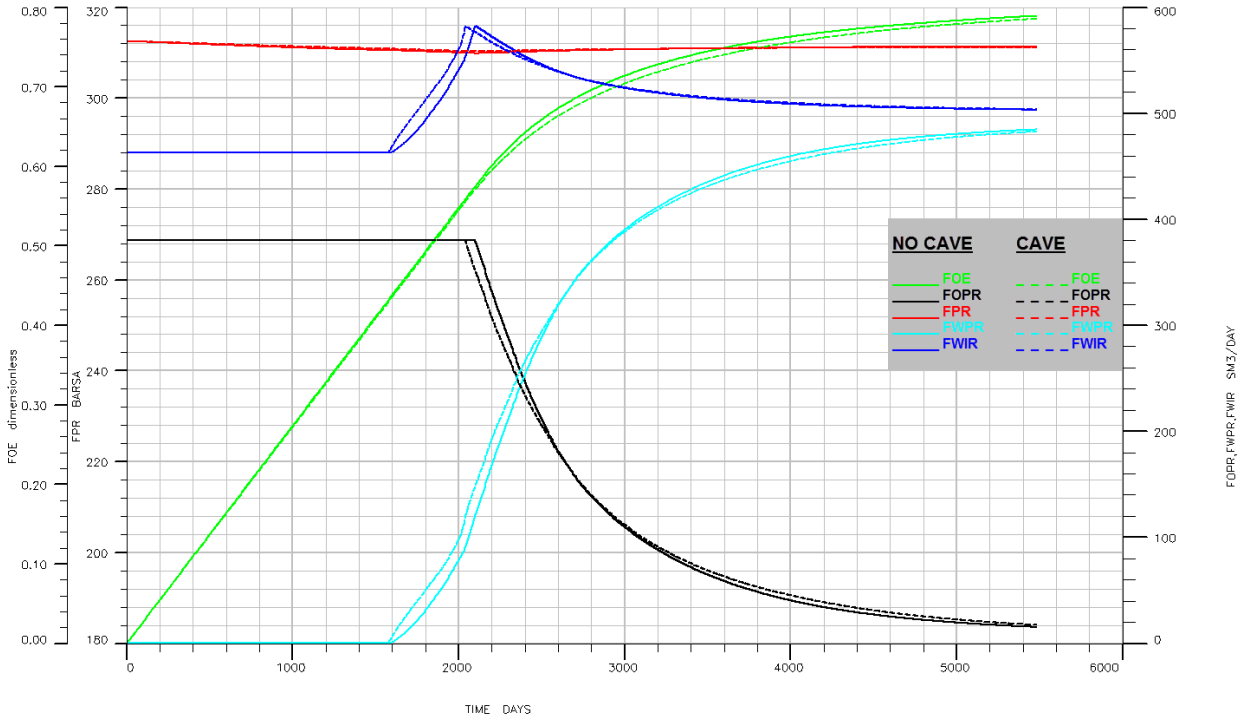


*Figure 3.1.4-6 This graph presents the FOE, FOPR, FPR, FWPR, and FWIR for high case with high injection rate.*

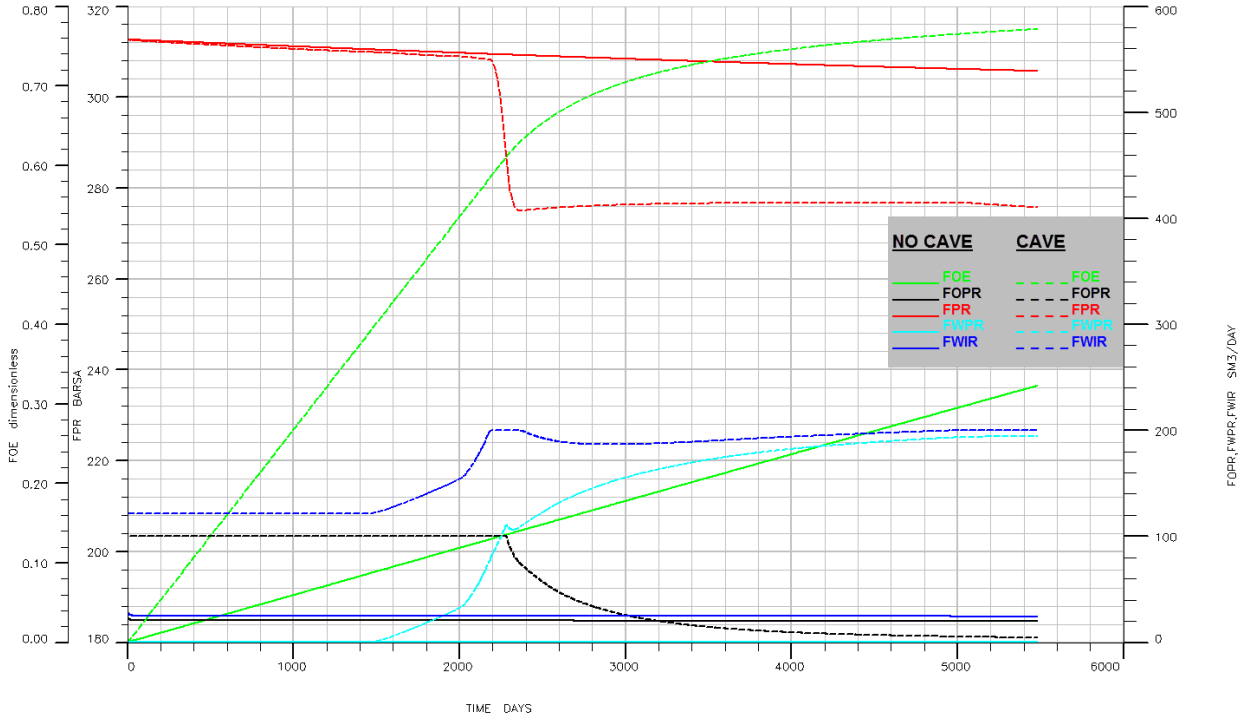


*Figure 3.1.4-7 This graph presents the FOE, FOPR, FPR, FWPR, and FWIR for low case with high injection rate.*

The reservoir pressure (FPR) is more or less constant for all cases apart from the low case with high maximum injection rate including a collapsed cave. This case is limited by the maximum injection rate, the graph (Figure 3.1.4-7) shows that after approximately 2200 days the FPR drops simultaneously as the FWIR peaks as 200 $Sm^3$/day. As for the FOPR, it is able to produce with a constant rate for all cases in the beginning, and decreasing when it is no longer possible to maintain the initial oil production rate.

Below, Table 3.1.4-1, shows a summary for time to water breakthrough (WBT) as well as Field Oil Efficiency (FOE) for the eight cases in Figure 3.1.4-1.

*Table 3.1.4-1 The table shows time to Water Break Through (WBT) as well as Field Oil Efficiency (FOE) for the eight cases in Figure 3.1.4-1. (H.inj) is written after the cases with high maximum water injection.*

| High/Low case | Radius collapsed cave | Time to WBT (days) | FOE 5 years (1825 days) | FOE 10 years (3650 days) | FOE 15 years (5475 days) |
|---|---|---|---|---|---|
| High | No cave | 1820 | 0.445 | 0.683 | 0.758 |
| High | 10 | 1820 | 0.444 | 0.670 | 0.747 |
| Low | No cave | no WBT | 0.108 | 0.216 | 0.322 |
| Low | 10 | 1900 | 0.413 | 0.627 | 0.693 |
| High (H.inj) | No cave | 1570 | 0.500 | 0.751 | 0.789 |
| High (H.inj) | 10 | 1550 | 0.497 | 0.743 | 0.786 |
| Low (H.inj) | No cave | no WBT | 0.108 | 0.216 | 0.322 |
| Low (H.inj) | 10 | 1445 | 0.489 | 0.736 | 0.771 |

From Table 3.1.4-1, it is clear that a higher injection rate will increase the field oil efficiency (FOE). The high case without a collapsed cave has a 3% higher FOE when the water injection rate is raised. While the high case with a collapsed cave has a 4% higher FOE when the water injection rate is raised. Furthermore, the low case with a collapsed cave has an 8% higher FOE when the water injection rate is raised, while the "no cave" case for low case has no change. This because the water injection is not raised as a result of the poor characteristics of this reservoir.

Figure 3.1.4-8 below presents a summary of FOPR, FWPR, and FWIR for high and low case with high injection rate.

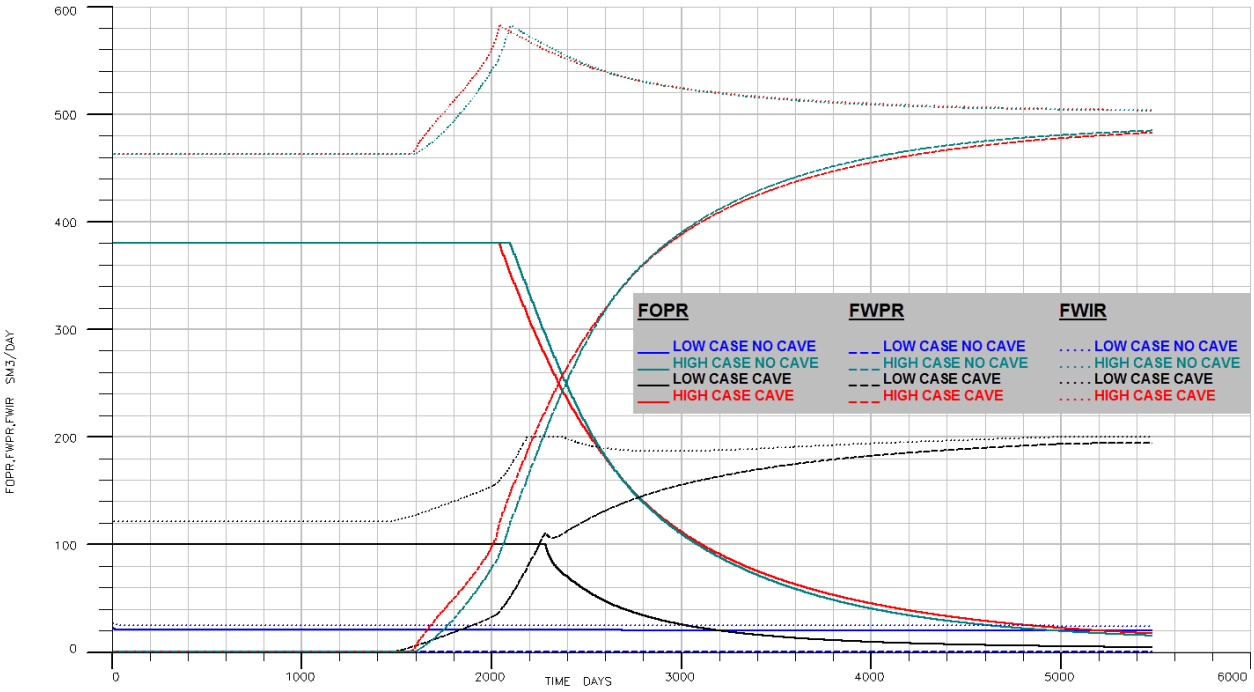


*Figure 3.1.4-8 This graph presents the summary of FOPR, FWPR, and FWIR for high and low case with high injection rate.*

It becomes obvious that for the high case, that the porosity and permeability increase introduced by adding a collapsed cave is not very noticeable. If the reservoir properties already are good, the improvement is not necessary to be able to produce the field. For low case however, the field oil efficiency (FOE) is raised from 33.2% to 77.1%, which means that the presence of a collapsed cave will more than double the FOE for the low case.

One consequence of setting a higher maximum injection rate is an increase in water production. See Figure 3.1.4-9 below for the water cut.

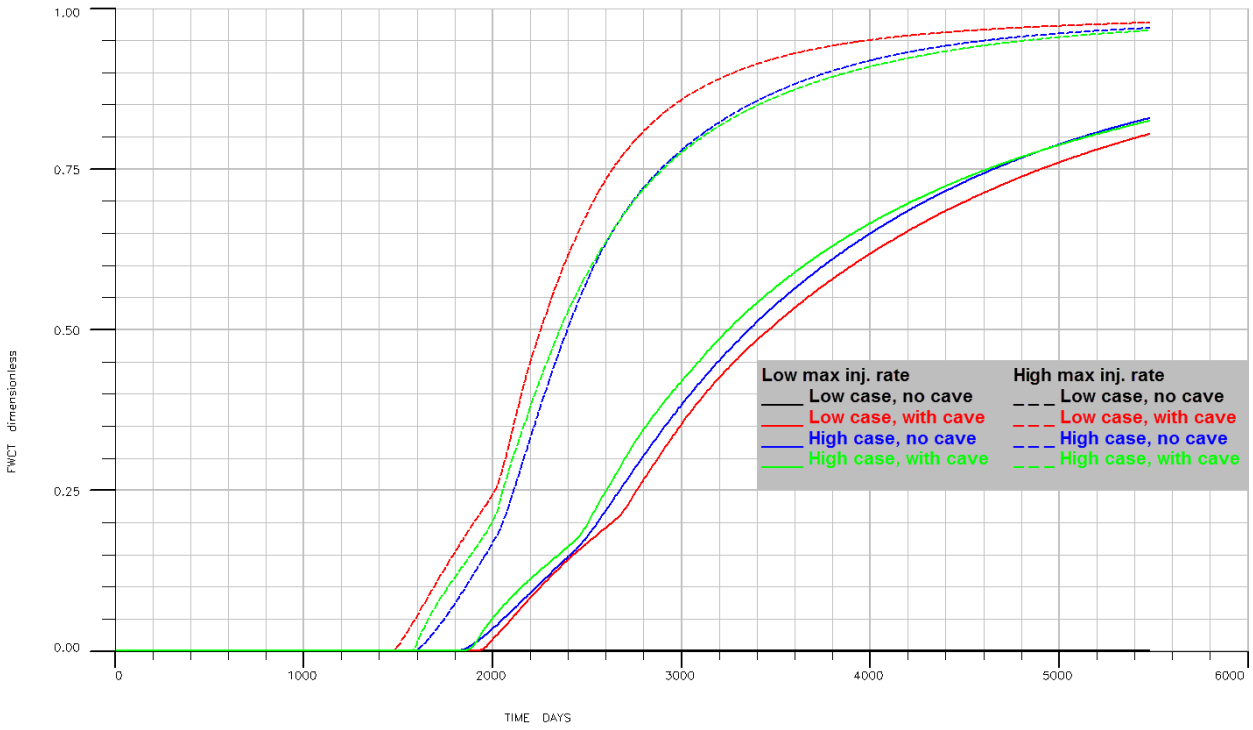


*Figure 3.1.4-9 This graph presents the FWCT (Field Water Cut) for the eight cases; high and low case with or without collapsed cave (R2 equal to 10 meters) and with high and low injection rate.*

As Figure 3.1.4-9 illustrates, the low case without a cave experiences no WBT (the FWCT graph is constant zero value). High water injection cases have a higher FWCT as a result of higher water production rate.

Some simulation graphs are presented in this chapter, and can be used as reference curves for future simulation of either synthetic- or real paleokarst reservoirs.

# 4 Conclusions

The thesis present a procedure for modeling paleokarst reservoirs in RMS. The workflow can be used for modeling paleokarst reservoir configurations deriving from any conceivable cave geometry. Paleocave systems of any imaginable geometry, as long as a skeleton line that represent this geometry is created.

Furthermore, the effect of the radius of the cave after collapse ($R_2$) is tested by comparing production curves derived from simulation of fluid flow in the paleokarst reservoir with Eclipse. The research shows that within the scope of tests carried out in this thesis, changing the collapse radiuses ($R_2$ equal to 10, 12 or 14 meters) will not affect the simulation results. As long as the volume of the cave before collapse is constant (as $R_1$ is constant equal to 5 meters), the increase of porosity (and thereby permeability) added to the background in each collapsed cave radius case is constant. In practice, this implies that the initial dimensions of the cave system appear to be relatively more important than how far the collapse of the cavity extends into the surrounding formation.

The main conclusion with respect to upscaling test performed here, is that a grid cell dimension of 4 or 8 meters provides a sufficiently detailed approximation of an the original reservoir model with 2 meters grid cell diameter. The simulated production curves indicate that results start to deviate from the initial fine-scale model when the grid cell dimension of the upscaled model exceed the collapsed cave diameter. For later studies, a grid cell diameter of 4 or 8 meters (for a reservoir model of the same size) is recommended. The amount of CPU time saved is substantial, which for practical purposes implies that more models and simulations can be performed in a shorter time.

Finally, this thesis presents several simulation result that can be used as reference curves for future simulation of either synthetic- or real paleokarst reservoirs.

# 5 Future work and limitations with this study

Future work within modeling and simulation of fluid flow in paleokarst reservoirs should focus on creating a set of realistic models, to create a "multiple case atlas" which can be used as a guideline for exploration and production of this type of reservoirs. Additional realistic models, brings the possibility to choose the best representation of the real case reservoir oil companies are working with. If the conditions governing karst morphology in a given reservoir formation can be constrained (e.g. climate, lithology, tectonics, sea-level change), this can be used to make assumptions about shape orientation and dimensions of karst forms including cave systems. Using the methods outlined in this thesis, a number of plausible reservoir models can be constructed and tested to add exploration and production work in these formations.

Better studies of outcrops and access to well data of paleokarst could contribute to reservoir models with better representing petrophysical properties, and thereby improve the models further.

Another interesting aspect opened up by this study, is that it offers the potential to carry out seismic forward modeling of paleokarst reservoir models. Comparison of seismic signatures from systematically generated paleokarst reservoir models with real-life seismic from known or suspected paleokarst reservoirs, could significantly enhance our ability to provide for optimized production from these complex features. The recognition of paleocave systems in seismic, could be vital information when it comes to both drilling, and reservoir prediction.

The green arrows in the chart below (a continuation of the mind map presented in the introduction, see Figure 1.1.1-1) sum up the future work, while the red arrows illustrates the structure of this thesis.

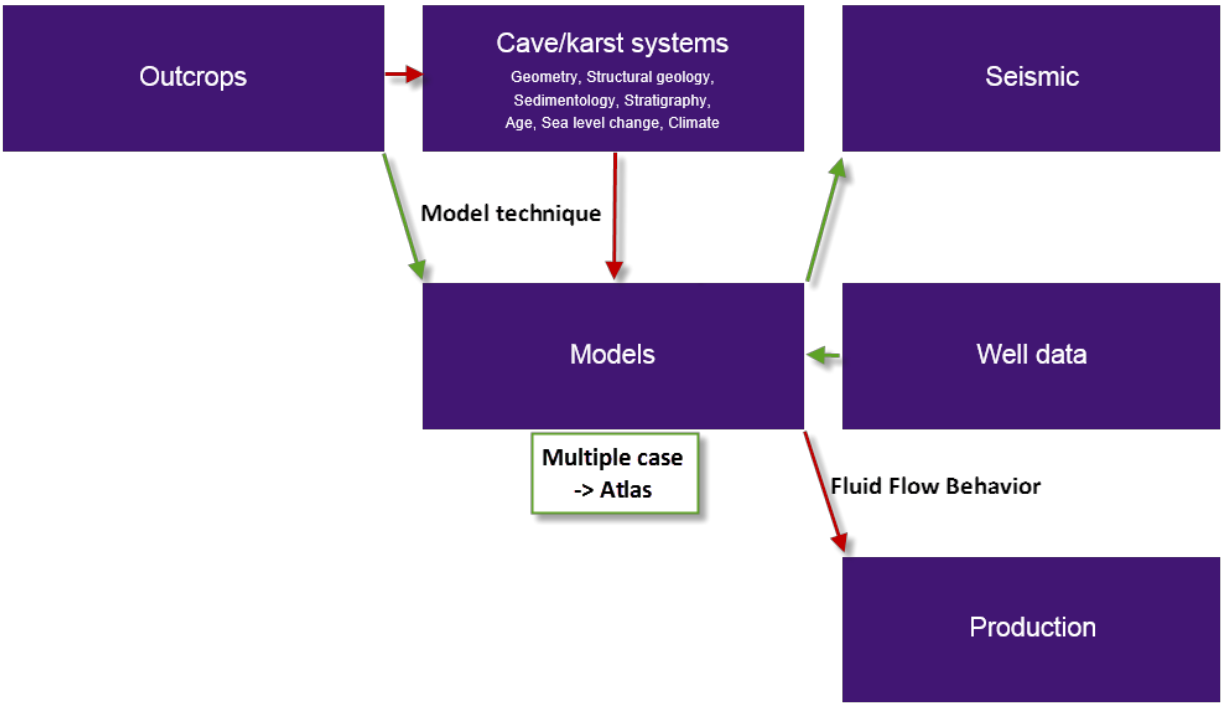


A number of shortcomings in this study originate from limitations imposed by the RMS-software. It is not possible to specify more than one radius of the original cave without performing a substantial amount of manual work, by dividing the cave into different segments and perform separate modeling of cave diameters before the individual segments merging into one. If for example a range of different radii (with weight parameter) could define the distance from a skeleton line, the geometry could be rendered more realistic. RMS has a tool that can make irregular intrusions, the disadvantage however, is that these irregular bodies not can be gridded (which of course is essential for creating a reservoir model). Pardo-Igúzquiza et al. (2011, 2012) and Collon-Drouaillet et al. (2012) have more realistic geometry in form of radius of the cave system. They use GoCad software for cave modeling. It would be interesting to investigate if their methods could be merged with the workflow outlined here.

Another limitation worth mentioning is the fact that the measuring of geometry of the Setergrotta Cave system is restricted by the cave diameter. It is not possible to crawl through tiny holes to measure all cave passages. In practice, this means that there is a lower cut-off diameter, and the length of the cave passages is underestimated. Handling this issue in a statistical manner should be possible, but this is outside the scope of the present study.

# 6 References

AFIFI, A. M. 2005. Ghawar: The Anatomy of the World's Largest Oil Field. *AAPG Distinguished Lecture, Search and Discovery Article,* 20026.

AL-AWADI, M., CLARK, W. J., MOORE, W. R., HERRON, M., ZHANG, T., ZHAO, W., HURLEY, N., KHO, D., MONTARON, B. & SADOONI, F. 2009. Dolomite: perspectives on a perplexing mineral. *Oilfield Review,* 21**,** 32-45.

BICKERT, T. 2009. Carbonate compensation depth. *Encyclopedia of Paleoclimatology and Ancient Environments*. Springer.

BING, Z., RONGCAI, Z., XUBEN, W., YUAN, L., WEI, L., HUAGUO, W. & ZHONGGUI, H. 2011. Paleokarst features and reservoir distribution in the Huanglong Formation of eastern Sichuan. *Petroleum Exploration and Development,* 38**,** 257-267.

BOGGS, S. 2012. *Principles of sedimentology and stratigraphy,* Upper Saddle River, N.J., Pearson Prentice Hall.

BROWN, A. 1997. Porosity variation in carbonates as a function of depth: Mississippian Madison Group, Williston Basin.

BURCHETTE, T. P. 2012. Carbonate rocks and petroleum reservoirs: a geological perspective from the industry. *Geological Society, London, Special Publications,* 370**,** 17-37.

CHOQUETTE, P. W. & JAMES, N. P. 1987. Diagenesis# 12. Diagenesis in Limestones-3. The deep burial environment. *Geoscience Canada,* 14.

CHOQUETTE, P. W. & PRAY, L. C. 1970. Geologic nomenclature and classification of porosity in sedimentary carbonates. *AAPG bulletin,* 54**,** 207-250.

COE, A. L. 2003. *The sedimentary record of sea-level change*, Cambridge University Press.

COLLON-DROUAILLET, P., HENRION, V. & PELLERIN, J. 2012. An algorithm for 3D simulation of branchwork karst networks using Horton parameters and *Geological Society, London, Special Publications,* 370**,** 295-306.

CRAIG, D. H. 1988. Caves and other features of Permian karst in San Andres dolomite, Yates field reservoir, west Texas. *Paleokarst*. Springer.

DALVA, A. 2012. Reservoir simulation of fluid flow in a reservoir with collapse breccia pipes and methods for spatial recognition of collapse breccia pipes in producing petroleum reservoirs.

DEMIRALIN, A. S. 1993. Karst breccias in the Madison Limestone (Mississippian), Garland Field, Wyoming.

DOORNHOF, D., KRISTIANSEN, T. G., NAGEL, N. B., PATTILLO, P. D. & SAYERS, C. 2006. Compaction and subsidence. *Oilfield Review,* 18**,** 50-68.

DOU, Q., SUN, Y., SULLIVAN, C. & GUO, H. 2011. Paleokarst system development in the San Andres Formation, Permian Basin, revealed by seismic characterization. *Journal of Applied Geophysics,* 75**,** 379-389.

DUNHAM, R. J. 1962. Classification of carbonate rocks according to depositional textures.

FEAZEL, C. 2010. Using Modern Cave Systems as Analogs for Paleokarst Reservoirs. AAPG.

FOLK, R. L. 1962. Spectral subdivision of limestone types.

FURNÉE, J. P. 2013. Karst and karstification. A view at solution and collapse breccias of the Minkinfjellet and Wordiekammen formations around Fortet and Waterfall Valley, Central Spitsbergen, Svalbard.

GISCHLER, E. 2011. Carbonate Environments. *In:* REITNER, J. & THIEL, V. (eds.) *Encyclopedia of Geobiology*. Springer Netherlands.

GOLDHAMMER, R. K. 1997. Compaction and decomposition algorithms for sedimentary carbonates.

HALBOUTY, M. T., MEYERHOFF, A. A., KING, R. E., DOTT SR, R. H., KLEMME, H. D. & SHABAD, T. 1970. World's giant oil and gas fields, geologic factors affecting their formation, and basin classification: Part I: Giant oil and gas fields.

HAMMES, U., F. J. LUCIA, AND C. KEARNS 1996. Reservoir heterogeneity in karst-related reservoirs: Lower Ordovician Ellenburger Group, west Texas. *E. L. Stoudt, ed., Precambrian–Devonian geology of the Franklin Mountains, west Texas—analogs for exploration and production in Ordovician and Silurian karsted reservoirs in the Permian basin: West Texas Geological Society, 1996 Annual Field Trip Guidebook, WTGS Publication 96-100***,** 99-115.

JAMES, N. P. & CHOQUETTE, P. W. 1984. Diagenesis 9. Limestones-the meteoric diagenetic environment. *Geoscience Canada,* 11.

JAMES, N. P. & CHOQUETTE, P. W. 1988. *Paleokarst*, Springer.

KANG, X., QIANG, J., FEI, T., LI, Y. & ZHANG, H. 2013. 1555826 Based on the Filling Evaluation of Carbonate Paleokarst Reservoir poroperm characteristics in Tahe Oilfield, Tarim Basin.

KERANS, C. 1988. Karst-controlled reservoir heterogeneity in Ellenburger Group carbonates of west Texas. *AAPG bulletin,* 72**,** 1160-1183.

LAURITZEN, S.-E., HESTANGEN, H., SKUTLABERG, S. & ØVREVIK, R. The Grønli-Seter cave research project, Rana, North Norway. Proceedings of the 14th International Congress of Speleology, Athen-Kalamos, 2005. 1-6.

LI, J., ZHANG, W., LUO, X. & HU, G. 2008. Paleokarst reservoirs and gas accumulation in the Jingbian field, Ordos Basin. *Marine and Petroleum Geology,* 25**,** 401-415.

LOMANDO, A. J. 1993. Casablanca field, Tarragona Basin, offshore Spain: a karsted carbonate reservoir.

LOUCKS, R. G. 1999. Paleocave carbonate reservoirs: origins, burial-depth modifications, spatial complexity, and reservoir implications. *AAPG bulletin,* 83**,** 1795-1834.

LOUCKS, R. G. 2007. A review of coalesced, collapsed-paleocave systems and associated suprastratal deformation. *Acta Carsologica,* 36**,** 121-132.

LOUCKS, R. G. & HANDFORD, C. R. 1992. Origin and recognition of fractures, breccias, and sediment fills in paleocave-reservoir networks. *M. P. Candelaria and C. L. Reed, eds., Paleokarst, karst related diagenesis and reservoir development: examples from Ordovician–Devonian age strata of west Texas and the midcontinent: Permian Basin Section, SEPM Publication 92-33***,** 31–44.

LOUCKS, R. G. & HANDFORD, C. R. 1996. Origin and recognition of fractures, breccias and sediment fills in paleocave-reservoir networks. *PUBLICATIONS-WEST TEXAS GEOLOGICAL SOCIETY***,** 207-220.

LUCIA, F. J. 1995. Lower Paleozoic cavern development, collapse, and dolomitization, Franklin Mountains, El Paso, Texas.

LUCIA, F. J. 2004. Origin and petrophysics of dolostone pore space. *Geological Society, London, Special Publications,* 235**,** 141-155.

LUCIA, F. J. 2007. *Carbonate Reservoir Characterization - An Integrated Approach,* New York, Springer.

LØNØY, A. 2006. Making sense of carbonate pore systems. *AAPG bulletin,* 90**,** 1381-1405.

MAZZULLO, S. & CHILINGARIAN, G. 1996. Hydrocarbon reservoirs in karsted carbonate rocks. *Developments in Petroleum Science,* 44**,** 797-865.
NORDEIDE, H. C. 2008. Spatial distribution and architecture of breccia pipes features at Wordiekammen, Billefjorden, Svalbard.
NORDLI, C. 2009. Fluid Flow in and around collapsed karst structures; breccia pipes, in Petroleum Reservoirs.
PALMER, A. N. 1991. Origin and morphology of limestone caves. *Geological Society of America Bulletin,* 103**,** 1-21.
PARDO-IGÚZQUIZA, E., DOWD, P. A., XU, C. & DURÁN-VALSERO, J. J. 2012. Stochastic simulation of karst conduit networks. *Advances in Water Resources,* 35**,** 141-150.
PARDO-IGUZQUIZA, E., DURÁN-VALSERO, J. J. & RODRÍGUEZ-GALIANO, V. 2011. Morphometric analysis of three-dimensional networks of karst conduits. *Geomorphology,* 132**,** 17-28.
PETTERSEN, Ø. 2006. Basics of Reservoir Simulation with the Eclipse Reservoir Simulator. *Bergen, Norway: University of Bergen, Department of Mathematics, Lecture Notes*.
ROXAR 2013a. Appendix K - Rescaling Theory — RMS 2013.0.
ROXAR 2013b. Horizon Mapping.
ROXAR 2013c. Upscaling Parameters — RMS 2013.0.
SALLER, A. 2014. *Carbonate Depositional Systems*, AAPG WEC 2014 - Lecture Notes.
SANDBERG, P. A. 1983. An oscillating trend in Phanerozoic non-skeletal carbonate mineralogy. *Nature,* 305**,** 19-22.
SARG, J. F. 2014. *Carbonate Seismic Sequence Stratigraphy - Application to Exploration*, AAPG WEC 2014 - Lecture Notes.
SCHLUMBERGER 2007. Carbonate Reservoirs - Meeting unique challenges to maximize recovery.
SCHLUMBERGER 2008. Brochure: Carbonate Advisor - Meeting unique challenges to maximize recovery.
SCHLUMBERGER 2013. Eclipse Reference Manual.
SCHLUMBERGER. 2014a. *Carbonate Reservoirs* [Online]. Available: http://www.slb.com/services/technical_challenges/carbonates.aspx.
SCHLUMBERGER. 2014b. *ECLIPSE Industry Reference Reservoir Simulator* [Online]. Available: http://www.software.slb.com/products/foundation/Pages/eclipse.aspx.
SCHMOKER, J. W. & HALLEY, R. B. 1982. Carbonate porosity versus depth: a predictable relation for south Florida. *AAPG Bulletin,* 66**,** 2561-2570.
SCHOLLE, P. & SCHOLLE, D. 2014. *Carbonate Reservoir Geology: Understanding Depositional and Diagnetic Factors Controlling Porosity*, AAPG WEC 2014 - Lecture Notes.
SCHOLLE, P. A. 1977. Chalk diagenesis and its relation to petroleum exploration: oil from chalks, a modern miracle? *AAPG Bulletin,* 61**,** 982-1009.
SCHOLLE, P. A. & ULMER-SCHOLLE, D. S. 2003. *A Color Guide to the Petrography of Carbonate Rocks: Grains, Textures, Porosity, Diagenesis, AAPG Memoir 77*, AAPG.
SETERGROTTA. 2015. *Setergrotta.no* [Online]. Available: http://www.setergrotta.no/ipub/pages/startside/mer_om_setergrotta.php.
TUCKER, M. E. 2011. *Sedimentary rocks in the field : a practical guide,* Chichester, West Sussex ; Hoboken, NJ, Wiley-Blackwell.
TUCKER, M. E., WRIGHT, V. P. & DICKSON, J. A. D. 1990. *Carbonate Sedimentology*, Wiley.

WHITE, E. L. & WHITE, W. B. 1969. Processes of cavern breakdown. *National Speleological Society Bulletin,* 31**,** 83-96.

XIAOQIANG, M., JIAGEN, H., YUMING, L. & BIN, Z. 2012. 3D Modeling of the Paleocave Reservoir in Tahe Oil Field, China. AAPG.

ØVREVIK, R. 2002. *Hydrologi og karstkorrosjon i Grønli-Seterakviferen, Mo i Rana*.

# 7 Appendix

## 7.1 Explanations

### 7.1.1 Grid model names (in RMS):

Grid model names start with “Grid2000”, specifying that the minimum depth of the skeleton line defining the center points of the cave before collapse starts at a depth of 2000 meters below mean sea level:

***Grid2000***

Then the grid model name defines the grid cell diameter [m]:

***2***, ***4***, ***8***, ***16***, ***32***

Further, the grid model name defines the radius of the collapsed cave [m]. If left blank “background” is added to the end of the grid model name, specifying that the model has no cave:

***10***, ***12***, ***14***, ***_***

Last the grid model name specifies if it is a high- or low case based on background porosity (Low case: Background Ø = 5%, High case: Background Ø = 20%):

***High*** or ***Low***

Example:

***Grid2000_4_10_low*** means the grid has minimum depth at 2000 meters below mean sea level, grid cell diameter of 4 meters, contains the collapsed cave with 10 meter radius, and low case with a background porosity of 5%.

### 7.1.2 Reservoir model names (in Eclipse):

Reservoir model names starts with the grid cell diameter [m]. If left blank means the standard grid cell diameter of 2 meter):

***_ , 4, 8, 16, 32***

Then the reservoir model name specifies if it is a high- or low case based on background porosity (Low case: Background Ø = 5%, High case: Background Ø = 20%):

***Highcase*** or ***Lowcase***

Further, the reservoir model name defines if there is a collapsed cave present:

***Cave*** or ***Nocave***

If there is a collapsed cave present, the radius is specified by "rc_XX" = Radius collapsed cave XX meters:

***Rc10***, ***rc12***, ***rc14***

Example:

***4_Lowcase_Cave_rc10*** means that the grid cell diameter is 4 meters, that it is low case with a background porosity of 5%, that there is a collapsed cave present and that the radius of the collapsed cave is 10 meters.

### 7.1.3 Explanations of self made keywords:

***SkeletonLines***

Polygon of analyzed path between center points of the Setergrotta Cave system.

***SkeletonLines2000***

To make the reservoir model more trustworthy and realistic, 1518 meters was added to the z-direction of the *SkeletonLines*, so that the depth range of the new *SkeletonLines2000* is 2000-2071 meters below mean sea level.

***BoundarySkeletonLines2000***

Boundary polygon based on *SkeletonLines2000*, but adjusted not to be totally fitted to the corner points.

***RefinedPoints_SkeletonLines2000***

Points based on *SkeletonLines2000*. The line segments were refined, by adding more points along the *SkeletonLines* in addition to the original center points from the Setergrotta Cave dataset. These refined points are used as input data for geometric modeling.

***Geometric_5***

A geometric model based on *RefinedPoints_SkeletonLines2000*. Radius from *RefinedPoints_SkeletonLines2000* was chosen to be 5 meters.

| Elevated refined points as input for geometric modeling | Geometric model | Elevation [m] from original *RefinedPoints_SkeletonLines2000* |
|---|---|---|
| *RefinedPoints_SkeletonLines2000_+3* | *Geometric_2* | 3 |
| *RefinedPoints_SkeletonLines2000_+1* | *Geometric_4* | 1 |
| *RefinedPoints_SkeletonLines2000_-1* | *Geometric_6* | -1 |
| *RefinedPoints_SkeletonLines2000_-3* | *Geometric_8* | -3 |
| *RefinedPoints_SkeletonLines2000_-5* | *Geometric_10* | -5 |
| *RefinedPoints_SkeletonLines2000_-7* | *Geometric_12* | -7 |
| *RefinedPoints_SkeletonLines2000_-9* | *Geometric_14* | -9 |

***Well placement in Eclipse:***

***WP1*** (Well Producer 1), ***WI1*** and ***WI2*** (Well Injector 1 and 2)

### 7.1.4 List of symbols

| | | |
|---|---|---|
| $\emptyset$ | = | Porosity [decimal fraction] (% if specified) |
| $K$ | = | Permeability [mD] |
| $A_n$ | = | Area of circle sector $n$ [$m^2$] |
| $\emptyset_n$ | = | Porosity of circle sector $n$ [decimal fraction] |
| $Kn$ | = | Permeability of circle sector $n$ [mD] |
| $rn$ | = | Radius of circle sector $n$ [m] |
| $A_t$ | = | Area of total circle [$m^2$] |
| $\emptyset_t$ | = | Porosity of total circle [decimal fraction] |
| $R_1$ | = | Radius cave [m] |
| $R_2$ | = | Radius collapsed cave [m] |
| $A_1$ | = | Area cave [$m^2$] |
| $A_2$ | = | Area collapsed cave [$m^2$] |
| $P_A$ | = | Value (arithmetic average) |
| $P_G$ | = | Value (geometric average) |
| $Pn$ | = | Value fraction $n$ |
| $Wn$ | = | Weight fraction $n$ |
| $q$ | = | Fluid flow rate through medium [$Sm^3$/sec] |
| $A$ | = | Area [$m^2$] |
| $\Delta P$ | = | Pressure difference [bar], ($P_{FPR} - P_{BHP}$), (Field Pressure – Bottom Hole Pressure) |
| $\mu$ | = | Viscosity [cP] |
| $L$ | = | Length [m] |

### 7.1.5 Well placement in Eclipse

*Table 7.1.5-1 Well completion data for all grid cell diameter cases (2, 4, 8, 16, 32 meter in diameter). WP1 (Well Producer 1), WI1 and WI2 (Well Injector 1 and 2)*

| Grid cell diameter | Well name | Ic | Jc | K_top | K_btm |
|---|---|---|---|---|---|
| 2 | *WP1* | 117 | 142 | 16 | 29 |
| 2 | *WI1* | 233 | 22 | 15 | 25 |
| 2 | *WI2* | 27 | 261 | 14 | 24 |
| 4 | *WP1* | 59 | 72 | 9 | 15 |
| 4 | *WI1* | 117 | 12 | 8 | 13 |
| 4 | *WI2* | 14 | 131 | 8 | 13 |
| 8 | *WP1* | 30 | 36 | 5 | 7 |
| 8 | *WI1* | 58 | 6 | 5 | 7 |
| 8 | *WI2* | 7 | 66 | 5 | 7 |
| 16 | *WP1* | 20 | 27 | 2 | 3 |
| 16 | *WI1* | 35 | 12 | 2 | 3 |
| 16 | *WI2* | 9 | 42 | 2 | 3 |
| 32 | *WP1* | 8 | 9 | 1 | 1 |
| 32 | *WI1* | 15 | 2 | 1 | 1 |
| 32 | *WI2* | 2 | 16 | 1 | 1 |

## 7.2 Porosity values

From the figures below, it follows that the porosity in carbonate rocks varies between 5-20% on 2000 meter depth. References used are: (Brown, 1997, Goldhammer, 1997, Schmoker and Halley, 1982)

(Goldhammer, 1997): Porosity 20% at 2000 meters

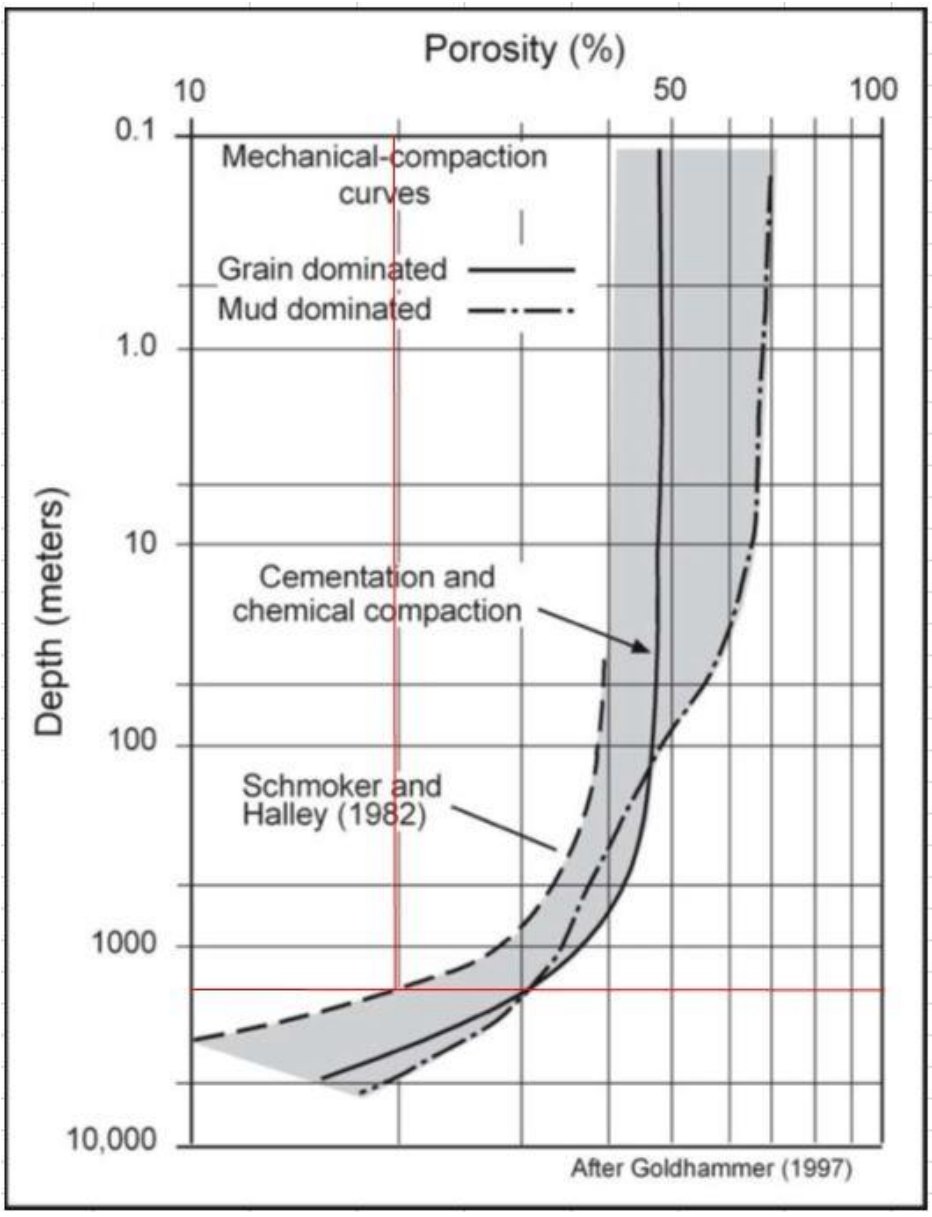

(Schmoker and Halley, 1982): Porosity 18% at 2000 meters

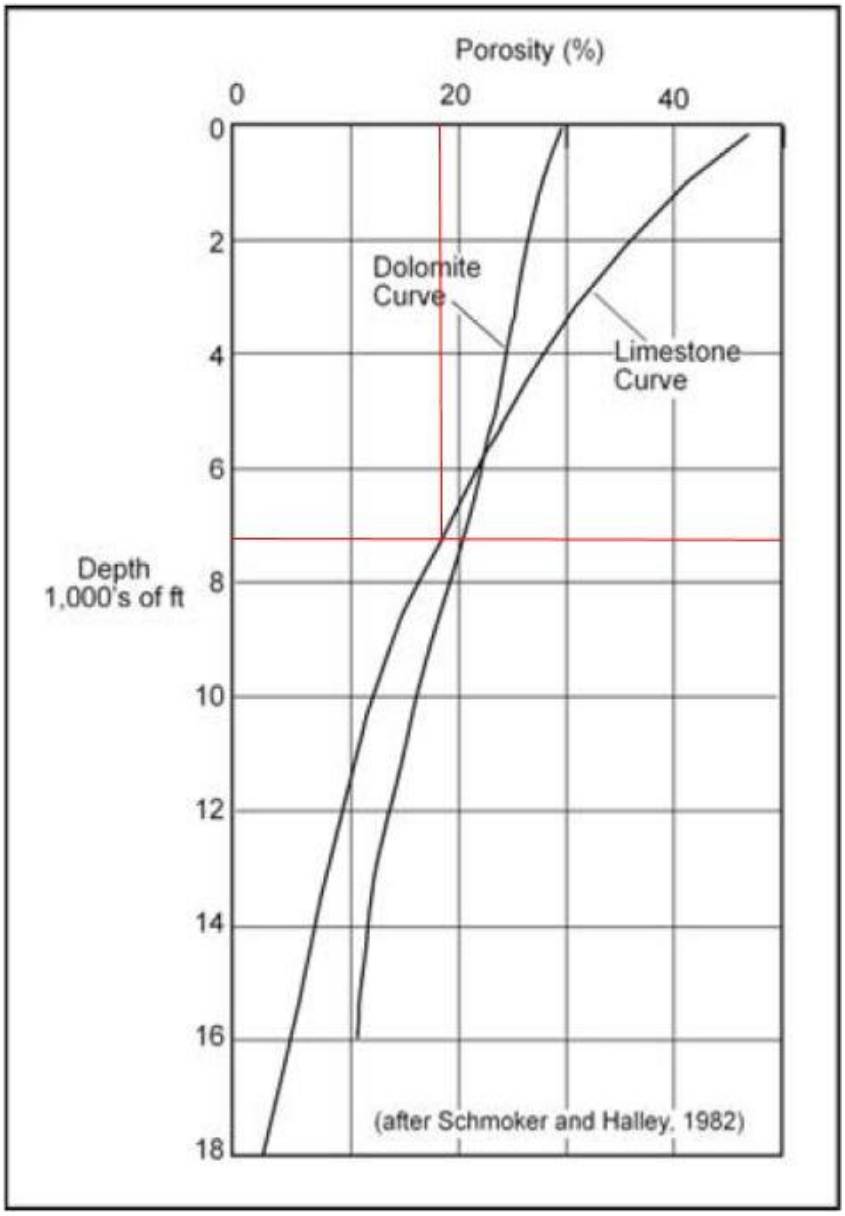

(Brown, 1997): Porosity 5% at 2000 meters

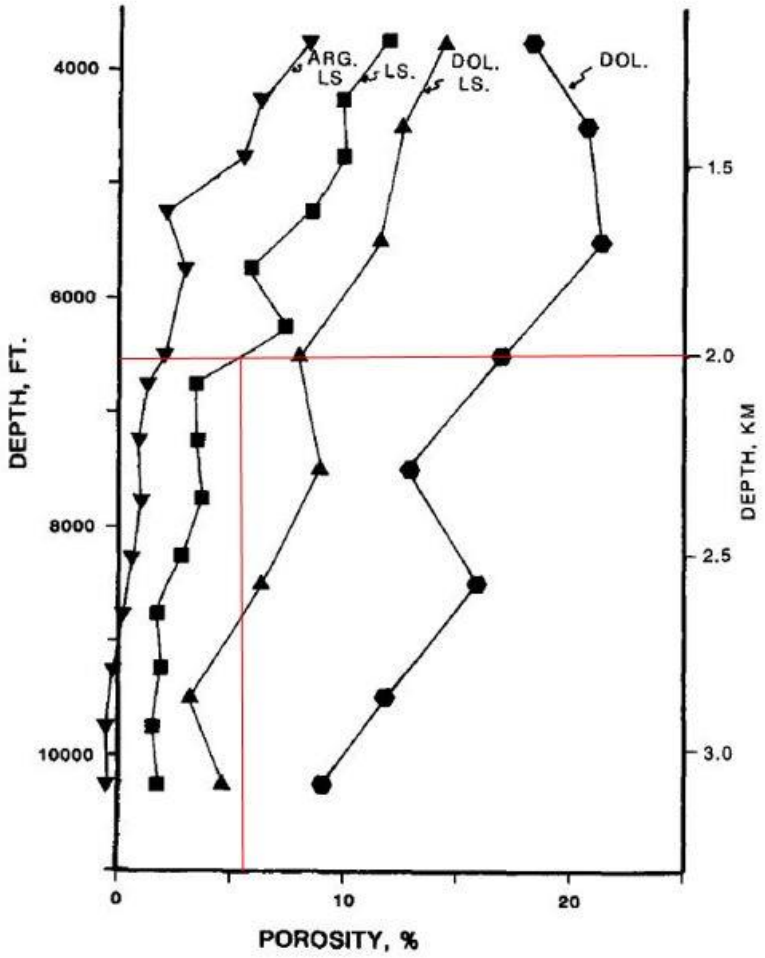


**Figure 3. Mean porosity of carbonate lithologies as a function of present-day burial depth. Symbols represent average depth and average porosity for that depth and lithology. ARG. LS. = argillaceous limestone; LS. = clean limestone; DOL. LS. = dolomitic limestone; DOL. = dolomite.**

(Brown, 1997): Porosity 5% at 2000 meters



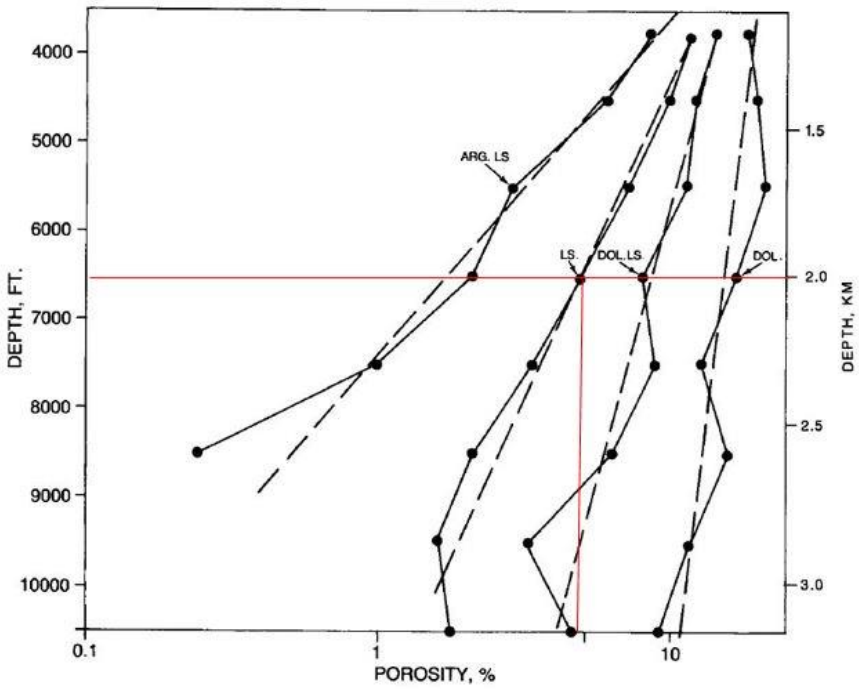


**Figure 4. Porosity trends on a semilogarithmic plot. The porosity loss plots close to a straight line in all of the lithologies, indicating that the porosity loss functions are approximately exponential. Low-porosity averages have a large scatter on semilogarithmic plots due to the inaccuracy of log-determined porosity at low values. ARG. LS. = argillacious limestone; LS. = clean limestone; DOL. LS. = dolomitic limestone; DOL. = dolomite.**

(Brown, 1997): Porosity 5% at 2000 meters

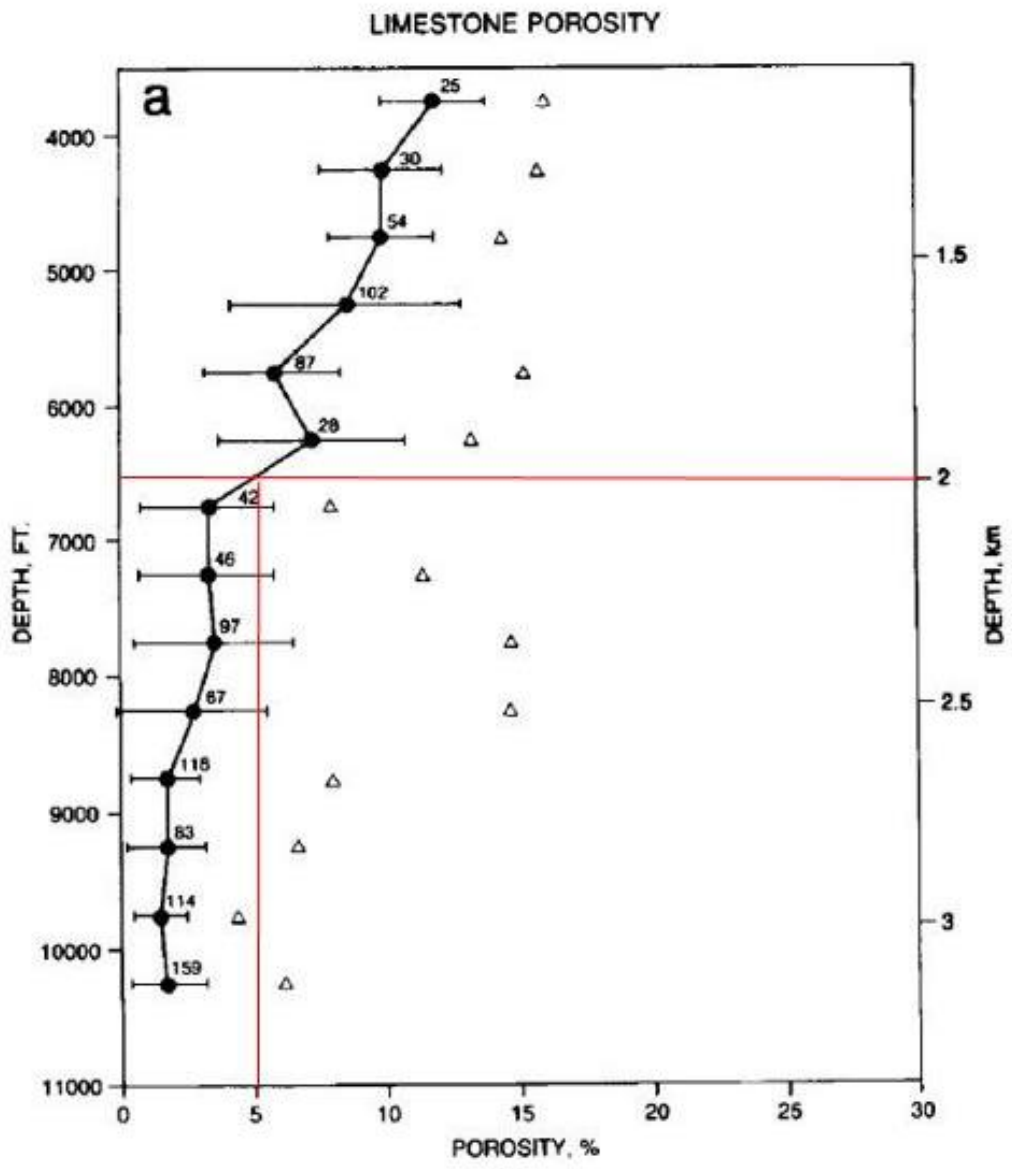

(Brown, 1997): Porosity 7-30% at 2000 meters

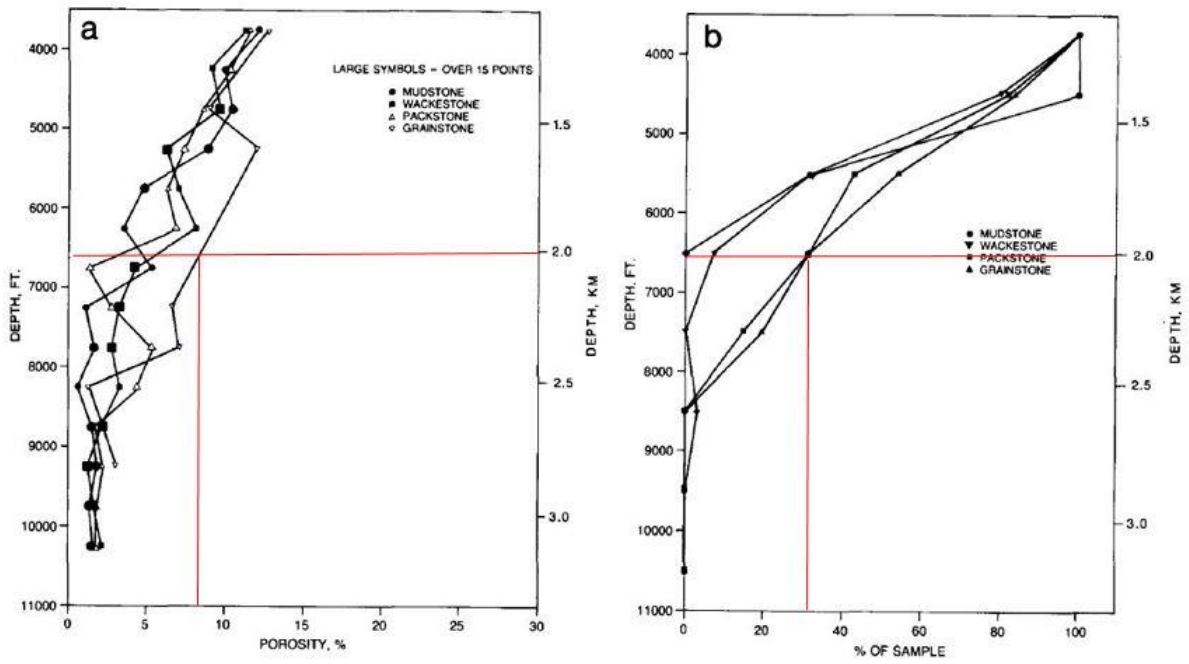


**Figure 7. Porosity of limestone fabrics. (a) Mean porosity of fabrics in depth intervals. There is no consistent ranking of the mudstone, wackestone, or packstone porosities from depth interval to depth interval. The grainstone samples are too small to be statistically distinguished from the packstones at the same depth given the large standard deviations of the porosity means. (b) Percentage of high-porosity samples ($\phi$ >8%) in carbonate fabrics from different depth intervals. Between 7.5 and 2.5 km, (500–8500 ft), the framework-supported carbonates have a significantly higher percentage of samples with porosities >8%. Below 2.5 km (8500 ft), all carbonates have low percentages of high-porosity samples**

(Brown, 1997): Porosity 5% at 2000 meters

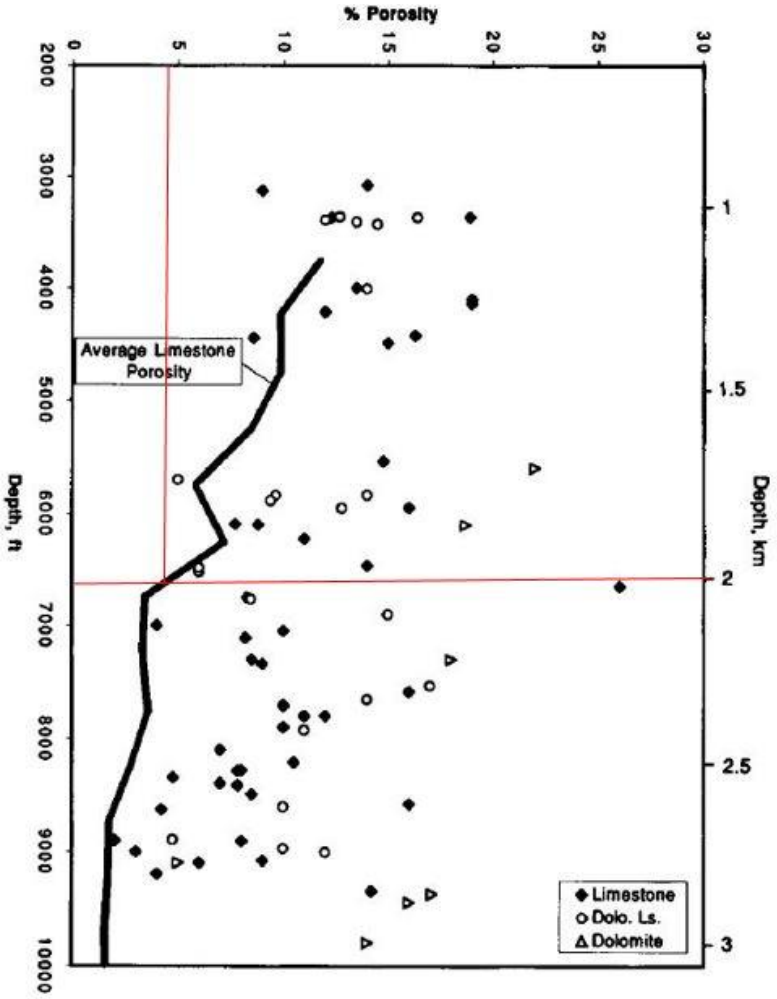


**Figure 10. Comparison of average limestone porosity trend developed here (solid line) with reservoir porosity of Madison Group fields of different reservoir mineralogy. Some fields with limestone may be dolomitic limestone or dolomite.**

(Brown, 1997): Porosity 5-20% at 2000 meters

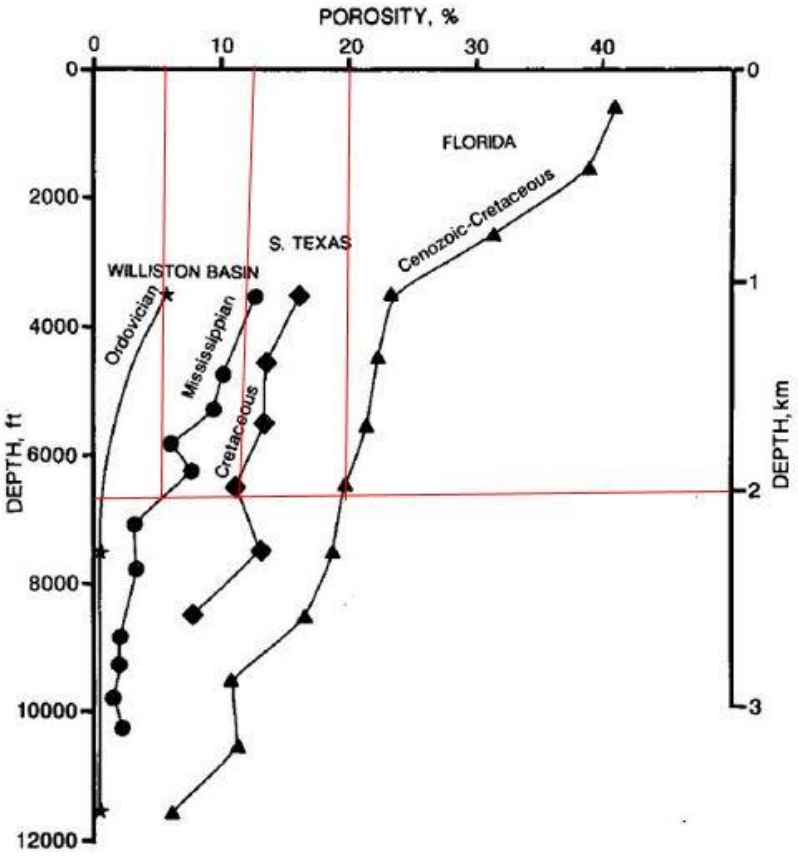


**Figure 13. Limestone porosity trend compared to other quantitative porosity trends for shelf limestones. Florida data from Schmoker (1984). Texas Cretaceous data are unpublished core analysis trends collected by R.G. Loucks (1985, personal communication). Ordovician data are average wireline-log limestone porosity from three wells penetrating the Red River Formation, collected as part of this study.**

## 7.3 Example of .data-file in Eclipse

```
NOECHO
-- ================================================================================================
--
-- Lowcase_cave_rc10
--
-- Exported by user jonfor from RMS2013 at 2015-03-17 11:33:41
--
-- ================================================================================================
-- ================================================================================================
RUNSPEC
-- ================================================================================================
TITLE
 Lowcase_cave_rc10
-- ------------------------------------------------------------------------------------------------
-- Grid dimensions
-- ------------------------------------------------------------------------------------------------
DIMENS
--  NX          NY     NZ
  261           279    35  /
-- ------------------------------------------------------------------------------------------------
-- Simulation start date
-- ------------------------------------------------------------------------------------------------
START
 1 'JAN' 2014  /
-- ------------------------------------------------------------------------------------------------
-- Unit system
-- ------------------------------------------------------------------------------------------------
METRIC
-- ------------------------------------------------------------------------------------------------
-- Phases and components
-- ------------------------------------------------------------------------------------------------
OIL
WATER
```

```
-- ------------------------------------------------------------------------------------------------
-- Program dimensions
-- ------------------------------------------------------------------------------------------------
--  Equilibration dimensions
EQLDIMS
-- NTEQUL   NDPRVD          NDRXVD
      1          100               20          /

-- Linear solver stack size. NSTACK is set equal to LITMAX if enough memory on computer. See keyword under “tuning parameters” below.
NSTACK
100             /

-- Number of iterations to update well targets (got a warning that said that I had too increase the value from 3)
NUPCOL
10              /

-- Table dimensions
TABDIMS
--              NTSFUN          NTPVT    NSSFUN  NPPVT    NTFIP    NRPVT
                1               1        40      30       30       30          /

-- Well dimensions
WELLDIMS
--              NWMAXZ          NCWMAX           NGMAXZ           NWGMAX
                5               20               5                5           /

-- Fault dimensions
FAULTDIM
--              MFSEGS
                0       /
-- ------------------------------------------------------------------------------------------------
-- Path names
-- ------------------------------------------------------------------------------------------------
PATHS
  'MAIN' 'C:\Users\jonfor\Dropbox\UIB\Master\Setergrotta_E\Lowcase_cave_rc10'  /
/
```

```
-- ----------------------------------------------------------------------------------------------
-- Options
-- ----------------------------------------------------------------------------------------------
--                                                Data checking only
--NOSIM
--                                                Input/output options
-- UNIFIN     -- Unified input files
UNIFOUT    -- Unified output files
--                                                Grid options
GRIDOPTS
 YES /


-- ==============================================================================================
GRID
-- ==============================================================================================
-- ----------------------------------------------------------------------------------------------
-- Output control
-- ----------------------------------------------------------------------------------------------
--                                                  Grid file export
GRIDFILE
-- GRID   EGRID
  0      1  /


--                                                Init file export
INIT


RPTGRID
-- ALLNNC
-- DEPTH
-- DX
-- DY
-- DZ
-- FAULTS
-- PORO
-- PORV
-- NTG
-- PERMX
-- PERMY
```

```
-- PERMZ
-- TRANX
-- TRANY
-- TRANZ
/
-- ------------------------------------------------------------------------------------------
-- Grid definition
-- ------------------------------------------------------------------------------------------
MAPAXES
  269.549   69.087
  269.549  719.138
  682.200  719.138
/

MAPUNITS
 METRES /

GRIDUNIT
 METRES /

GDORIENT
INC INC INC DOWN LEFT /

INCLUDE
 '$MAIN\Lowcase_cave_rc10.coord.inc'
/

INCLUDE
 '$MAIN\Lowcase_cave_rc10.zcorn.inc'
/

INCLUDE
 '$MAIN\Lowcase_cave_rc10.actnum.inc'
/
```

```
-- ------------------------------------------------------------------------------------------
-- Petrophysical properties
-- ------------------------------------------------------------------------------------------
--                                                 Porosity
INCLUDE
  '$MAIN\Lowcase_cave_rc10.poro.inc'
/
--                                                 Net-to-gross
INCLUDE
  '$MAIN\Lowcase_cave_rc10.ntg.inc'
/
--                                                 X Permeability
INCLUDE
  '$MAIN\Lowcase_cave_rc10.permx.inc'
/
--                                                 Y Permeability
INCLUDE
  '$MAIN\Lowcase_cave_rc10.permy.inc'
/
--                                                 Z Permeability
INCLUDE
  '$MAIN\Lowcase_cave_rc10.permz.inc'
/
```

```
-- ================================================================================================
PROPS
-- ================================================================================================
-- ------------------------------------------------------------------------------------------------
-- Output control
-- ------------------------------------------------------------------------------------------------
RPTPROPS
-- PVTO
-- PVDG or PVTG
-- PVTW
-- SGFN
-- SOFN
-- SWFN
-- SGL
-- SGU
-- SGCR
-- SOGCR
-- SOWCR
-- SWL
-- SWU
-- SWCR
-- PCG
-- PCW
-- ROCK
/
```

```
-- ------------------------------------------------------------------------------------------

-- Fluid data

-- ------------------------------------------------------------------------------------------

-- Two-phase (water-oil) relative permeability curves.

-- Relativ permeability for water and oil, and capillary pressure as a function of water saturation.

-- Sw – Water saturation, Krw – Relative permeability for water, Kro – Relative permeability for oil, Pcow – Capillary pressure

SWOF

--          Sw          Krw          Kro          Pcow
            0.200       0.000        0.850        0
            0.250       0.006        0.727        0
            0.300       0.013        0.613        0
            0.350       0.022        0.509        0
            0.400       0.032        0.414        0
            0.450       0.043        0.330        0
            0.500       0.057        0.255        0
            0.550       0.071        0.189        0
            0.600       0.087        0.133        0
            0.650       0.105        0.087        0
            0.700       0.124        0.051        0
            0.750       0.144        0.024        0
            0.800       0.167        0.007        0
            0.850       0.190        0.000        0
            0.900       0.300        0.000        0
            1.000       1.000        0.000        0          /


-- PVT-data for water

-- Pref – Reference pressure for rest of data, Bw – Volume formation factor for water, Cw – Water compressibility, ViscW – Water viscosity,

-- Cv – Viscobility

PVTW

--          Pref    Bw      Cw              ViscW     Cv
            308.2   1.024   0.0000464 0.42  1*        /
```

```
-- PVT-data for dead oil (black oil)
-- P(bar) – Pressure in Bar, Bo – Volume formation factor for oil, ViscO – Oil viscosity
PVDO
--          P(bar)      Bo        ViscO
            227.00      1.2600    1.042
            253.40      1.2555    1.072
            281.60      1.2507    1.096
            311.10      1.2463    1.118
            343.80      1.2417    1.151
            373.50      1.2377    1.174
            395.50      1.2356    1.200     /

-- Rock compressibility (linear)
-- Pref – Reference pressure for rest of data, Cr – Rock compressibility
ROCK
--          Pref    Cr
            1       5.60E-05  /

-- Surface densities [kg/Sm3]
DENSITY
--          oil     Water     Gas
            833     1038      0.66      /

-- Oil is always above bubble-point-pressure, i.e. dead oil, no free gas => Rs is constant
-- Rs – Dissolved gas concentration
RSCONST
--          Rs                Bubble-point-pressure
            100               180       /
```

```
-- ================================================================================================
REGIONS
-- ================================================================================================
-- ------------------------------------------------------------------------------------------------
-- Output control
-- ------------------------------------------------------------------------------------------------
RPTREGS
-- PVTNUM
-- SATNUM
-- EQLNUM
-- FIPNUM
/
-- ------------------------------------------------------------------------------------------------
-- Region grid arrays
-- ------------------------------------------------------------------------------------------------
--                                                 Fluid data regions
INCLUDE
  '$MAIN\Lowcase_cave_rc10.pvtnum.inc'
/
--                                                 Saturation data regions
INCLUDE
  '$MAIN\Lowcase_cave_rc10.satnum.inc'
/
--                                                 Equilibrium data regions
INCLUDE
  '$MAIN\Lowcase_cave_rc10.eqlnum.inc'
/
--                                                 Fluid-in-place data regions
INCLUDE
  '$MAIN\Lowcase_cave_rc10.fipnum.inc'
/
```

```
-- ================================================================================================
SOLUTION
-- ================================================================================================
-- ------------------------------------------------------------------------------------------------
-- Output control
-- ------------------------------------------------------------------------------------------------
RPTSOL
  'RESTART = 2'                 -- Initial restart kept
  'FIP=1'                       -- Fluid in place for whole field
-- DENG
-- DENO
-- DENS
-- DENW
-- EQUIL
-- FIPRESV
-- FLOGAS
-- FLOOIL
-- FLOWAT
-- KRG
-- KRO
-- KRW
-- PVDPH
-- RPORV
/
-- ------------------------------------------------------------------------------------------------
-- Equilibration data
-- ------------------------------------------------------------------------------------------------
-- Equilibration data
-- Datum – Datum depth, Pdatum – Pressure at the datum depth, OWC – Oil water contact (defined below the reservoir to get it completely
-- oil-filled, with no mobile water present in the reservoir), PCOWC – Capillary pressure at the contact, GOC – Gas oil contact (defined above
-- the reservoir to avoid including gas in model), PCGOC – Gas-oil capillary pressure at the gas-oil contact (default 0), TRSVD – Integer
-- selecting the type of initialization for live black oil (default 0), TRVVD – Integer selecting the type of initialization for black oil runs with wet
-- gas (default 0)
EQUIL
--              Datum           Pdatum    OWC       PCOWC   GOC       PCGOC   TRSVD   TRVVD   /
                1859.02         300       2096.89   0       1859.02   0       0       0       /
```

```
-- ================================================================================================

SUMMARY

-- ================================================================================================

ALL

-- View in Excel

EXCEL

-- Field Pressure Rate

FPR

-- Field Oil Production Rate

FOPR

-- Field Water Production Rate

FWPR

-- Field Gas Production Rate

FGPR

-- Field Oil Production Total

FOPT

-- Field Water Production Total

FWPT

-- Field Gas Production Total

FGPT

-- Field Oil Efficiency

FOE


-- To compare run times

-- Time step length

TIMESTEP

-- Number of Newton iterations for each time step

NEWTON

-- Current CPU usage in seconds

TCPU

-- CPU time per time step in seconds

TCPUTS

-- CPU time per day

TCPUDAY

-- Average number of linear iterations per Newton iteration, for each time step

NLINEARS
```

```
-- ================================================================================================

SCHEDULE

-- ================================================================================================

-- Define frequency for writing of restart files (every 1 month)

RPTRST

BASIC=5     NORST=1         FREQ=1   /

-- Well specifications

WELSPECS

--          Wname           Gname     Iwh     Jwh     Z(bhp)     PrefPhase  2*        ShutIn     XFlowFlag

--          1*              DensCalc  FIPnr   /

            WP1             G                 117     142        1*                   OIL                /

            WI1             G                 233     22         1*                   WAT                /

            WI2             G                 27      261        1*                   WAT                /

            /

-- Completion data

COMPDAT

--          Wnm*            Ic        Jc      K_top   K_btm      Open/Shut SatTblNbr tfac     Rh(diam)   Kh

--          Skin            dfac      penDir  r0      /

            WP1             117       142     16      29         O         1*        1*       0.35       1*

            0               1*        Z       1*      /

            WI1             233       22      15      25         O         1*        1*       0.35       1*

            0               1*        Z       1*      /

            WI2             27        261     14      24         O         1*        1*       0.35       1*

            0               1*        Z       1*      /

            /

-- Production specification. Specify a rate that ideally would drain the whole reservoir in 10 years.

-- 373582 Sm3 oil in place / 10 years / 365 days = 100 Sm3/day

WCONPROD

--          Wnm*  Open/ShutFlag  Ctrlmode  Orat    Wrat    Grat    Lrat    Resv)   BHPmin  THPmin  VFP-data

            WP1   OPEN           ORAT      100     1*      1*      300     1*      180     1*      1*      /

            /
```

```
-- Injection data
WCONINJE
--          Wnm*  InjFluid  Open/Shut CtrlMode  Rate      Resv      BHP       THP       1*        /
            WI1   WATER     OPEN      RATE      50        1*        500       1*        1*        /
            WI2   WATER     OPEN      RATE      50        1*        500       1*        1*        /
            /
GCONINJE
--          Group  Phase     CtrlMode  RateTrg   RvolTrg   ReinjTrg  VoidReplFrac      /
            FIELD  WATER     VREP      1*        1*        1*        0.9999            /
            /
-- ------------------------------------------------------------------------------------------
-- Output control
-- ------------------------------------------------------------------------------------------
RPTSCHED
-- 'RESTART=2'      -- All restarts kept
-- 'FIP=1'          -- Fluid in place for whole field
-- PRES
-- SOIL
-- SWAT
-- RS
-- RV
-- WELLS
-- SUMMARY
-- CPU
-- NEWTON
/
-- ------------------------------------------------------------------------------------------
-- Tuning parameters
-- ------------------------------------------------------------------------------------------
-- LITMAX specifies the maximum number of linear iterations in a Newton iteration. To avoid the calculations to run circles, a high enough
-- NSTACK has to be set. Usual these two are set equal.
TUNING
--          TSINIT        TSMAXZ        TSMINZ    TSMCHP    TSFMAX    TSFMIN    TSFCNV    TFDIFF    /
            0.1           5             0.1       1*        1*        1*        1*        1*        /
--          TRGTTE        TRGCNV        TRGMBE    TRGLCV    XXXTTE    XXXMBE    XXXLCV    XXXWFL    /
            1*            1*            1*        1*        1*        1*        1*        1*        /
--          NEWTMX        NEWTMN        LITMAX    LITMIN    MXWSIT    MXWPIT    DDPLIM    DDSLIM    /
            40            1             100       1         1*        1*        1*        1*        /
```

```
-- ------------------------------------------------------------------------------------------------

-- Time control

-- ------------------------------------------------------------------------------------------------

-- List of report dates  (15 years from production start 1. Jan 2014).

DATES

1     FEB  2014  /    --  1. YEAR

1     MAR  2014  /    --  1. YEAR

1     APR  2014  /    --  1. YEAR

1     MAY  2014  /    --  1. YEAR

1     JUN  2014  /    --  1. YEAR

1     JUL  2014  /    --  1. YEAR

1     AUG  2014  /    --  1. YEAR

1     SEP  2014  /    --  1. YEAR

1     OCT  2014  /    --  1. YEAR

1     NOV  2014  /    --  1. YEAR

1     DEC  2014  /    --  1. YEAR

1     JAN  2015  /    --  2. YEAR

1     FEB  2015  /    --  2. YEAR

1     MAR  2015  /    --  2. YEAR

1     APR  2015  /    --  2. YEAR

1     MAY  2015  /    --  2. YEAR

1     JUN  2015  /    --  2. YEAR

1     JUL  2015  /    --  2. YEAR

1     AUG  2015  /    --  2. YEAR

1     SEP  2015  /    --  2. YEAR

1     OCT  2015  /    --  2. YEAR

1     NOV  2015  /    --  2. YEAR

1     DEC  2015  /    --  2. YEAR

1     JAN  2016  /    --  3. YEAR

1     FEB  2016  /    --  3. YEAR

1     MAR  2016  /    --  3. YEAR

1     APR  2016  /    --  3. YEAR

1     MAY  2016  /    --  3. YEAR

1     JUN  2016  /    --  3. YEAR

1     JUL  2016  /    --  3. YEAR

1     AUG  2016  /    --  3. YEAR

1     SEP  2016  /    --  3. YEAR

1     OCT  2016  /    --  3. YEAR
```

```
1 NOV 2016 / -- 3. YEAR
1 DEC 2016 / -- 3. YEAR
1 JAN 2017 / -- 4. YEAR
1 FEB 2017 / -- 4. YEAR
1 MAR 2017 / -- 4. YEAR
1 APR 2017 / -- 4. YEAR
1 MAY 2017 / -- 4. YEAR
1 JUN 2017 / -- 4. YEAR
1 JUL 2017 / -- 4. YEAR
1 AUG 2017 / -- 4. YEAR
1 SEP 2017 / -- 4. YEAR
1 OCT 2017 / -- 4. YEAR
1 NOV 2017 / -- 4. YEAR
1 DEC 2017 / -- 4. YEAR
1 JAN 2018 / -- 5. YEAR
1 FEB 2018 / -- 5. YEAR
1 MAR 2018 / -- 5. YEAR
1 APR 2018 / -- 5. YEAR
1 MAY 2018 / -- 5. YEAR
1 JUN 2018 / -- 5. YEAR
1 JUL 2018 / -- 5. YEAR
1 AUG 2018 / -- 5. YEAR
1 SEP 2018 / -- 5. YEAR
1 OCT 2018 / -- 5. YEAR
1 NOV 2018 / -- 5. YEAR
1 DEC 2018 / -- 5. YEAR
1 JAN 2019 / -- 6. YEAR
1 FEB 2019 / -- 6. YEAR
1 MAR 2019 / -- 6. YEAR
1 APR 2019 / -- 6. YEAR
1 MAY 2019 / -- 6. YEAR
1 JUN 2019 / -- 6. YEAR
1 JUL 2019 / -- 6. YEAR
1 AUG 2019 / -- 6. YEAR
1 SEP 2019 / -- 6. YEAR
1 OCT 2019 / -- 6. YEAR
1 NOV 2019 / -- 6. YEAR
1 DEC 2019 / -- 6. YEAR
```

```
1	JAN	2020	/	--	7. YEAR
1	FEB	2020	/	--	7. YEAR
1	MAR	2020	/	--	7. YEAR
1	APR	2020	/	--	7. YEAR
1	MAY	2020	/	--	7. YEAR
1	JUN	2020	/	--	7. YEAR
1	JUL	2020	/	--	7. YEAR
1	AUG	2020	/	--	7. YEAR
1	SEP	2020	/	--	7. YEAR
1	OCT	2020	/	--	7. YEAR
1	NOV	2020	/	--	7. YEAR
1	DEC	2020	/	--	7. YEAR
1	JAN	2021	/	--	8. YEAR
1	FEB	2021	/	--	8. YEAR
1	MAR	2021	/	--	8. YEAR
1	APR	2021	/	--	8. YEAR
1	MAY	2021	/	--	8. YEAR
1	JUN	2021	/	--	8. YEAR
1	JUL	2021	/	--	8. YEAR
1	AUG	2021	/	--	8. YEAR
1	SEP	2021	/	--	8. YEAR
1	OCT	2021	/	--	8. YEAR
1	NOV	2021	/	--	8. YEAR
1	DEC	2021	/	--	8. YEAR
1	JAN	2022	/	--	9. YEAR
1	FEB	2022	/	--	9. YEAR
1	MAR	2022	/	--	9. YEAR
1	APR	2022	/	--	9. YEAR
1	MAY	2022	/	--	9. YEAR
1	JUN	2022	/	--	9. YEAR
1	JUL	2022	/	--	9. YEAR
1	AUG	2022	/	--	9. YEAR
1	SEP	2022	/	--	9. YEAR
1	OCT	2022	/	--	9. YEAR
1	NOV	2022	/	--	9. YEAR
1	DEC	2022	/	--	9. YEAR
1	JAN	2023	/	--	10. YEAR
1	FEB	2023	/	--	10. YEAR
```

```
1	MAR	2023	/	--	10. YEAR
1	APR	2023	/	--	10. YEAR
1	MAY	2023	/	--	10. YEAR
1	JUN	2023	/	--	10. YEAR
1	JUL	2023	/	--	10. YEAR
1	AUG	2023	/	--	10. YEAR
1	SEP	2023	/	--	10. YEAR
1	OCT	2023	/	--	10. YEAR
1	NOV	2023	/	--	10. YEAR
1	DEC	2023	/	--	10. YEAR
1	JAN	2024	/	--	11. YEAR
1	FEB	2024	/	--	11. YEAR
1	MAR	2024	/	--	11. YEAR
1	APR	2024	/	--	11. YEAR
1	MAY	2024	/	--	11. YEAR
1	JUN	2024	/	--	11. YEAR
1	JUL	2024	/	--	11. YEAR
1	AUG	2024	/	--	11. YEAR
1	SEP	2024	/	--	11. YEAR
1	OCT	2024	/	--	11. YEAR
1	NOV	2024	/	--	11. YEAR
1	DEC	2024	/	--	11. YEAR
1	JAN	2025	/	--	12. YEAR
1	FEB	2025	/	--	12. YEAR
1	MAR	2025	/	--	12. YEAR
1	APR	2025	/	--	12. YEAR
1	MAY	2025	/	--	12. YEAR
1	JUN	2025	/	--	12. YEAR
1	JUL	2025	/	--	12. YEAR
1	AUG	2025	/	--	12. YEAR
1	SEP	2025	/	--	12. YEAR
1	OCT	2025	/	--	12. YEAR
1	NOV	2025	/	--	12. YEAR
1	DEC	2025	/	--	12. YEAR
1	JAN	2026	/	--	13. YEAR
1	FEB	2026	/	--	13. YEAR
1	MAR	2026	/	--	13. YEAR
1	APR	2026	/	--	13. YEAR
```

```
1	MAY	2026	/	--	13. YEAR
1	JUN	2026	/	--	13. YEAR
1	JUL	2026	/	--	13. YEAR
1	AUG	2026	/	--	13. YEAR
1	SEP	2026	/	--	13. YEAR
1	OCT	2026	/	--	13. YEAR
1	NOV	2026	/	--	13. YEAR
1	DEC	2026	/	--	13. YEAR
1	JAN	2027	/	--	14. YEAR
1	FEB	2027	/	--	14. YEAR
1	MAR	2027	/	--	14. YEAR
1	APR	2027	/	--	14. YEAR
1	MAY	2027	/	--	14. YEAR
1	JUN	2027	/	--	14. YEAR
1	JUL	2027	/	--	14. YEAR
1	AUG	2027	/	--	14. YEAR
1	SEP	2027	/	--	14. YEAR
1	OCT	2027	/	--	14. YEAR
1	NOV	2027	/	--	14. YEAR
1	DEC	2027	/	--	14. YEAR
1	JAN	2028	/	--	15. YEAR
1	FEB	2028	/	--	15. YEAR
1	MAR	2028	/	--	15. YEAR
1	APR	2028	/	--	15. YEAR
1	MAY	2028	/	--	15. YEAR
1	JUN	2028	/	--	15. YEAR
1	JUL	2028	/	--	15. YEAR
1	AUG	2028	/	--	15. YEAR
1	SEP	2028	/	--	15. YEAR
1	OCT	2028	/	--	15. YEAR
1	NOV	2028	/	--	15. YEAR
1	DEC	2028	/	--	15. YEAR
1	JAN	2029	/	--	END
/
END
```

# CD contains:

*PDF version of the Master Thesis*

*RMS model*

*One Eclipse simulation model (Lowcase_cave_rc10)*